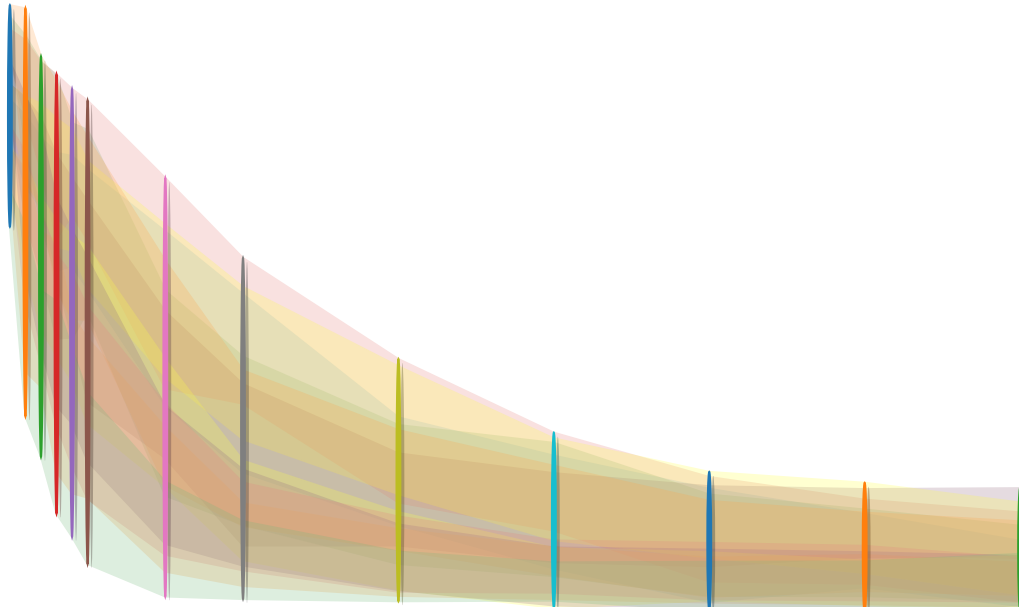




Eidgenössische Technische Hochschule Zürich
Swiss Federal Institute of Technology Zurich



Characterization of Multi-Qubit Algorithms with Randomized Benchmarking

STEFANIA BALASIU

Master's Thesis

Supervisor:

Dr. Christian Kraglund Andersen

Principal Investigator:

Prof. Dr. Andreas Wallraff

Quantum Device Lab
ETH Zürich
31st May 2018

Abstract

Superconducting quantum processors are used extensively for state-of-the-art research in quantum computing due to their good coherence properties, the high-fidelity readout schemes, and the flexibility in scaling up to larger architectures. However, in order to implement quantum error correction algorithms, the multi-qubit crosstalk and correlated errors must be understood and reduced. In this thesis I present and implement a novel extension of a previously-introduced characterization technique for multi-qubit algorithms called simultaneous randomized benchmarking (SRB). We apply random elements from the single qubit Clifford group simultaneously on up to $n = 4$ qubits, and we use single-shot, multiplexed readout to measure all the n single qubit observables $\hat{\sigma}_z$, and the $\hat{\sigma}_z^{\otimes s}$ correlators between all subsets of $s \leq n$ qubits. From the measurements of single qubit observables from each SRB experiment, we quantify the crosstalk as a 2.5-fold increase in the average single qubit infidelity per applied Clifford gate when we operate all four qubits compared to when we only operate one qubit at a time. From the correlator measurements, we calculate the total infidelity of the multi-qubit error channel associated with each n -qubit SRB experiment, which I refer to as the multi-qubit error. By comparing this quantity to the completely uncorrelated multi-qubit error, we estimate the amount of correlated errors in our algorithm. For the 4-qubit experiment, we find a total multi-qubit error of approximately $9.3 \pm 0.5\%$, with around $2.5 \pm 0.7\%$ correlated errors. We also calculate lower bounds on the multi-qubit error with only up to 2-qubit correlations, and then up to 3-qubit correlations, and we find that we may have both 2- and 3-qubit correlated errors, but we likely do not have 4-qubit correlated errors in our algorithm. From independent measurements of the AC-Stark shift between pairs of qubits we find that the crosstalk obtained from SRB might consist mostly of coherent errors such as over- or under-rotations of the qubits. On the other hand, we find large always-on $\sigma_z\sigma_z$ interactions between pairs of qubits, which are not captured by the SRB measurements.

Contents

Abstract	i
1 Introduction and motivation	1
2 Theoretical Description	3
2.1 Superconducting circuit QED	3
2.1.1 Single-qubit circuit QED	3
2.1.2 Multi-qubit circuit QED	6
2.2 Crosstalk in multi-qubit algorithms	7
2.2.1 Sources of uncorrelated errors	7
2.2.2 Sources of correlated errors	8
2.3 Randomized benchmarking	10
2.3.1 The quantum depolarizing channel	10
2.3.2 Single qubit RB	11
2.3.2.1 Interleaved single qubit RB	14
2.3.3 Multi-qubit simultaneous RB	16
2.3.4 Investigating the amount of crosstalk with multi-qubit SRB	20
2.3.5 Investigating the degree of correlated errors with multi-qubit SRB	20
2.3.5.1 Completely correlated errors	21
2.3.5.2 Completely uncorrelated errors	21
2.3.5.3 Subspace specific correlated errors	22
3 Experimental Implementation	27
3.1 Description of the multi-qubit setup	27
3.2 Single qubit virtual Z (VZ) gates	33
3.2.1 Dynamic phase correction with VZ gates	36
3.2.2 Single qubit RB with VZ gates	39
3.2.3 Single qubit IRB with VZ gates	43
4 Characterizing the amount of cross-talk and correlated errors in multi-qubit algorithms with SRB	46
4.1 Crosstalk in multi-qubit algorithms	46
4.2 Correlated errors in multi-qubit algorithms	50
4.3 Readout crosstalk in SRB experiments	57
5 Conclusions and outlook	59
Acknowledgements	61
Appendices	62
Appendix A Driving a two-level system	62
Appendix B Derivation of the inequality between correlated and uncorrelated depolarizing parameters	64
References	66

1 Introduction and motivation

Recent work on superconducting multi-qubit quantum processors has shown that superconducting qubits can reach good coherence times higher than $100\ \mu s$ [1], single- and two-qubit average gate errors as low as 0.1% [2, 3] and 1% [3, 4], respectively, and fast, high-fidelity multiplexed readout of up to five qubits with errors below 2% [5]. Due to these good properties, quantum processors based on superconducting qubits are prime candidates for implementing the next steps in multi-qubit quantum computing research. Some examples include applications of the near future with noisy intermediate-scale quantum (NISQ) computers of up to 100 qubits [6], and more long term goals of achieving fully fault-tolerant quantum error correction (QEC) schemes, which can require thousands of physical qubits and gate errors smaller than 0.1% [7].

In order to implement fault-tolerant codes, the typical gate errors must remain below a certain error-threshold in order for the logical error rates between successive cycles of the QEC code to decrease with increasing code size [7, 8]. This property of QEC codes is usually derived under the assumption that the multi-qubit errors in the algorithm are completely uncorrelated, and that they remain independent of the number of qubits in the code [7]. Hence, the type of errors that occur in multi-qubit algorithms must be identified, and their scaling with the number of qubits operated simultaneously must be investigated before implementing codes based on the fault-tolerant threshold criterion mentioned above. In this thesis we characterize these metrics using a technique based on simultaneous randomized benchmarking introduced by Gambetta et al. [9].

Several schemes have been implemented and used extensively to characterize the performance of multi-qubit algorithms. For example, quantum state tomography has been used to reconstruct multi-qubit density matrices [8, 10, 11, 12], and process and gate set tomographies [13, 14, 15] have been used to obtain process matrices that characterize gate performance in multi-qubit algorithms. However, these schemes fail to isolate the quantities of interest, the multi-qubit gate errors, from errors due to state preparation and measurement (SPAM), or they scale unfavorably with the number of qubits (for instance in gate set tomography). The randomized benchmarking technique is advantageous as it has better scaling with the number of qubits, and it captures the exponential decay of the multi-qubit state due to gate errors, which is characterized by a decay strength that is independent of SPAM.

Standard randomized benchmarking (RB) and interleaved RB have been used extensively to quantify the performance of single- and two-qubit gates [2, 16, 17, 18, 19, 20]. More recently [3], standard RB on three qubits has been used for the first time to measure average 3-qubit gate errors of around 10%. More interestingly, the authors have shown that they were not always able to calculate this error from 1- and 2-qubit gate errors obtained from single and two-qubit RB measurements performed simultaneously. In particular, the calculation could reproduce the 3-qubit result only when the $\sigma_z\sigma_z$ interactions between the qubits (an important source of correlated errors) were calibrated out before the RB measurements. Thus, the authors show that multi-qubit characterization algorithms capture effects from multi-qubit errors that are not necessarily reproduced in measurements on subsets of qubits.

Performing single qubit RB on multiple qubits at the same time implements a technique called simultaneous randomized benchmarking (SRB) [9]. This measurement allows to quantify both the scaling of the total multi-qubit error with the number of qubits in the algorithm (crosstalk), and what amount of this total error is correlated between mul-

tiple qubits (the amount of correlated errors). The authors in Ref [9] have measured both these metrics in a two-qubit SRB experiment, while the authors in Ref [21] have performed SRB on up to four qubits, but have only analyzed the scaling of crosstalk with the number of qubits.

During this project we have generalized the theory in Ref. [9] to n -qubit SRB experiments, and we have performed these measurements on all combinations of up to four qubits. The novelty of this project is that we measure all possible subsets of $\hat{\sigma}_z^{\otimes s}$ correlators on $s \leq n$ qubits in each n -qubit SRB experiment. Measuring these correlators allows us to calculate the total infidelity of the multi-qubit error channel implemented by each algorithm. By making various assumptions about the degree of the correlated errors in our data, we then calculate the amount of correlated errors present in each n -qubit algorithm, and we investigate what are the relative contributions of the s -qubit correlations for $s \leq n$ to the total amount of correlated errors we observe. Finally, we perform measurements of the AC-Stark shift and the $\sigma_z\sigma_z$ -coupling between pairs of qubits in order to investigate whether we can reproduce the multi-qubit SRB results from more basic measurements on subsets of qubits.

In the theory section of this thesis, Sec. 2, I will begin with a brief theoretical introduction to the field of superconducting circuit quantum electrodynamics, where I will also describe the 8-qubit processor on which we performed all the experiments presented in this work. In Sec. 2.2 I will then briefly discuss the main sources of correlated and uncorrelated errors in multi-qubit algorithms that will be relevant in understanding the results from SRB. The main part of the theory section will describe the formalism behind the standard RB (Sec. 2.3.2), interleaved RB (Sec. 2.3.2), and multi-qubit SRB (Sec. 2.3.3) protocols. I will discuss the quantum error channels implemented by each experiment, and how to calculate the infidelities of these channels. I will then use the latter to explain in Sec. 2.3.5 how the SRB measurement can be used to quantify the amounts of crosstalk and correlated errors in an n -qubit algorithm, and to investigate the relative contributions of various degrees of correlated errors to the total n -qubit error.

In Sec. 3, I will discuss how the (S)RB experiments were implemented in the lab. In Sec. 3.1, I will present our experimental setup, and in particular the thresholding and correlator features of our detection instrument, the Zurich Instruments Ultra High Frequency Lock-In Quantum Controller (UHFLI-QC), that were used for the (S)RB experiments discussed in this work. Then, in Sec. 3.2 I will describe the HVZ decomposition based on so-called virtual Z gates introduced by McKay et al. [2], which was used to generate the gates applied to the qubits in the (S)RB experiments.

Lastly, in Sec. 4 I show and discuss in detail the results from (S)RB measurements on all combinations of 1, 2, 3, and 4 qubits using qubits 3, 4, 5, and 7. The effect of simultaneous control on the single qubit errors is discussed in Sec. 4.1, and the amount and degree of correlated errors is discussed in Sec. 4.2.

2 Theoretical Description

In this section I will describe the theoretical background to the multi-qubit characterization measurements performed in this work. I will start with a short description of the basic superconducting circuit quantum electrodynamics (QED) architecture and its generalization to multi-qubit processors. Then I will discuss several different types of crosstalk that can occur between different qubits on the same processor, and the kinds of errors that these crosstalk mechanisms produce. Finally, I will conclude this section with a discussion about the theoretical framework of a new protocol developed during this thesis, that allows to characterize the amount of crosstalk and correlated errors in a multi-qubit processor. This protocol is based on simultaneous randomized benchmarking introduced by Gambetta et al. in Ref. [9].

2.1 Superconducting circuit QED

The theory of circuit QED based on superconducting qubits has been described in detail in many previous works [22, 23, 24]. In this thesis I will focus on the parts of this theory that are relevant to understanding single- and multi-qubit algorithms with a particular type of superconducting qubits called *transmons*.

2.1.1 Single-qubit circuit QED

In superconducting circuit QED, qubits and resonators are constructed from an electronic circuit with capacitive elements (C) and inductive components (L). A typical linear LC circuit creates a harmonic oscillator, whose quantized energy levels are equally spaced. On the other hand, a non-linear inductor such as the Josephson junction [24] placed in parallel with a capacitor creates an anharmonic oscillator. This system has unequal separation between the energy levels, which allows us to selectively excite only the desired energy transitions. We define the qubit as the first two energy levels of this non-linear system.

Based on Ref. [22], we can describe the transmon qubit as a Cooper pair box (or charge qubit) with improved coherence due to the insensitivity of the transmon's energy levels to charge noise. The Hamiltonian for the transmon qubit can be derived from an analysis of the electric circuit diagram of the transmon [22]. Here I will only reproduce the final result:

$$\hat{H}_{\text{transmon}} = 4E_C(\hat{n} - n_g)^2 - 2E_J \left| \cos\left(\frac{\pi\Phi}{\Phi_0}\right) \right| \cos\hat{\phi}. \quad (2.1)$$

This Hamiltonian has a capacitive part given by the first term, where E_C is the charging energy created by the capacitances in the transmon circuit, \hat{n} is the number operator corresponding to the number of Cooper pairs in the circuit, and n_g is the gate charge accumulated in the circuit from an external bias voltage. The second term is the inductive contribution from a magnetic-flux-tunable non-linear inductor called a SQUID loop, which consists of two Josephson junctions in parallel. Thus $E_J = \hbar I_c/2e$ is the energy of one Josephson junction, with I_c the critical current of the junction, Φ is the externally applied magnetic flux, $\Phi_0 = h/2e$ is the superconducting magnetic flux quantum, and $\hat{\phi}$ is the canonical phase operator of the electrons in the circuit. Insensitivity to electronic charge fluctuations is achieved by designing systems for which $E_J \gg E_C$ [22]. In practice,

this regime is reached by placing a capacitive element with large capacitance in parallel with the SQUID loop, thus lowering E_C with respect to E_J [23].

The experiments presented in this thesis were performed on a chip with eight Xmon qubits designed as shown in Fig. 2.1 (a). The Xmon qubit is a transmon whose capacitor in parallel with the SQUID loop has an X shape, as seen in Fig. 2.1 (b). This shape allows to create the fork-shaped capacitive couplings with larger areas, and thus stronger couplings to the readout (light blue) and qubit-qubit coupling (brown) resonators. The processor was microfabricated by depositing a 150 nm niobium (Nb) film on a sapphire substrate. All components on the chip, except for the SQUID loop, are fabricated using photolithography and dry etching techniques. The Josephson junctions in the SQUID loop were fabricated using the electron beam deposition technique, and consist of two layers of aluminum (Al) with a layer of aluminum oxide in between. For more details about the processor and the fabrication process see Ref. [5].

Since aluminum becomes superconducting at temperatures below 1.2 K, the whole processor must be cooled down to at least below this temperature in order to exploit the non-linearity of the Josephson junctions, and hence the useful features of the transmon. However, typical working temperatures in circuit QED setups are below 100 mK in order to place the qubit in the ground state by protecting it from thermal excitations.

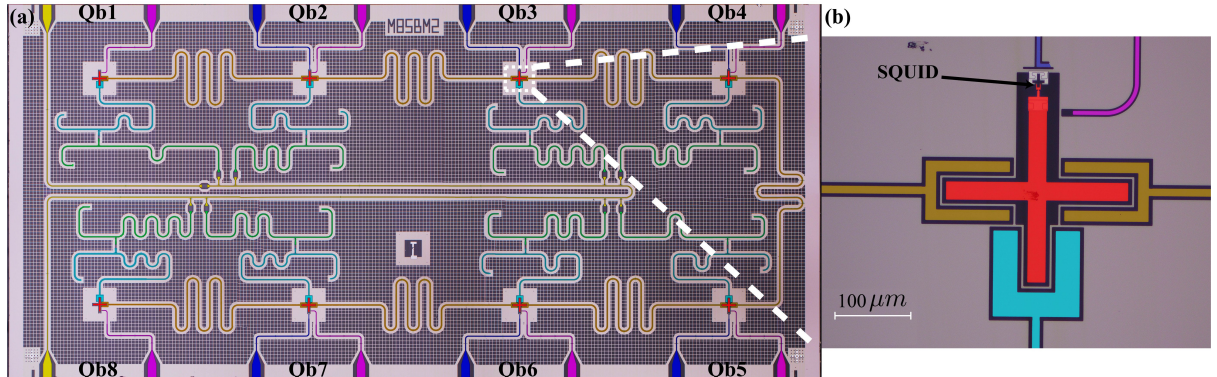


Figure 2.1: (a) False-colored microscope image of the processor design with eight Xmon qubits that was used for the experiments presented in this thesis. Each qubit has its own drive line shown in magenta, and all but Qb1 and Qb8 are tunable via their dark blue flux lines. The 8 qubits are capacitively coupled pairwise by the brown $\lambda/2$ coplanar waveguide (cpw) coupling resonators. Each Xmon is also capacitively coupled to its $\lambda/4$ readout cpw resonator in light blue, which in turn couples to a Purcell filter shown in green. The yellow directional feedline couples to all Purcell filters via interdigitated finger capacitors, and thus allows multiplexed readout of all qubits simultaneously. (b) Zoom-in of one Xmon. The SQUID loop (top) is connected in parallel with the X-shaped capacitor shown in red. The remaining arms of the capacitor couple to the readout resonator at the bottom, and to the left and right coupling resonators. The dark blue flux line allows to apply an external magnetic flux through the SQUID loop, while the magenta drive line is used to drive the qubit with a coherent microwave tone.

The coherent exchange of interactions between one Xmon and its readout resonator is described by the Jaynes-Cummings Hamiltonian [22]:

$$\hat{H}_{JC} = \sum_i \hbar\omega_i |i\rangle\langle i| + \hbar\omega_r \hat{a}^\dagger \hat{a} + \left[\sum_i \hbar g_{i,i+1} |i\rangle\langle i+1| \hat{a}^\dagger + \text{h.c.} \right]. \quad (2.2)$$

The first term in this Hamiltonian describes the energy levels of the transmon given by $\hbar\omega_i$, the second term is the energy of the readout resonator, with \hat{a}^\dagger and \hat{a} the creation and annihilation operators, respectively, and the terms in the square brackets represent the exchange interaction between the transmon and the resonator. This interaction occurs at the rate $g_{i,i+1}/2\pi$ between the resonator and the $|i+1\rangle \leftrightarrow |i\rangle$ transmon transition.

In all the experimental work presented in this thesis, we have only used the first transmon transition, from the ground state $|0\rangle = |g\rangle$ to the excited state $|1\rangle = |e\rangle$. In terms of the transmon parameters defined in Eq. (2.1), the energy of this first transition is approximately given by [22]

$$E_{01} = \sqrt{16E_C E_J \left| \cos\left(\pi \frac{\Phi}{\Phi_0}\right) \right|} - E_C. \quad (2.3)$$

$E_{01,\max} = 4\sqrt{E_C E_J} - E_C$ is the frequency of the transmon at the parking position referred to as the *sweet spot*, where the transmon is least sensitive to flux noise. From here on, I will ignore any explicit description of the higher energy levels of the transmon, but I will include the effects from the interaction of the qubit computational basis states $\{|0\rangle, |1\rangle\}$ with the next highest energy state, $|2\rangle = |f\rangle$.

In order to use this two-level system for quantum computation, it must be designed such that $g_{01} \gg \kappa_{\text{int}}, \Gamma$; i.e. the strength of the exchange interaction should dominate over internal losses from the resonator at the rate κ_{int} , and over the qubit decoherence rate Γ [25]. If this condition is met, the system is in the *strong coupling regime*. In addition, the system must also be placed in the *dispersive regime* in order to perform quantum non-demolition (QND) measurements of the qubit state, where the measurement operator is diagonal in the qubit basis $\{|g\rangle, |e\rangle\}$ at all times. This regime is achieved by detuning the qubit from the readout resonator such that $\Delta\omega_{q,r} = |\omega_q - \omega_r| \gg g_{01}/2\pi$, where $\omega_q = \omega_1$ is the frequency of the first energy transition of the transmon. If this condition is true, then the dispersive Hamiltonian is obtained from the Jaynes-Cummings Hamiltonian by treating the interaction term as a perturbation to the first two terms [23]. Here I only give the final result:

$$\hat{H}_{\text{dispersive}} = \frac{\hbar\omega'_q}{2} \hat{\sigma}_z + (\hbar\omega'_r + \chi\hat{\sigma}_z)\hat{a}^\dagger\hat{a}, \quad (2.4)$$

where $\hat{\sigma}_z$ is the Pauli Z operator. The first term describes the qubit with the frequency $\omega'_q = \omega_q + \chi_{01}$ renormalized by the Lamb shift $\chi_{01} = g_{01}^2/\Delta\omega_{q,r}$, and the second term is the resonator with renormalized frequency $\omega'_r = \omega_r - \chi_{12}$, where the shift $\chi_{12} = g_{12}^2/\Delta\omega_{2,r}$, with $\Delta\omega_{2,r} = |\omega_2 - \omega_r|$, is caused by the resonator interacting with the qubit $|f\rangle$ level. Additionally, the resonator frequency is shifted by the qubit-state-dependent *dispersive shift* $\chi\hat{\sigma}_z$, with [22]

$$\chi = \chi_{01} - \chi_{12}/2 = -g_{01}^2 \frac{E_C}{\Delta\omega_{q,r}(\Delta\omega_{q,r} - E_C)}. \quad (2.5)$$

The dispersive shift is the underlying mechanism behind the non-demolition measurement of the qubit. Since the qubit energy term commutes with the interaction term, $[\hbar\omega'_q\hat{\sigma}_z/2, \chi\hat{\sigma}_z\hat{a}^\dagger\hat{a}] = 0$, $\hat{\sigma}_z$ is a constant of motion in the system dynamics. Hence, in the dispersive regime, repeatedly probing the qubit state with a weak microwave tone for a time $\tau_m \ll T_1$, where T_1 is the qubit lifetime, will always give the same information about the qubit state that was collapsed by the first measurement. This information is contained in the dispersive shift of the transmission spectrum of the readout tone [26].

The implementation of this detection scheme using modulated microwave signals and digital signal processing will be discussed in Sec. 3.1.

Finally, the state of the Xmon is manipulated by applying microwave pulses to its drive line (magenta structures in Fig. 2.1). We can write the Hamiltonian of the qubit in a frame rotating at the drive frequency ω_d as [27]

$$\hat{H}_{drive} = \hbar \frac{\omega_q - \omega_d}{2} \hat{\sigma}_z + \frac{\hbar \Omega_R(t)}{2} (\cos(\phi) \hat{\sigma}_x + \sin(\phi) \hat{\sigma}_y), \quad (2.6)$$

where $\Omega_R(t)$ is the Rabi frequency proportional to the pulse amplitude, ϕ is the phase of the pulse, and $\hat{\sigma}_x$, $\hat{\sigma}_y$ are the Pauli X and Y operators. See Appendix A for an explicit formula for $\Omega_R(t)$ and a derivation of this Hamiltonian. From Eq. (2.6) we see that we have full control over the state of the qubit: adjusting the phase of the driving field rotates the qubit state round the \hat{x} - and \hat{y} -axes of the Bloch sphere, and driving at a frequency that is detuned from the qubit frequency leads to a rotation about the \hat{z} -axis. Driving the qubit off-resonance will also induce an AC-Stark shift of its energy levels [26, 28]. This shift will be derived in Appendix A, and its role in characterizing charge line crosstalk will be discussed in Sec. 2.2.1.

Driving on resonance with the qubit transition frequency will induce so-called *Rabi oscillations* of the qubit population between the ground and the excited state at a rate given by $\Omega_R(t)$. Throughout this thesis, I will refer to the resonant drive pulses that take the qubit from $|g\rangle$ to $|e\rangle$ and from $|g\rangle$ to $(|g\rangle + |e\rangle)/\sqrt{2}$ as a π -pulse and a $\pi/2$ -pulse, respectively.

2.1.2 Multi-qubit circuit QED

In this section I will again assume we are explicitly only concerned with the first transmon transition. See Ref. [23] for a more general version of the multi-qubit Hamiltonian that includes higher transmon levels, and in particular the $|f\rangle$ level, which becomes important in implementing two-qubit controlled-phase gates.

We can write the dispersive Hamiltonian for our system of 8 qubits and their readout resonators as [23]

$$\hat{H}_{\text{multi-qubit}} = \sum_{i=1}^8 \left[\frac{\hbar \omega'_{q,i}}{2} \hat{\sigma}_{z,i} + \hbar (\omega'_{r,i} + \chi_i \hat{\sigma}_{z,i}) \hat{a}_i^\dagger \hat{a}_i \right] + \sum_{i=1}^7 \hbar J_{i,i+1} (\hat{\sigma}_i^- \hat{\sigma}_{i+1}^+ + \hat{\sigma}_i^+ \hat{\sigma}_{i+1}^-). \quad (2.7)$$

The first term is just a sum of the single qubit dispersive Hamiltonian in Eq. (2.4) over the 8 qubits; thus I assumed that each readout resonator i couples most strongly to qubit i , such that cross-couplings to neighboring qubits $i-1$ and $i+1$ are negligible. We will see in the next section why this assumption is warranted. The second term describes the exchange interaction, or J-coupling, between neighboring qubits on the chip. The operators $\hat{\sigma}_i^+ = |1\rangle\langle 0|_i$ and $\hat{\sigma}_i^- = |0\rangle\langle 1|_i$ respectively create and annihilate an excitation in qubit i , and $J_{i,i+1}$ is given by [23]

$$J_{i,i+1} = \frac{g_{c,i} g_{c,i+1}}{2} \left(\frac{1}{\Delta\omega_{q,cr}^i} + \frac{1}{\Delta\omega_{q,cr}^{i+1}} \right). \quad (2.8)$$

Here $g_{c,i}$ and $g_{c,i+1}$ are the coupling strengths of qubits i and $i+1$ to their shared coupling resonator, and $\Delta\omega_{q,cr}^i = |\omega_{q,i} - \omega_{cr}^{(i,i+1)}|$ is the detuning of the frequency of qubit i , $\omega_{q,i}$, from that of the coupling resonator between qubits i and $i+1$, $\omega_{cr}^{(i,i+1)}$. This qubit-qubit coupling

creates a non-local swap interaction between $|01\rangle \leftrightarrow |10\rangle$ mediated by a virtual photon in the coupling resonator. The coupling is effectively turned off when $J_{i,i+1} \ll |\omega_{q,i} - \omega_{q,i+1}|$, i.e. when the two coupled qubits are detuned far away from one another. However, as we will see in the next section, in practice there is always some residual nearest-neighbor $\sigma_z\sigma_z$ -coupling that may constitute an important source of correlated errors. Qubits that are not nearest neighbors can also couple to each other (these coupling terms are ignored in the Hamiltonian in Eq. (2.7)), yet the $\sigma_z\sigma_z$ -interaction between neighbors usually dominates over these second order effects.

The QND detection mechanism is the same in the multi-qubit case as explained in the previous section for a single transmon coupled to its readout resonator. The main additional feature that can be achieved with the design in Fig. 2.1 is *multiplexed readout*. Instead of probing only one readout resonator by sending a microwave tone resonant with the frequency of that resonator, we can send a composite pulse through the yellow feedline in Fig. 2.1 that has frequency components at all or any subset of the frequencies $\omega_{r,i}$ corresponding to the 8 readout resonators on the processor. This technique allows us to measure multiple qubits at the same time. Using this feature to obtain information about qubit state correlations was indispensable to measuring the results presented in this work (see Sec. 2.3.3 and Sec. 4). For a detailed theoretical description of multiplexed readout in our group, see Ref. [29].

2.2 Crosstalk in multi-qubit algorithms

In the context of quantum information processing, the term "crosstalk" is generally used to refer to any multi-qubit error-inducing mechanism. We can make an important distinction between *uncorrelated* multi-qubit errors, which act independently in each of the single qubit subspaces, and *correlated* errors, which induce correlations between several or all qubit subspaces. Quantitatively, the total multi-qubit error channel [30] in an n -qubit algorithm \mathcal{E} is uncorrelated if $\mathcal{E} = \mathcal{E}_1 \circ \mathcal{E}_2 \circ \dots \circ \mathcal{E}_n$, where \mathcal{E}_i are the error channels associated with each single qubit channel.

The characterization and suppression of correlated errors in multi-qubit processors are particularly important goals that must be achieved in order to implement quantum error correction and fault-tolerant designs. In particular, the theory that establishes the threshold theorem for achieving fault-tolerant quantum computation [31] relies on the assumption that errors are uncorrelated [7]. In this section I will identify and discuss a few important types of crosstalk that lead to correlated and uncorrelated multi-qubit errors, and that will be relevant in the remainder of this thesis.

2.2.1 Sources of uncorrelated errors

Charge line crosstalk

We drive individual qubits by applying resonant microwave tones via their charge lines. However, a drive tone at $\omega_{q,i}$ could also couple to qubit j in a non-negligible way. Due to this *cross-driving*, or charge line crosstalk, there will be an off-resonant drive tone on qubit j that will thus induce an AC-Stark shift of the energy levels of qubit j (see Appendix A). The strength of this crosstalk between two qubits is given by the size of the induced AC-Stark frequency shift and can be characterized by the following two methods. One can directly measure the change in frequency of qubit j with a Ramsey measurement while simultaneously driving qubit i . However, this method will not be able to resolve

frequency shifts below $1/T_{\text{Ramsey}}$, where T_{Ramsey} is the delay between the two $\pi/2$ -pulses in the Ramsey measurement (see [32] for details about the Ramsey experiment). An alternative method is to drive resonant Rabi oscillations on qubit j through the charge line of qubit i . Then the AC-Stark shift $\delta\omega_{q,j|i}$ on qubit j due its coupling to the charge line of qubit i can be estimated from

$$\delta\omega_{q,j|i} = \frac{\Omega_R^2}{2\Delta\omega_{j,d}}, \quad (2.9)$$

where Ω_R is the Rabi frequency of the induced oscillations of the population of qubit j , and $\Delta\omega_{j,d} = \omega_{q,j} - \omega_{\text{drive}}$ is the frequency detuning between qubit j and the drive tone. Here I assumed that the qubit is an ideal two-level system (higher energy levels have been neglected), and that the detuning is large, $\Delta\omega_{j,d} \gg \Omega_R$. Note that the AC-Stark shift can be positive or negative depending on the sign of the detuning between the transmon and the drive, and that it decreases with larger frequency separation between the qubits. This result is derived in Appendix A.

Flux line crosstalk

The mechanism behind this type of crosstalk is very similar to the one that causes the charge line crosstalk, except that here there is cross coupling between the flux lines of different qubits. From Eq. (2.3) we see that applying a flux pulse through the SQUID loop of qubit i will change its transition frequency, $\omega_{q,i} = E_{01,i}/\hbar$, thus taking it outside the rotating reference frame defined by this frequency, where the qubit was calibrated to have zero phase. Therefore, during the excursion outside this reference frame, the qubit will acquire a *dynamic phase* given by the duration of the flux pulse, $\phi_{dyn,i} = \int \omega_{q,i}(t) - \omega_{q,i}^{(\text{park})} dt$, where $\omega_{q,i}^{(\text{park})}$ is the starting parking position of the qubit. However, other qubits will also be detuned during this operation due to flux line crosstalk, such that they will also acquire their own dynamic phases $\phi_{dyn,j}$. The dynamic phase induced on qubit j due to coupling to the flux line of qubit i can be measured with a cross-Ramsey phase measurement, where the flux pulse on qubit i is applied between the two $\pi/2$ -pulses of a Ramsey experiment on qubit j [33]. These dynamic phases must be corrected in the implementation of two-qubit controlled-phase gates as described in detail in Refs. [33] and [34]. As a result of this project, our group is now applying these corrections with the use of zero-duration, virtual Z (VZ) pulses introduced by McKay et al. in Ref. [2]. These VZ pulses and their use in dynamic phase compensation will be described in Sec. 3.2.

2.2.2 Sources of correlated errors

$\sigma_z\sigma_z$ -coupling

As already mentioned in Sec. 2.1.2, the J -interaction between two qubits is turned on only when the qubits are in resonance with one another, $\omega_{q,i} = \omega_{q,j}$. Yet if $J_{i,j} \simeq |\omega_{q,i} - \omega_{q,j}|$, with $J_{i,j}$ defined in Eq. (2.8), then the qubits have some residual $\sigma_z\sigma_z$ -coupling proportional to $J_{i,i+1}^2/|\omega_{q,i} - \omega_{q,i+1}|$, which is strongest for qubits sharing a coupling resonator. This residual qubit-qubit interaction is essentially always turned on, and, as we will see in Sec. 4, it can be a significant source of correlated errors in multi-qubit algorithms.

One method to estimate the error rate caused by the $\sigma_z\sigma_z$ -coupling between two qubits is to measure the frequency shift of one of the qubits caused by the interaction

with the other. In order to see how we can perform this measurement, we look at the total Hamiltonian of two qubits interacting via the $\sigma_z\sigma_z$ -coupling with strength $\xi/2\pi$ [35]:

$$\hat{H}_{2qb} = \frac{\hbar\omega_{q,i}}{2}\hat{\sigma}_{z,i} + \frac{\hbar\omega_{q,j}}{2}\hat{\sigma}_{z,j} + \hbar\xi\hat{\sigma}_{z,i}\hat{\sigma}_{z,j}, \quad (2.10)$$

where the first two terms describe the energies of the two qubits, and the last term is the qubit-qubit interaction term. If we rewrite this Hamiltonian as

$$\hat{H}_{2qb} = \frac{\hbar\omega_{q,i}}{2}\hat{\sigma}_{z,i} + \hbar\left(\frac{\omega_{q,j}}{2} + \xi\hat{\sigma}_{z,i}\right)\hat{\sigma}_{z,j}, \quad (2.11)$$

we see that the frequency of qubit j is conditioned on the state of qubit i , with the proportionality term ξ . Hence, we can use Ramsey measurements to find the frequencies of qubit j when qubit i is in the ground state and in the excited state, and then calculate the strength ξ of the $\sigma_z\sigma_z$ -coupling as the difference between these two frequency values. Comparing ξ to the gate duration will give an estimate of the error rate per single qubit gate due to the $\sigma_z\sigma_z$ -coupling.

Multiplexed readout crosstalk

As explained in Sec. 2.1.2, in order to perform multiplexed readout of multiple qubits we must generate a waveform with several frequency components corresponding to each qubit's readout frequency. The main cause of crosstalk in multiplexed readout is the potentially significant spectral overlap between neighboring readout frequency components. This crosstalk causes the resonator of qubit i to be additionally populated by spurious frequency tones originating from neighboring frequency components. Hence, the component of the composite readout pulse that was supposed to carry information about only one qubit will now contain information about other qubits as well. Thus, instead of only accessing the single-qubit subspace of each qubit, we will also obtain partial information about multi-qubit correlations. As we will see in the following section and in Sec. 4, this effect might distort the results of simultaneous randomized benchmarking and the conclusions regarding the amount of correlated errors in our algorithms.

Readout crosstalk was assumed to be negligibly small, and was thus not included in the multi-qubit Hamiltonian in Eq. (2.7). This assumption is warranted by the use of Purcell filters shown in green in Fig. 2.1. The effect of these filters is to suppress the amplitude of signals at each readout resonator by a factor proportional to $1/\Delta^2$ if these signals are far enough detuned from the readout resonator frequencies. Typically, this detuning is the difference between neighboring readout frequency components, $\Delta = |\omega_{r,i} - \omega_{r,j}|$. On the processor used in this thesis, the Purcell filters reduced the multiplexed readout crosstalk to below 2% [5]. This effect could be further reduced by using Gaussian-shaped readout pulses, which have a narrower frequency spectrum than the square-shaped readout pulses used in this work [5].

Finally, the readout crosstalk between two qubits can be characterized with a cross-Ramsey phase measurement, which allows to estimate the dephasing of qubit j induced by measuring qubit i . To this end, a readout pulse of varying amplitudes is applied on qubit i between the two $\pi/2$ -pulses of a Ramsey measurement on qubit j . For more details about this measurement, and about characterizing multiplexed readout crosstalk, see Ref. [29].

In this section I have described different crosstalk mechanisms and the measurements that can be performed to estimate the amount of crosstalk between pairs of qubits.

However, it is not completely understood how these types of errors behave in multi-qubit algorithms, and to what degree can multi-qubit errors be extrapolated from errors on smaller subsets of qubits. Finding insightful multi-qubit characterization techniques is a very important next step towards increasing the size of quantum processors and realizing robust error correction codes. In the next section I will discuss the theory behind one such multi-qubit error characterization scheme based on randomized benchmarking that was developed during this project.

2.3 Randomized benchamrking

The randomized benchmarking (RB) measurement is a very common characterization technique that has been used extensively to measure the average error per applied Clifford gates in both single- and multi-qubit algorithms [3, 19, 36, 37]. Here we focus on the simultaneous RB (SRB) technique on two qubits introduced by Gambetta et al. in Ref. [9]. In this project, we have generalized the theory of SRB to n -qubit experiments in order to quantify the amounts of crosstalk and correlated errors in algorithms on up to four qubits. In addition, we further extend the SRB formalism to characterize the degree of the correlated errors, and to potentially identify the s -qubit subspace that contains the largest amount of correlated errors. Since reaching fault-tolerant thresholds also entails that the errors do not increase indefinitely with the number of qubits in the algorithm [7], we also investigate the scaling of the single- and multi-qubit errors with the number of simultaneously operated qubits.

I will start the discussion of the theory of RB with a brief description of the quantum depolarizing channel, which will be a central concept to understanding RB. Then I will describe how the single- and multi-qubit RB measurements are implemented experimentally, and I will perform a theoretical analysis of each protocol from which we will understand what type of error channels they implement, and what are the relevant quantities that characterize these channels. I will discuss how we use the SRB formalism to quantify multi-qubit crosstalk, and finally, I will focus on the RB measurements on $n \leq 4$ qubits that have been experimentally implemented in this thesis, and I will describe how we can use these results to investigate the amount and the degree of correlated errors in each n -qubit algorithm.

2.3.1 The quantum depolarizing channel

The n -qubit depolarizing channel Λ_n describes a quantum noise process where the initial state described by the density operator $\hat{\rho}_n$ is left unperturbed with probability α_n , and is completely depolarized (fully mixed) with probability $1 - \alpha_n$:

$$\hat{\rho}_n \xrightarrow{\Lambda_n} (1 - \alpha_n) \frac{1}{d} + \alpha_n \hat{\rho}_n, \quad (2.12)$$

where $d = 2^n$ is the dimension of the n -qubit Hilbert space. The *survival probability* or the *depolarizing parameter* α_n describes the rate at which $\hat{\rho}_n$ is depolarized into a fully mixed state.

Below I will explicitly write down the effects of the single- and multi-qubit depolarizing channels on a density matrix expressed in the relevant Pauli basis.

Single qubit depolarizing channel

The identity matrix together with the three single qubit Pauli matrices $\{\mathbb{1}, \sigma_x, \sigma_y, \sigma_z\}$, with

$$\mathbb{1} = \begin{pmatrix} 1 & 0 \\ 0 & 1 \end{pmatrix}, \quad \sigma_x = \begin{pmatrix} 0 & 1 \\ 1 & 0 \end{pmatrix}, \quad \sigma_y = \begin{pmatrix} 0 & -i \\ i & 0 \end{pmatrix}, \quad \sigma_z = \begin{pmatrix} 1 & 0 \\ 0 & -1 \end{pmatrix}, \quad (2.13)$$

form a basis for the space of 2×2 Hermitian matrices, and therefore they span the space of single-qubit observables. Hence we can express any single qubit density matrix ρ_1 in terms of this Pauli basis as

$$\rho_1 = \frac{\mathbb{1}}{2} + \rho_{x,1}\sigma_x + \rho_{y,1}\sigma_y + \rho_{z,1}\sigma_z, \quad (2.14)$$

where $\rho_{\xi,1}$ is the coefficient of ρ_1 in the single qubit subspace defined by the Pauli matrix $\xi \in \{\sigma_x, \sigma_y, \sigma_z\}$. In this representation, the action of the single-qubit depolarizing channel Λ_1 on ρ_1 becomes

$$\rho_1 \xrightarrow{\Lambda_1} \frac{\mathbb{1}}{2} + \alpha_1(\rho_{x,1}\sigma_x + \rho_{y,1}\sigma_y + \rho_{z,1}\sigma_z). \quad (2.15)$$

Multi-qubit depolarizing channel

Similarly, the n -fold tensor product of the single-qubit Pauli basis $\{\mathbb{1}, \sigma_x, \sigma_y, \sigma_z\}^{\otimes n}$ spans the space of n -qubit observables, and thus we can express the n -qubit density matrix ρ_n in terms of this basis as:

$$\rho_n = \frac{\mathbb{1}}{d} + \sum_{i \leq n} \sum_{\varsigma=x,y,z} \rho_{\varsigma,i}\sigma_{\varsigma,i} + \sum_{\substack{i,j \leq n \\ i < j}} \sum_{\varsigma,\varsigma'=x,y,z} \rho_{\varsigma\varsigma',ij} \sigma_{\varsigma,i}\sigma_{\varsigma',j} + \dots, \quad (2.16)$$

where $d = 2^n$. Each $\rho_{\xi,s}$ is the coefficient of ρ_n in the subspace defined by the qubits $s \leq n$ and spanned by the corresponding Pauli operators $\xi \in \{\mathbb{1}, \sigma_x, \sigma_y, \sigma_z\}^{\otimes s}$. Here $\mathbb{1}$ is the n -dimensional identity matrix. Then the action of the n -qubit depolarizing channel Λ_n on ρ_n expressed in this basis becomes

$$\rho_n \xrightarrow{\Lambda_n} \frac{\mathbb{1}}{2^n} + \alpha_n \left(\sum_{i \leq n} \sum_{\varsigma=x,y,z} \rho_{\varsigma,i}\sigma_{\varsigma,i} + \sum_{\substack{i,j \leq n \\ i < j}} \sum_{\varsigma,\varsigma'=x,y,z} \rho_{\varsigma\varsigma',ij} \sigma_{\varsigma,i}\sigma_{\varsigma',j} + \dots \right). \quad (2.17)$$

In the next few sections I will use these definitions for the single and multi-qubit depolarizing channels to give a theoretical overview of the quantum channels described by the single- and multi-qubit randomized benchmarking protocols.

2.3.2 Single qubit RB

The single qubit RB experiment is used to characterize the average infidelity of single qubit gates over the single qubit Clifford group \mathcal{C}_1 . The latter is defined as the *normalizer* of the single qubit Pauli group $\mathcal{P} = \{\pm P, \pm iP\}_{P \in [\mathbb{1}, \sigma_x, \sigma_y, \sigma_z]}$ in the unitary group of degree 2, $U(2)$, which describes the set of all 2×2 unitary matrices. In group theory, this means that the Clifford group is defined by those elements in the $U(2)$ group whose conjugation action on the Pauli group returns elements that are still within the Pauli group [38]:

$$\mathcal{C}_1 = \{U \in U(2); P_i, P_j \in \mathcal{P}, i \neq j : UP_iU^\dagger = \pm P_j\}. \quad (2.18)$$

The RB measurement protocol relies on sampling random elements from \mathcal{C}_1 , which is expressed in a suitable decomposition in terms of single qubit gates. Details about this decomposition will be given in Sec. 3.2.2. The RB protocol is illustrated in Fig. 2.2 and contains the following steps:

1. Choose a sequence length m in the interval $[0, M]$, where M is the longest sequence used in the experiment.
2. Generate m random Clifford elements $\{G_i\}_{i \in [1, m]}$ sampled uniformly from \mathcal{C}_1 .
3. Generate the $(m + 1)^{\text{st}}$ so-called *recovery gate* to be the inverse of the previous m gates $G_{m+1} = (G_m \dots G_1)^\dagger$.
4. Prepare the qubit in some initial state, which is typically in an eigenstate of the single qubit $\hat{\sigma}_z$ operator, apply the sequence $G_{m+1}G_m \dots G_1$, and measure the qubit in the $\hat{\sigma}_z$ basis.
5. Repeat step 4 a large number of times N (typically $N > 2^{10}$) and average all the N measurement results (shots) to obtain $\langle \hat{\sigma}_z \rangle$. A larger value of N improves the statistical accuracy of the RB results; see Sec. 3.2.2.
6. Repeat steps 2-5 K times in order to sample the Clifford group K times, and average all the K measured values of $\langle \hat{\sigma}_z \rangle$. As I will explain in Sec. 3.2.2, the value for K depends on the desired accuracy of the RB results related to finite sampling of \mathcal{C}_1 .
7. Repeat steps 2-6 for all sequence lengths $m \in [0, M]$.

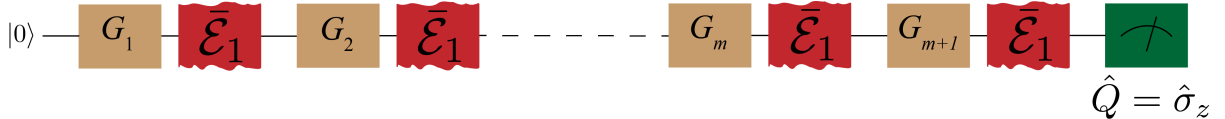


Figure 2.2: One Clifford sequence of length m in the single qubit RB protocol. This gate sequence is applied to the qubit in the ground state, and the $\hat{\sigma}_z$ operator is measured after the recovery gate, $G_{m+1} = (G_m \dots G_1)^\dagger$. Each Clifford gate G_i in the sequence depicted in light brown is the ideal, unitary implementation of the noisy Clifford gate \tilde{G}_i that has an associated average error channel $\bar{\mathcal{E}}_1$ shown in red.

In order to understand the quantum channel that is implemented by the RB protocol, we will consider the error channel \mathcal{E}_k , which in the most general form is described as a completely positive, trace-preserving (CPTP) map, associated with each applied Clifford gate in the k^{th} repetition of the sequence of length m . It has been shown [16] that for typical errors, each Clifford gate error \mathcal{E}_k is well approximated by the average error channel over the entire sequence $\bar{\mathcal{E}}_1$. Hence, our applied, imperfect Clifford gates can be expressed as $\tilde{G}_{i,k} = \bar{\mathcal{E}}_1 \circ G_{i,k}$ for $i \in [1, m + 1]$ and $k \in [1, K]$, where $G_{i,k}$ denotes the ideal, unitary implementation of the Clifford gate, and \circ denotes composition of error channels. We therefore assume that, on average, all the Clifford elements have the same error and that this error is independent of the Clifford gates. Thus, we can write the sequence of m Cliffords as

$$\mathcal{S}_{m,k} = \bar{\mathcal{E}}_1 \circ G_{m+1,k} \circ \bar{\mathcal{E}}_1 \circ G_{m,k} \circ \dots \circ \bar{\mathcal{E}}_1 \circ G_{1,k}, \quad (2.19)$$

or, using that $G_{m+1,k} = (G_{m,k} \dots G_{1,k})^\dagger$,

$$\mathcal{S}_{m,k} = \bar{\mathcal{E}}_1 \circ \left(\bigcirc_{i=1}^m G_{i,k}^\dagger \circ \bar{\mathcal{E}}_1 \circ G_{i,k} \right). \quad (2.20)$$

Then the average over the K different sequences sampled from the group becomes

$$\mathcal{S}_m = \frac{1}{K} \sum_{k=1}^K \mathcal{S}_{m,k}. \quad (2.21)$$

If we *assume* that we have fully sampled the Clifford group for each m , we can rewrite this averaging process in terms of the average, or *twirl*, over the Clifford group \mathcal{C}_1 , which I denote by $\mathcal{T}_{\mathcal{C}_1}(\bar{\mathcal{E}}_1)$:

$$\mathcal{S}_m = \bar{\mathcal{E}}_1 \circ \left(\mathcal{T}_{\mathcal{C}_1}(\bar{\mathcal{E}}_1) \right)^{\circ m}. \quad (2.22)$$

The twirl of the channel $\bar{\mathcal{E}}_1$ over a group of unitary channels, here the Clifford elements, is given by [9]

$$\mathcal{T}_{\mathcal{C}_1}(\bar{\mathcal{E}}_1) = \frac{1}{|\mathcal{C}_1|} \sum_{G \in \mathcal{C}_1} G^\dagger \circ \bar{\mathcal{E}}_1 \circ G. \quad (2.23)$$

In practice, K would become too large if we wanted to generate all the possible Clifford sequences of length m ; see Sec. 3.2.2. Therefore, the assumption above is generally not true, and we will use the theory developed by Helsen et al. in [39] to estimate confidence intervals around the quantities of interest, that capture the errors due to finite sampling of \mathcal{C}_1 .

I will now use the Liouville superoperator representation of quantum channels in the normalized Pauli basis $\mathcal{P}_1 = \frac{1}{\sqrt{2}}\{\mathbb{1}, \sigma_x, \sigma_y, \sigma_z\}$, where each element now has a trace of 1 [39]. This allows us to write the Pauli transfer matrix of any map Λ as a matrix $\Lambda_{ij} = \frac{1}{d}\text{Tr}[P_i \Lambda(P_j)]$, with $P_i, P_j \in \mathcal{P}_1$, and the dimension of the Hilbert space $d = 2$ for a single qubit. In this representation, all maps are matrices and thus channel composition simply becomes matrix-matrix multiplication. Hence, we can rewrite Eq. (2.23) as [9]

$$\mathcal{T}_{\mathcal{C}_1}(\bar{\mathcal{E}}_1) = \frac{1}{|\mathcal{C}_1|} \sum_{G \in \mathcal{C}_1} \mathbf{G}^\dagger \bar{\mathcal{E}}_1 \mathbf{G}. \quad (2.24)$$

The twirling process is the key concept in the theory of randomized benchmarking. The Clifford group is a unitary 2-design [40]. This means that the twirl of any channel Λ over the Clifford group is the same as twirling over the unitary group $U(2)$ [39], and that the Liouville (or the Pauli transfer matrix) representation of both the Clifford group and the unitary group has two independent and irreducible representations in the normalized Pauli basis. The first, trivial representation s_0 is given by the identity $\mathbb{1}/\sqrt{2}$, and the second s_1 is given by everything else in the Pauli group $\{\sigma_x, \sigma_y, \sigma_z\}/\sqrt{2}$ [9, 39]. The fact that the two representations of the Clifford group are independent means that the action of \mathcal{C}_1 in the first subspace is independent of its action in the second subspace. The fact that the two representations are irreducible further means that we cannot find any similarity transformation matrix¹ that will reduce the dimension of the subspace of that representation [41].

¹A similarity transformation is the map $A \rightarrow B^{-1}AB$, for some group element A , and the similarity transformation matrix B .

Given these properties of the Clifford group we can make use of one of the corollaries to Schur's Lemma, which says that the group average over the conjugation of a channel by the elements of the group, i.e. the twirl, is given by [9]

$$\mathcal{T}_{\mathcal{C}_1}(\bar{\mathcal{E}}_1) = \sum_{\varsigma \in \{s_0, s_1\}} \frac{\text{Tr}(\bar{\mathcal{E}}_1 \mathbb{P}_\varsigma)}{\text{Tr}(\mathbb{P}_\varsigma)} \mathbb{P}_\varsigma, \quad (2.25)$$

where \mathbb{P}_ς are the projectors into the two irreducible representations of the Clifford group. Since the subspace s_1 is irreducible, the action of \mathcal{C}_1 is the same on all the elements in this subspace, and we can rewrite the twirl as

$$\Lambda_1 = \mathcal{T}_{\mathcal{C}_1}(\bar{\mathcal{E}}_1) = (1 - \alpha_1) \frac{1}{2} + \alpha_1 \sum_{\varsigma \in s_1} \mathbb{P}_\varsigma, \quad (2.26)$$

$$\alpha_1 = \sum_{\varsigma \in s_1} \frac{\text{Tr}(\bar{\mathcal{E}}_1 \mathbb{P}_\varsigma)}{\text{Tr}(\mathbb{P}_\varsigma)}, \quad (2.27)$$

It is now apparent that the twirl describes the single qubit depolarizing channel Λ_1 with an associated depolarizing parameter α_1 . Hence, the twirl over the single qubit Clifford group with the average error $\bar{\mathcal{E}}_1$ is a depolarizing channel. In the context of single qubit RB, I will denote this depolarizing channel by $\Lambda_{\mathcal{C}_1}$.

It is then clear that the measured quantities $\langle \hat{\sigma}_z \rangle_m$ as a function of the Clifford sequence lengths m will decay exponentially towards a fully mixed state. This decay is characterized by the decay constant α_1 , which can be found experimentally from a fit of the $\langle \hat{\sigma}_z \rangle$ data to the equation

$$\langle \hat{\sigma}_z \rangle_m = A \alpha_1^m + B. \quad (2.28)$$

Here, the constants A and B quantify all the information about SPAM (state preparation and measurement) errors. The fact that the decay strength specified by α_1 is first-order independent of SPAM errors makes the RB protocol a very powerful tool for characterizing gate errors and the overall performance of the algorithm. For a theoretical discussion of second order error effects, see Ref. [16].

Knowing α_1 , the average fidelity of the channel $\Lambda_{\mathcal{C}_1}$ with respect to the identity channel $\mathbb{1}$ can be easily calculated as

$$\bar{F}(\Lambda_{\mathcal{C}_1}, \mathbb{1}) = \text{Tr}\left(\hat{M} \Lambda_{\mathcal{C}_1}(\hat{\rho}_0)\right) = 1 - \frac{1 - \alpha_1}{2}, \quad (2.29)$$

where, for single qubit RB, the initial density operator $\hat{\rho}_0 = |0\rangle\langle 0|$ represents the ground state of the qubit, and the measurement operator $\hat{M} = |0\rangle\langle 0|$ is the projector back into the ground state. The average *channel infidelity*, or average *error per Clifford*, immediately follows:

$$r_1 = r(\Lambda_1) = 1 - \bar{F}(\Lambda_{\mathcal{C}_1}, \mathbb{1}) = \frac{1 - \alpha_1}{2}. \quad (2.30)$$

2.3.2.1 Interleaved single qubit RB

A useful variation of the single qubit RB protocol is interleaved RB (IRB), which allows to find the average error of a particular gate of interest. In this thesis, I have only implemented IRB on single qubit gates, yet the theory for IRB can also be used to find n -qubit gate errors; see [37] for a measurement of the average error of a two-qubit gate with IRB.

The IRB measurement implements the same protocol as described in the previous section for single qubit RB, but with an addition which can be summarized as follows, see also Fig. 2.3:

1. Perform standard single qubit RB and find the depolarizing parameter α_1 as described in the previous section.
2. Perform standard single qubit RB with the gate of interest G interleaved between each two Clifford elements. The recovery gate $G_{m+1,k}$ now inverts the new sequence $(G_{m,k}GG_{m-1,k}\dots G_{2,k}GG_{1,k})^\dagger$ for all repetitions $k \in [1, K]$ and all lengths $m \in [0, M]$. Fit to Eq. (2.28) and extract the depolarizing parameter α'_1 , which will be explained below.
3. Calculate the average gate error of G from [17]

$$\mathbf{r}_G = \frac{d-1}{d} \left(1 - \frac{\alpha'_1}{\alpha_1} \right), \quad (2.31)$$

where $d = 2$ for a single qubit gate.



Figure 2.3: One Clifford sequence of length m in the single qubit IRB protocol. This gate sequence is applied to the qubit in the ground state, and the $\hat{\sigma}_z$ operator is measured after the recovery gate, $G_{m+1} = (G_m G \dots G G_1)^\dagger$. Each Clifford gate G_i in the sequence depicted in light brown is the ideal, unitary implementation of the noisy Clifford gate \tilde{G}_i , that has an associated average error channel $\bar{\mathcal{E}}_1$ shown in red. The noisy gate of interest \tilde{G} , whose average error we are interested in finding, is interleaved between every two noisy Clifford gates \tilde{G}_i . \tilde{G} is also decomposed into the perfectly unitary gate of interest G shown in light blue, and its associated error channel \mathcal{E} shown in purple.

In order to be able to write the twirl in Eq. (2.24), it is important that the gate of interest is part of the single qubit Clifford group \mathcal{C}_1 . We again assume that each noisy Clifford gate has an associated average error channel $\bar{\mathcal{E}}_1$ such that $\tilde{G}_{i,k} = \bar{\mathcal{E}}_1 \circ G_{i,k}$. Here we also assume that we can write the noisy gate of interest $\tilde{G} = \mathcal{E} \circ G$ in terms of its ideal, unitary description, G , and the average error channel associated with it, \mathcal{E} . Then we can write the average sequence superoperator for IRB in a similar way as we did in Eqs. (2.20) and (2.21) [17]:

$$\mathcal{S}_m = \frac{1}{K} \sum_{k=1}^K \bar{\mathcal{E}}_1 \circ \left(\bigcirc_{i=1}^m G_{i,k}^\dagger \circ G^\dagger \circ \mathcal{E} \circ \bar{\mathcal{E}}_1 \circ G \circ G_{i,k} \right). \quad (2.32)$$

One can follow the same derivation steps to obtain this equation as I did in the previous section. The twirl is now the average of the composed channel $\mathcal{E} \circ \bar{\mathcal{E}}_1$, which in Liouville representation becomes a matrix multiplication:

$$\mathcal{T}_{\mathcal{C}_1}(\mathcal{E} \bar{\mathcal{E}}_1) = \frac{1}{|\mathcal{C}_1|} \sum_{G \in \mathcal{C}_1} G^\dagger \mathcal{E} \bar{\mathcal{E}}_1 G. \quad (2.33)$$

As shown in [17], the zeroth order model of this twirl describes a depolarizing channel,

$$\Lambda_{\text{IRB}}(\rho_1) = \Lambda_I(\rho_1) \circ \Lambda_1(\rho_1) = (1 - \alpha'_1) \frac{1}{2} + \alpha'_1 \rho_1, \quad (2.34)$$

with a depolarizing parameter α'_1 . Thus, we can extract α'_1 from a fit to Eq. (2.28), and use it in Eq. (2.31) to find the average gate error associated with \tilde{G} .

2.3.3 Multi-qubit simultaneous RB

The n -qubit simultaneous RB (SRB) measurement consists of n simultaneous applications of the single qubit RB protocol on n qubits. Hence, this technique can be used to estimate the average error of the n -qubit channel per simultaneous application of n elements from the single qubit Clifford group, or equivalently per simultaneous application of one element from the n -fold tensor product of this group, $\mathcal{C}_1^{\otimes n}$. Moreover, as will be explained in this section, this technique also allows to characterize the amount of multi-qubit crosstalk in the algorithm, as well as the amount and the degree of correlated errors between the different single qubit subspaces.

The n -qubit SRB experiment as implemented in this thesis is an extension of the theory and implementation by Gambetta et al. in Ref. [9]. The experimental protocol is as follows, see also Fig. 2.4:

1. Choose a sequence length m in the interval $[0, M]$, where M is the longest sequence used in the experiment.
2. Prepare the n qubits in the $+1$ eigenspace of a chosen Pauli operator. Here we choose the $\hat{\sigma}_z^{\otimes n}$ operator and the initial state $|0\rangle^{\otimes n}$.
3. For each qubit $s \leq n$, generate m random Clifford elements $\{G_{i,s}\}_{i \in [1,m]}$ sampled uniformly from the single qubit Clifford group \mathcal{C}_1 .
4. For each qubit $s \leq n$, generate the $(m+1)^{\text{st}}$ recovery gate to be the inverse of the previous m gates on that qubit, $G_{m+1,s} = (G_{m,s} \dots G_{1,s})^\dagger$.
5. Apply the generated sequences $G_{m+1,s} G_{m,s} \dots G_{1,s}$ simultaneously to each qubit s , for all $s \leq n$. Measure all the single-qubit operators $\hat{\sigma}_{z,s}$ as well as all the possible combinations of multi-qubit operators $\hat{\sigma}_{z,i} \otimes \hat{\sigma}_{z,j} \otimes \dots \otimes \hat{\sigma}_{z,s}$, for all $s \leq n$. In order to use Ref. [39] to estimate upper bounds on the confidence intervals around the data points and the quantities of interest, it is important that all these measurement operators stabilize the initial state in the corresponding s -qubit subspace. See Ref. [31] for details about the quantum stabilizer formalism.
6. Repeat step 5 a large number of times N (typically $N > 2^{10}$) and average all the N measurement shots for each qubit to obtain $\langle \hat{\sigma}_{z,i} \otimes \dots \otimes \hat{\sigma}_{z,s} \rangle$ for all $s \in [1, n]$. A larger value of N improves the statistical accuracy of the RB results; see Sec. 3.2.2.
7. Repeat steps 2-6 K times in order to sample the n -fold tensor product of the Clifford group K times, and average all the K measured values of $\langle \hat{\sigma}_{z,i} \otimes \dots \otimes \hat{\sigma}_{z,s} \rangle$ for all $s \leq n$. As in the single qubit protocol, the value for K depends on the desired accuracy of the RB results due to finite sampling of \mathcal{C}_1 for each qubit.
8. Repeat steps 2-7 for all sequence lengths $m \in [0, M]$.

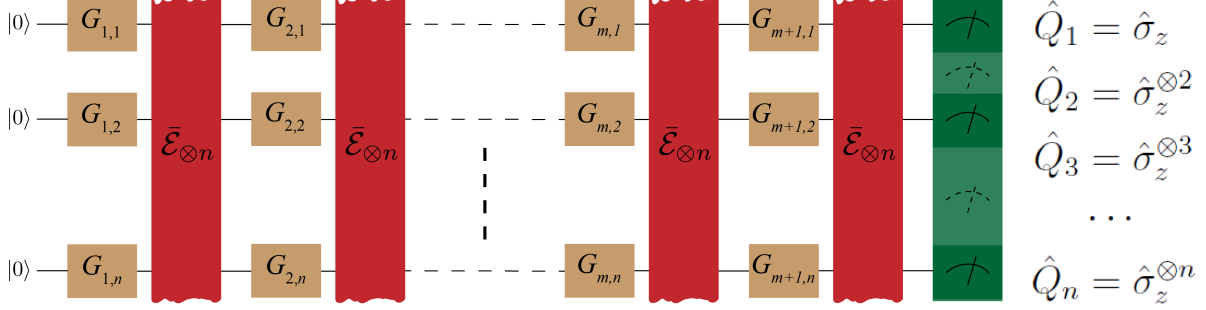


Figure 2.4: n single qubit Clifford sequences each of length m applied simultaneously to all n qubits in the multi-qubit simultaneous RB protocol. The entire $n \times (m + 1)$ multi-qubit gate sequence is applied to the collective ground state of the n -qubit system $|0\rangle^{\otimes n}$, and the operators $\hat{\sigma}_z^{\otimes s}$ for all the possible $s \leq n$ -qubit subspaces are measured after the n simultaneously applied recovery gates, $G_{m+1,s} = (G_{m,s} \dots G_{1,s})^\dagger$, $s \in [1, n]$. Each simultaneous application of n unitary single qubit Clifford gates $G_{i,s}$, $i \in [1, m + 1]$, $s \in [1, n]$, shown in light brown can be thought of as a multi-qubit gate, with its associated average multi-qubit error channel $\bar{\mathcal{E}}_{\otimes n}$ shown in red.

From here on, I will simply write $\sigma_{z,i} \dots \sigma_{z,s}$ instead of $\hat{\sigma}_{z,i} \otimes \dots \otimes \hat{\sigma}_{z,s}$.

We denote by $\bar{\mathcal{E}}_{\otimes n}$ the CPTP multi-qubit error map associated with a single simultaneous application of n noisy Clifford elements, $\tilde{G}_{i,1} \tilde{G}_{i,2} \dots \tilde{G}_{i,n}$. The protocol described above twirls the error channel $\bar{\mathcal{E}}_{\otimes n}$ with the n -fold tensor product of the single qubit Clifford group, $\mathcal{C}_1^{\otimes n}$. If we assume that each $\tilde{G}_{i,s}$, $s \leq n$, acts independently in its respective single qubit subspace, then the irreducible representations of this group are given by the n -fold product $(s_0 \otimes s_1)^n$ of the two irreducible and independent representations s_0 and s_1 of the single qubit Clifford group discussed in the previous section [9]. More explicitly, an n -qubit SRB experiment has the irreducible representations given by the action of the group $\mathcal{C}_1^{\otimes n}$ in each of the following subspaces:

$$\begin{aligned}
& \mathbb{1}\mathbb{1}\dots\mathbb{1}, \\
& \sigma\mathbb{1}\dots\mathbb{1}, \quad \sigma \in \{\sigma_x, \sigma_y, \sigma_z\} \\
& \mathbb{1}\sigma\dots\mathbb{1}, \quad \sigma \in \{\sigma_x, \sigma_y, \sigma_z\} \\
& \dots \\
& \sigma_1\sigma_2\mathbb{1}\dots\mathbb{1}, \quad \sigma_1, \sigma_2 \in \{\sigma_x, \sigma_y, \sigma_z\} \\
& \mathbb{1}\sigma_1\sigma_2\dots\mathbb{1}, \quad \sigma_1, \sigma_2 \in \{\sigma_x, \sigma_y, \sigma_z\} \\
& \dots \\
& \sigma_1\sigma_2\dots\sigma_s\mathbb{1}\dots\mathbb{1}, \quad \sigma_1, \sigma_2, \dots, \sigma_s \in \{\sigma_x, \sigma_y, \sigma_z\} \\
& \mathbb{1}\sigma_1\sigma_2\dots\sigma_s\mathbb{1}\dots\mathbb{1}, \quad \sigma_1, \sigma_2, \dots, \sigma_s \in \{\sigma_x, \sigma_y, \sigma_z\} \\
& \dots \\
& \sigma_1\sigma_2\sigma_3\dots\sigma_n, \quad \sigma_1, \sigma_2, \dots, \sigma_n \in \{\sigma_x, \sigma_y, \sigma_z\}.
\end{aligned} \tag{2.35}$$

Thus, again using Schur's lemma, we can write the twirl over the group $\mathcal{C}_1^{\otimes n}$ as

$$\mathcal{T}_{\mathcal{C}_1^{\otimes n}}(\bar{\mathcal{E}}_{\otimes n}) = \sum_{\varsigma \in \{(s_0 \otimes s_1)^n\}} \frac{\text{Tr}(\bar{\mathcal{E}}_{\otimes n} \mathbb{P}_\varsigma)}{\text{Tr}(\mathbb{P}_\varsigma)} \mathbb{P}_\varsigma, \tag{2.36}$$

where \mathbb{P}_ς are now the projectors into each of the irreducible subspaces in Eqs. (2.35). Hence, this twirl implements the depolarizing channel $\Lambda_{\mathcal{C}_1^{\otimes n}}$, which is now a composition of the depolarizing channels in each of the subspaces in Eqs. (2.35). In other words, this channel can be expressed a composition of all the depolarizing channels on $s \leq n$ qubits [9],

$$\Lambda_{\mathcal{C}_1^{\otimes n}} = \left(\bigcirc_{i \leq n} \Lambda_i^{(n)} \right) \circ \left(\bigcirc_{\substack{i,j \leq n \\ i < j}} \Lambda_{ij}^{(n)} \right) \circ \left(\bigcirc_{\substack{i,j,k \leq n \\ i < j < k}} \Lambda_{ijk}^{(n)} \right) \circ \dots \circ \Lambda_{12\dots n}^{(n)}, \quad (2.37)$$

where we *define* each $\Lambda_{ij\dots s}^{(n)}$ to be the depolarizing channel acting only in the s -qubit subspace in an n -qubit SRB experiment, while leaving the other qubit subspaces unperturbed. Therefore, $\Lambda_{ij\dots s}^{(n)}$ acts only on the coefficients of $\hat{\rho}_n$ in Eq. (2.16) that are in the s -qubit subspace according to the following maps:

$$\sum_{i \leq n} \sum_{\varsigma=x,y,z} \rho_{\varsigma,i} \sigma_{\varsigma,i} \xrightarrow{\Lambda_i^{(n)}} \sum_{i \leq n} \alpha_i^{(n)} \sum_{\varsigma=x,y,z} \rho_{\varsigma,i} \sigma_{\varsigma,i}, \quad (2.38)$$

$$\sum_{\substack{i,j \leq n \\ i < j}} \sum_{\varsigma,\varsigma'=x,y,z} \rho_{\varsigma\varsigma',ij} \sigma_{\varsigma,i} \sigma_{\varsigma',j} \xrightarrow{\Lambda_{ij}^{(n)}} \sum_{\substack{i,j \leq n \\ i < j}} \alpha_{ij}^{(n)} \sum_{\varsigma,\varsigma'=x,y,z} \rho_{\varsigma\varsigma',ij} \sigma_{\varsigma,i} \sigma_{\varsigma',j} \quad (2.39)$$

...

Here, each $\alpha_{ij\dots s}^{(n)}$ is the depolarizing parameter that describes the depolarizing strength on the s -qubit subspace while simultaneously twirling the subspace on the remaining $(n - s)$ qubits. I point out here for clarity that the number or letter in parentheses in the exponential, (n) , will always denote the number of qubits operated on simultaneously, i.e. an n -qubit SRB experiment. This notation will also indicate that the quantity is an *experimentally measured* quantity.

Before we move on, let us explicitly write Eqs. (2.37)-(2.39) for a 2-qubit SRB experiment, which has been implemented in Refs. [9] and [37]. Eq. (2.37) becomes simply

$$\Lambda_{\mathcal{C}_1^{\otimes 2}} = \Lambda_1^{(2)} \circ \Lambda_2^{(2)} \circ \Lambda_{12}^{(2)}, \quad (2.40)$$

where we have the two single qubit channels $\Lambda_1^{(2)}$, $\Lambda_2^{(2)}$, and the two-qubit channel $\Lambda_{12}^{(2)}$. By writing out the expression for ρ_2 in the 2-qubit Pauli basis using Eq. (2.16),

$$\begin{aligned} \rho_2 = \frac{1}{4} + & (\rho_{x,1} \sigma_{x,1} + \rho_{y,1} \sigma_{y,1} + \rho_{z,1} \sigma_{z,1}) + \\ & (\rho_{x,2} \sigma_{x,2} + \rho_{y,2} \sigma_{y,2} + \rho_{z,2} \sigma_{z,2}) + \\ & (\rho_{xx,12} \sigma_{x,1} \sigma_{x,2} + \rho_{xy,12} \sigma_{x,1} \sigma_{y,2} + \rho_{xz,12} \sigma_{x,1} \sigma_{z,1} + \\ & \rho_{yx,12} \sigma_{y,1} \sigma_{x,2} + \rho_{yy,12} \sigma_{y,1} \sigma_{y,2} + \rho_{yz,12} \sigma_{y,1} \sigma_{z,2} + \\ & \rho_{zx,12} \sigma_{z,1} \sigma_{x,2} + \rho_{zy,12} \sigma_{z,1} \sigma_{y,2} + \rho_{zz,12} \sigma_{z,1} \sigma_{z,2}), \end{aligned} \quad (2.41)$$

the actions of $\Lambda_1^{(2)}$, $\Lambda_2^{(2)}$, and $\Lambda_{12}^{(2)}$ on ρ_2 can be described by the following maps:

$$\rho_{x,1}, \rho_{y,1}, \rho_{z,1} \xrightarrow{\Lambda_1^{(2)}} \alpha_1^{(2)} \rho_{x,1}, \alpha_1^{(2)} \rho_{y,1}, \alpha_1^{(2)} \rho_{z,1}, \quad (2.42)$$

$$\rho_{x,2}, \rho_{y,2}, \rho_{z,2} \xrightarrow{\Lambda_2^{(2)}} \alpha_2^{(2)} \rho_{x,2}, \alpha_2^{(2)} \rho_{y,2}, \alpha_2^{(2)} \rho_{z,2}, \quad (2.43)$$

$$\rho_{xx,12}, \rho_{xy,12}, \dots, \rho_{zz,12} \xrightarrow{\Lambda_{12}^{(2)}} \alpha_{12}^{(2)} \rho_{xx,12}, \alpha_{12}^{(2)} \rho_{xy,12}, \dots, \alpha_{12}^{(2)} \rho_{zz,12}. \quad (2.44)$$

Hence, we can define the total depolarizing parameter associated with the total 2-qubit channel $\Lambda_{\mathcal{C}_1^{\otimes 2}}$ as the sum of the depolarizing parameters from each subspace, weighted by the number of terms in that subspace:

$$\bar{\alpha}_2 = \frac{1}{15} \left(3\alpha_1^{(2)} + 3\alpha_2^{(2)} + 9\alpha_{12}^{(2)} \right), \quad (2.45)$$

where we normalize by

$$\sum_{\mathbb{P} \in \{\{\sigma_x, \sigma_y, \sigma_z\}\}^2} \text{Tr}(\mathbb{P}) = 15. \quad (2.46)$$

Notice that this normalization constant is just the sum of all the terms in Eq. (2.45).

From this analysis for a 2-qubit SRB experiment, it is easy to see that the depolarizing parameter associated with the full multi-qubit $\Lambda_{\mathcal{C}_1^{\otimes n}}$ channel is given by

$$\bar{\alpha}_n = \frac{1}{A} \left(\sum_{i \leq n} 3\alpha_i^{(n)} + \sum_{\substack{i,j \leq n \\ i < j}} 9\alpha_{ij}^{(n)} + \sum_{\substack{i,j,k \leq n \\ i < j < k}} 27\alpha_{ijk}^{(n)} + \dots + 3^n \alpha_{12\dots n}^{(n)} \right), \quad (2.47)$$

where $\alpha_{ij\dots s}^{(n)}$ are the depolarizing strengths of the subspace specific channels in Eq. (2.37), and A is a normalization constant equal to

$$A = \sum_{\mathbb{P} \in \{\{\sigma_x, \sigma_y, \sigma_z\}\}^n} \text{Tr}(\mathbb{P}). \quad (2.48)$$

The factors in front of the depolarizing parameters count all the Pauli basis elements in the respective s -qubit subspace, i.e. all the possible permutations with repetition of tensor products of s operators from the set of Pauli operators $\{\sigma_x, \sigma_y, \sigma_z\}$. Note that all the Pauli basis elements in a given s -dimensional subspace have the same depolarizing parameter. This is a consequence of doing a complete twirl over $\mathcal{C}_1^{\otimes n}$, which leads *on average* to equivalent mixing rates along each basis vector in the s -dimensional Bloch sphere.

Experimentally, we can obtain each $\alpha_{ij\dots s}^{(n)}$ by measuring the expectation values of the s -qubit correlators $\langle \sigma_{z,i} \sigma_{z,j} \dots \sigma_{z,s} \rangle$, and fitting to the exponential decay in Eq. (2.28). Once we calculate $\bar{\alpha}_n$, we can define the multi-qubit average fidelity of the channel $\Lambda_{\mathcal{C}_1^{\otimes n}}$ with respect to the identity map $\mathbb{1}^{\otimes n}$ as [9]

$$\bar{F}(\Lambda_{\mathcal{C}_1^{\otimes n}}, \mathbb{1}^{\otimes n}) = \text{Tr} \left(M_n \Lambda_{\mathcal{C}_1^{\otimes n}} (\rho_{0,n}) \right) = 1 - \frac{(d-1)(1-\bar{\alpha}_n)}{d}, \quad (2.49)$$

where $d = 2^n$ is the dimension of the n -qubit Hilbert space, $\rho_{0,n} = (|0\rangle\langle 0|)^{\otimes n}$ is the initial density matrix, and $\hat{M}_n = (\mathbb{1}^{\otimes n} + \hat{\sigma}_z^{\otimes n})/d$ is the measurement operator which projects into the $+1$ eigenspace of the stabilizer $\hat{\sigma}_z^{\otimes n}$.

We can also define the *average multi-qubit channel infidelity* as the overlap between the n -qubit error channel and the identity map:

$$r(\Lambda_{\mathcal{C}_1^{\otimes n}}) = r_n = 1 - \bar{F}(\Lambda_{\mathcal{C}_1^{\otimes n}}, \mathbb{1}^{\otimes n}) = \frac{(2^n - 1)(1 - \bar{\alpha}_n)}{2^n}. \quad (2.50)$$

From here onward, I will refer to this last quantity as the *multi-qubit error* and I will always denote it by r_n .

In the remainder of this section, I will describe how the SRB formalism can be used to quantify the amounts of crosstalk and correlated errors in multi-qubit experiments, and to investigate what degree of correlated errors has the dominant effect in the multi-qubit system.

2.3.4 Investigating the amount of crosstalk with multi-qubit SRB

In the context of the SRB formalism, we define multi-qubit crosstalk as the increase in the infidelity of each single qubit error channel $\Lambda_i^{(n)}$ with n , the number of simultaneously operated qubits.

We calculate the infidelity $r_{1,i}^{(n)}$ associated with the error channel acting on the subspace of qubit i in the n -qubit SRB experiment as

$$r_{1,i}^{(n)} = 1 - \text{Tr}\left(M_i \Lambda_{C_1^{\otimes n}}(\rho_{0,n})\right) = \frac{1 - \alpha_i^{(n)}}{2}. \quad (2.51)$$

Here, the measurement operator $\hat{M}_i = (\mathbb{1} + \hat{\sigma}_{z,i})/2$ projects the final qubit state into the $+1$ eigenspace of the single qubit stabilizer $\hat{\sigma}_{z,i}$, and the depolarizing parameter, $\alpha_i^{(n)}$, is obtained from measurements of the single qubit observable $\hat{\sigma}_{z,i}$ for qubit i .

In Sec. 4, I will show and discuss the amount of crosstalk found by calculating $r_{1,i}^{(n)}$ for each qubit i in all combinations of SRB experiments on up to four qubits that were performed in this work.

2.3.5 Investigating the degree of correlated errors with multi-qubit SRB

In this section I will focus on n -qubit SRB experiments with $n \in \{1, 2, 3, 4\}$ in order to describe how the theory in Sec. 2.3.3 can be used to investigate whether the multi-qubit error channel implemented by the SRB protocol contains any correlations between the errors acting in the individual qubit subspaces. Formally, an n -qubit error channel \mathcal{E}_n , with an associated strength ϵ and n -qubit operator $\hat{\mathcal{O}}$, has the following action on the n -qubit density matrix $\hat{\rho}_n$:

$$\hat{\rho}_n \xrightarrow{\mathcal{E}_n} (1 - \epsilon)\hat{\rho}_n + \epsilon\hat{\mathcal{O}}\hat{\rho}_n\hat{\mathcal{O}}^\dagger. \quad (2.52)$$

\mathcal{E}_n is a correlated error channel if it cannot be written as a composition of n single qubit error channels, $\mathcal{E}_n \neq \mathcal{E}_1 \circ \mathcal{E}_2 \circ \dots \circ \mathcal{E}_n$.

We can further develop the theory in the previous section to characterize the degree of the correlated errors between different subspaces in the n -qubit algorithm. To this end, we can calculate lower bounds on the multi-qubit error under the assumption that it contains correlations of degree only up to $s < n$, and use these results to investigate what is the smallest correlated subspace s that will describe the true, experimentally-obtained multi-qubit error r_n that contains all degrees of correlations (Eqs. (2.47) and (2.50)). In this section I develop the theory for these characterization tools, and in Sec. 4 I will show and discuss the experimental results.

I will start by writing down the total multi-qubit depolarizing parameter in Eq. (2.47) for a 4-qubit SRB experiment:

$$\begin{aligned} \bar{\alpha}_4 = \frac{1}{255} & \left(3\alpha_1^{(4)} + 3\alpha_2^{(4)} + 3\alpha_3^{(4)} + 3\alpha_4^{(4)} + \right. \\ & 9\alpha_{12}^{(4)} + 9\alpha_{13}^{(4)} + 9\alpha_{14}^{(4)} + 9\alpha_{23}^{(4)} + 9\alpha_{24}^{(4)} + 9\alpha_{34}^{(4)} + \\ & \left. 27\alpha_{123}^{(4)} + 27\alpha_{124}^{(4)} + 27\alpha_{134}^{(4)} + 27\alpha_{234}^{(4)} + 81\alpha_{1234}^{(4)} \right), \end{aligned} \quad (2.53)$$

where each $\alpha_i^{(4)}$ are extracted from measuring the expectation values of the single qubit observables $\langle \sigma_{z,i} \rangle$ for all qubits $i \leq 4$, $\alpha_{ij}^{(4)}$ are extracted from measuring the expectation

values of the two-qubit correlators $\langle \sigma_{z,i} \sigma_{z,j} \rangle$, and so on. Notice that the ability to measure all combinations of s -qubit correlations for all $s \leq 4$ is required in order to measure all the depolarizing parameters in Eq. (2.53).

Below I will re-express the total error channel $\Lambda_{\mathcal{C}_1^{\otimes n}}$ and its associated total depolarizing parameter $\bar{\alpha}_n$ under various assumptions about which subspace contains correlated errors. I will use the notation $\tilde{\alpha}_{n,s}$ for the multi-qubit depolarizing parameters, where $s < n$ denotes the largest subspace where we assume to have correlations. I will then use Eq. (2.53) as a baseline against which to compare these quantities in order to make some theoretical predictions about what one would expect to find from calculating these objects.

2.3.5.1 Completely correlated errors

If we assume that all the errors in the different subspaces are completely correlated, then the average error channel $\bar{\mathcal{E}}_{\otimes n}$ implemented by SRB describes the full n -qubit depolarizing channel, $\Lambda_{\mathcal{C}_n}$, obtained by twirling with the full n -qubit Clifford group, \mathcal{C}_n . In this case, all subspaces will depolarize at the same rate given by the depolarizing parameter $\alpha_{ij...s}^{(n)} = \alpha_{12...n}^{(n)}$, for all $s \leq n$.

This case is added here for completion. We did not perform this experiment, since twirling over the whole n -qubit Clifford group becomes experimentally unfeasible for $n = 4$ (the number of elements in the full 2-qubit Clifford group is already 11520; see [37] for details). We also did not investigate this assumption in our analysis of the SRB results, since it is unlikely that the error channel $\Lambda_{\mathcal{C}_1^{\otimes n}}$ associated with n simultaneously applied single qubit Clifford elements contains only n -qubit correlations, i.e. that the multi-qubit error is a perfectly entangling gate.

2.3.5.2 Completely uncorrelated errors

If the errors in all the individual s -qubit subspaces are completely uncorrelated, then the total error channel can be written as $\bar{\mathcal{E}}_{\otimes n} = \bar{\mathcal{E}}_1 \circ \bar{\mathcal{E}}_2 \circ \dots \circ \bar{\mathcal{E}}_n$. This implies that each subspace-specific depolarizing channel in Eq. (2.37) depolarizes each single qubit subspace independently. Thus, we can write

$$\Lambda_{\mathcal{C}_1^{\otimes n}} = \Lambda_1^{(n)} \circ \Lambda_2^{(n)} \circ \dots \circ \Lambda_n^{(n)}, \quad (2.54)$$

where $\Lambda_i^{(n)}$ denotes the depolarizing channel acting only in the subspace of qubit i in the n -qubit SRB experiment. As a result, we can also write each $\alpha_{12...s}^{(n)} = \alpha_1^{(n)} \alpha_2^{(n)} \dots \alpha_s^{(n)}$ for $s \leq n$, where $\alpha_i^{(n)}$ is the *measured* depolarizing parameter acting only on the subspace of qubit i in the n -qubit SRB experiment. Eq. (2.47) then becomes

$$\tilde{\alpha}_{n,1} = \frac{1}{A} \left(\sum_{i \leq n} 3\alpha_i^{(n)} + \sum_{\substack{i,j \leq n \\ i < j}} 9\alpha_i^{(n)} \alpha_j^{(n)} + \sum_{\substack{i,j,k \leq n \\ i < j < k}} 27\alpha_i^{(n)} \alpha_j^{(n)} \alpha_k^{(n)} + \dots + 3^n \alpha_1^{(n)} \alpha_2^{(n)} \dots \alpha_n^{(n)} \right), \quad (2.55)$$

and, in particular, for the 4-qubit SRB experiment we have

$$\begin{aligned} \tilde{\alpha}_{4,1} = & \frac{1}{255} \left(3\alpha_1^{(4)} + 3\alpha_2^{(4)} + 3\alpha_3^{(4)} + 3\alpha_4^{(4)} + \right. \\ & 9\alpha_1^{(4)}\alpha_2^{(4)} + 9\alpha_1^{(4)}\alpha_3^{(4)} + 9\alpha_1^{(4)}\alpha_4^{(4)} + 9\alpha_2^{(4)}\alpha_3^{(4)} + 9\alpha_2^{(4)}\alpha_4^{(4)} + 9\alpha_3^{(4)}\alpha_4^{(4)} + \\ & 27\alpha_1^{(4)}\alpha_2^{(4)}\alpha_3^{(4)} + 27\alpha_1^{(4)}\alpha_2^{(4)}\alpha_4^{(4)} + 27\alpha_1^{(4)}\alpha_3^{(4)}\alpha_4^{(4)} + 27\alpha_2^{(4)}\alpha_3^{(4)}\alpha_4^{(4)} + \\ & \left. 81\alpha_1^{(4)}\alpha_2^{(4)}\alpha_3^{(4)}\alpha_4^{(4)} \right). \end{aligned} \quad (2.56)$$

Ideally, we would like to have no correlated errors in our n -qubit algorithm. To investigate if this is the case, we notice that we would expect to find $\bar{\alpha}_n = \tilde{\alpha}_{n,1}$ if the errors are completely uncorrelated. Therefore, we calculate the quantity $\Delta\bar{\alpha}_n = \bar{\alpha}_n - \tilde{\alpha}_{n,1}$, or equivalently $\Delta r_n = \tilde{r}_{n,1} - r_n$, where $\tilde{r}_{n,1}$ is the completely uncorrelated multi-qubit error given by

$$\tilde{r}_{n,1} = \frac{(2^n - 1)(1 - \tilde{\alpha}_{n,1})}{2^n}. \quad (2.57)$$

Then the presence of correlated errors will be signaled by checking the following conditions:

$$\begin{aligned} \Delta r_n = 0 & \rightarrow \text{no observed correlated errors,} \\ \Delta r_n > 0 & \rightarrow \text{some correlated errors,} \\ \Delta r_n = \tilde{r}_{n,1} - r_n. & \end{aligned} \quad (2.58)$$

If there are correlated errors, the quantities $\Delta\bar{\alpha}_n$ and Δr_n as defined above will always be positive because it is always true that $\alpha_{12\dots s} \geq \alpha_1\alpha_2\dots\alpha_s$, for all $s \leq n$. I will prove this statement for an $n = 2$ -qubit SRB experiment in Appendix B, and I will give an intuitive explanation for this inequality in Sec. 4.2.

Next we will focus on the 4-qubit SRB experiment and consider the case $\Delta\bar{\alpha}_4 > 0$, i.e. we cannot interpret our measured $\alpha_{ij\dots s}^{(4)}$ as simply being the uncorrelated product $\alpha_i^{(4)}\alpha_j^{(4)}\dots\alpha_s^{(4)}$ for all $s \leq 4$. Consequently, we can investigate whether the quantity $\bar{\alpha}_4$ calculated from all correlators can be fully explained by $\tilde{\alpha}_{4,2}$ calculated only from the depolarizing parameters $\alpha_i^{(4)}$ and $\alpha_{ij}^{(4)}$, which capture the effects of uncorrelated errors and 2-qubit correlated errors. If this is also not the case, we can further investigate how well we can explain $\bar{\alpha}_4$ by also including the 3-qubit correlators, i.e. we consider $\tilde{\alpha}_{4,3}$ which is calculated only from the depolarizing parameters $\alpha_i^{(4)}$, $\alpha_{ij}^{(4)}$, and $\alpha_{ijk}^{(4)}$ describing 1-, 2-, and 3-qubit correlations. To investigate these effects theoretically, we first rewrite $\Lambda_{C_1^{\otimes n}}$ in a more general framework from which we can derive the 4-qubit errors in the two cases mentioned above.

2.3.5.3 Subspace specific correlated errors

The most general theoretical model of the n -qubit SRB protocol should describe the map $\Lambda_{C_1^{\otimes n}}$ as a weighted sum of the completely correlated n -qubit error channel Λ_{C_n} , the completely uncorrelated n -qubit error channel, $\Lambda_1 \otimes \Lambda_2 \otimes \dots \otimes \Lambda_n$, and all the n -qubit error channels where only the s -dimensional subspace is fully correlated, for all $s < n$. For example, if we denote $\Lambda_{C_n} = \Lambda_{12\dots n}$, the channels for the 2-, 3-, and 4-qubit SRB

experiments are written in this new framework as:

$$\Lambda_{C_1^{\otimes 2}} = a_2 \Lambda_{12} + b_2 (\Lambda_1 \circ \Lambda_2), \quad (2.59)$$

$$\begin{aligned} \Lambda_{C_1^{\otimes 3}} = a_3 \Lambda_{123} + b_3 (\Lambda_1 \circ \Lambda_{23}) + c_3 (\Lambda_2 \circ \Lambda_{13}) + d_3 (\Lambda_3 \circ \Lambda_{12}) + \\ e_3 (\Lambda_1 \circ \Lambda_2 \circ \Lambda_3), \end{aligned} \quad (2.60)$$

$$\begin{aligned} \Lambda_{C_1^{\otimes 4}} = a_4 \Lambda_{1234} + \\ b_4 (\Lambda_1 \circ \Lambda_{234}) + c_4 (\Lambda_2 \circ \Lambda_{134}) + d_4 (\Lambda_3 \circ \Lambda_{124}) + e_4 (\Lambda_4 \circ \Lambda_{123}) + \\ f_4 (\Lambda_{12} \circ \Lambda_{34}) + g_4 (\Lambda_{13} \circ \Lambda_{24}) + h_4 (\Lambda_{14} \circ \Lambda_{23}) \circ \\ t_4 (\Lambda_1 \circ \Lambda_2 \circ \Lambda_{34}) + u_4 (\Lambda_{12} \circ \Lambda_3 \circ \Lambda_4) + v_4 (\Lambda_1 \circ \Lambda_3 \circ \Lambda_{24}) + \\ w_4 (\Lambda_{13} \circ \Lambda_2 \circ \Lambda_4) + x_4 (\Lambda_1 \circ \Lambda_4 \circ \Lambda_{23}) + y_4 (\Lambda_{14} \circ \Lambda_2 \circ \Lambda_3) + \\ z_4 (\Lambda_1 \circ \Lambda_2 \circ \Lambda_3 \circ \Lambda_4). \end{aligned} \quad (2.61)$$

Here, the prefactors indicate the strength of each type of depolarizing effect in the full $\Lambda_{C_1^{\otimes n}}$ channel, and normalization requires the conditions $a_n + b_n + \dots = 1$ for all $n \in \{2, 3, 4\}$. Each of the channels $\Lambda_{ij...s}$ in Eqs. (2.59), (2.60), (2.61) are theoretical objects used only in the context of this description in order to indicate the presence of the different types of error correlations in the total n -qubit channel; they are not measured quantities. Indeed, our 4-qubit SRB experiment does not grant us access to all these quantities. In particular, all $\Lambda_{ij...s}$ with $s > 1$ are theoretical quantities that denote the completely correlated s -qubit channels Λ_{C_s} , which are experimentally inaccessible by the SRB protocol.

We will now focus on the 4-qubit SRB experiment. Each *measured* depolarizing parameter $\alpha_{ij...s}^{(4)}$ is still obtained from measuring the s -qubit correlators $\langle \sigma_{z,i} \sigma_{z,j} \dots \sigma_{z,s} \rangle$. Using Eq. (2.61) we can express each of these measured quantities in terms of some undetermined theoretical depolarizing parameters $\alpha_{ij...s}$ corresponding to each of the theoretical depolarizing channels $\Lambda_{ij...s}$ in Eq. (2.61). For example, the measured parameter $\alpha_{12}^{(4)}$ in the 4-qubit SRB experiment is given by

$$\begin{aligned} \alpha_{12}^{(4)} = a_4 \alpha_{1234} + \\ b_4 \alpha_{1234} + c_4 \alpha_{234} + d_4 \alpha_{134} + e_4 \alpha_{124} + \\ f_4 \alpha_{12} + g_4 \alpha_{13} + h_4 \alpha_{14} + \\ t_4 \alpha_{12} + u_4 \alpha_{13} + v_4 \alpha_{14} + \\ w_4 \alpha_{12} + x_4 \alpha_{13} + y_4 \alpha_{14} + \\ z_4 \alpha_{12}. \end{aligned} \quad (2.62)$$

Analyzing the 4-qubit experiment in this more general framework allows us to investigate the multi-qubit depolarizing parameter $\bar{\alpha}_4$ from Eq. (2.53) in cases where the errors are correlated only in certain qubit subspaces but not in others.

Only single qubit errors and 2-qubit correlated errors

If the largest subspace that has correlated errors is the 2-qubit subspace, then $a_4 = b_4 = c_4 = d_4 = e_4 = 0$ in Eqs. (2.61) and (2.62). We obtain the multi-qubit depolarizing

parameter $\tilde{\alpha}_{4,2}$ for the 4-qubit channel $\Lambda_{C_1^{\otimes 4}}$ containing only up to 2-qubit correlations by expressing all remaining non-zero terms in Eq. (2.53) in a similar form as in Eq. (2.62). Collecting like terms, we obtain

$$\begin{aligned} \tilde{\alpha}_{4,2} = \frac{1}{A} & \left[\sum_{i \leq 4} x_i \alpha_i + \right. \\ & \sum_{\substack{ij \leq 4 \\ i < j}} (x_{ij} \alpha_{ij} + \tilde{x}_{ij} \alpha_i \alpha_j) + \\ & \sum_{\substack{ijk \leq 4 \\ i < j < k}} (x_{ijk} \alpha_i \alpha_j \alpha_k + \tilde{x}_{ijk} \alpha_i \alpha_j \alpha_k) + \\ & \left. \sum_{\substack{ijkl \leq 4 \\ i < j < k < l}} (x_{ijkl} \alpha_{ij} \alpha_{kl} + \tilde{x}_{ijkl} \alpha_i \alpha_j \alpha_k \alpha_l + x'_{ijkl} \alpha_i \alpha_j \alpha_k \alpha_l) \right], \end{aligned} \quad (2.63)$$

where the prefactors $x_{ij...s}$, $\tilde{x}_{ij...s}$, and x'_{ijkl} are unknown constants denoting the weight of each term in each sum. Determining all these prefactors would give us access to all the information about how much of each degree of correlated errors occurs in the 4-qubit experiment. However, this system of equations is overdetermined; we only measure 14 depolarizing parameters $\alpha_{ij...s}^{(4)}$, $s \leq 4$, but we have many more unknown prefactors in Eq. (2.63). However, since we are primarily interested in determining the minimum type of error correlations (2-qubit, 3-qubit, or 4-qubit) that will completely describe our measured $\bar{\alpha}_4$, we will take the following approach. In order to see if assuming only 2-qubit correlations is enough to explain the observed $\bar{\alpha}_4$ containing all degrees of correlations, we will express all the measured $\alpha_{ijk}^{(4)}$ and $\alpha_{1234}^{(4)}$ in terms of only the measured single qubit parameters $\alpha_i^{(4)}$, and the 2-qubit-correlated parameters $\alpha_{ij}^{(4)}$. Using now only these measured quantities in Eq. (2.63), the total depolarizing parameter $\tilde{\alpha}_{4,2}$ becomes:

$$\begin{aligned} \tilde{\alpha}_{4,2} = \frac{1}{A} & \left[\sum_{i \leq 4} 3 \alpha_i^{(4)} + \sum_{\substack{ij \leq 4 \\ i < j}} 9 \alpha_{ij}^{(4)} + \right. \\ & \sum_{\substack{ijk \leq 4 \\ i < j < k}} \left(x_{ijk} \alpha_i^{(4)} \alpha_j^{(4)} + \tilde{x}_{ijk} \alpha_i^{(4)} \alpha_j^{(4)} \alpha_k^{(4)} \right) + \\ & \left. \sum_{\substack{ijkl \leq 4 \\ i < j < k < l}} \left(x_{ijkl} \alpha_{ij}^{(4)} \alpha_{kl}^{(4)} + \tilde{x}_{ijkl} \alpha_i^{(4)} \alpha_j^{(4)} \alpha_{kl}^{(4)} + x'_{ijkl} \alpha_i^{(4)} \alpha_j^{(4)} \alpha_k^{(4)} \alpha_l^{(4)} \right) \right]. \end{aligned} \quad (2.64)$$

Instead of minimizing this system of equations in order to find the unknown prefactors, we will estimate an upper bound of $\tilde{\alpha}_{4,2}$ by calculating

$$\begin{aligned} \tilde{\alpha}_{4,2}^{\max} = & \frac{1}{255} \left[\sum_{i \leq 4} 3\alpha_i^{(4)} + \sum_{\substack{ij \leq 4 \\ i < j}} 9\alpha_{ij}^{(4)} + \right. \\ & \sum_{\substack{ijk \leq 4 \\ i < j < k}} 27 \max\left(\alpha_i^{(4)}\alpha_{jk}^{(4)}, \alpha_i^{(4)}\alpha_j^{(4)}\alpha_k^{(4)}\right) + \\ & \left. 81 \max\{\alpha_{ij}^{(4)}\alpha_{kl}^{(4)}, \alpha_i^{(4)}\alpha_j^{(4)}\alpha_{kl}^{(4)}, \alpha_i^{(4)}\alpha_j^{(4)}\alpha_k^{(4)}\alpha_l^{(4)}\}_{\substack{ijkl \leq 4 \\ i < j < k < l}} \right]. \end{aligned} \quad (2.65)$$

If the equation above gives $\tilde{\alpha}_{4,2}^{\max} = \bar{\alpha}_4$ within the experimental error bars, then it is an indication that the effects from correlated errors between more than 2 qubits might have a negligibly small contribution to our error channel compared to the effects from 2-qubit correlated errors. Hence, it would suggest that including only 2-qubit correlated errors in our model for $\bar{\alpha}_4$ is a sufficiently good description of the observed multi-qubit error.

If, on the other hand, we calculate Eq. (2.65) and obtain within the error bars that $\tilde{\alpha}_{4,2}^{\max} < \bar{\alpha}_4$ (or equivalently, $\tilde{r}_{4,2}^{\max} > \bar{r}_4$), then we can conclude with certainty that 2-qubit correlated errors are not the only types of correlations in our system, and thus that it is also important to consider higher order correlations. Obtaining a model that includes both 2- and 3-qubit correlated errors is the topic of the next section.

Single qubit errors and both 2- and 3-qubit correlated errors

If the largest subspace that has correlated errors is the 3-qubit subspace, then only $a_4 = 0$ in Eqs. (2.61) and (2.62). Proceeding like we did in the previous section, we can write the most general form of the total depolarizing parameter that includes 2- and 3-qubit correlations as

$$\tilde{\alpha}_{4,3} = \tilde{\alpha}_{4,2} + \frac{1}{A} \left(\sum_{\substack{ijk \leq 4 \\ i < j < k}} x'_{ijk} \alpha_{ijk} + \sum_{\substack{ijkl \leq 4 \\ i < j < k < l}} x''_{ijkl} \alpha_i \alpha_{jkl} \right), \quad (2.66)$$

with $\tilde{\alpha}_{4,2}$ from Eq. (2.63), and the unknown prefactors x'_{ijk} and x''_{ijkl} as explained in the previous section.

As before, we again only estimate the upper bound of $\tilde{\alpha}_{4,3}$ by calculating $\tilde{\alpha}_{4,3}^{\max}$ from the measured single qubit depolarizing parameters $\alpha_i^{(4)}$, and the ones that describe 2- and 3-qubit correlations, $\alpha_{ij}^{(4)}$ and $\alpha_{ijk}^{(4)}$, respectively:

$$\begin{aligned} \tilde{\alpha}_{4,3}^{\max} = & \frac{1}{255} \left[\sum_{i \leq 4} 3\alpha_i^{(4)} + \sum_{\substack{ij \leq 4 \\ i < j}} 9\alpha_{ij}^{(4)} + \sum_{\substack{ijk \leq 4 \\ i < j < k}} 27\alpha_{ijk}^{(4)} + \right. \\ & \left. 81 \max\{\alpha_i^{(4)}\alpha_{jkl}^{(4)}, \alpha_{ij}^{(4)}\alpha_{kl}^{(4)}, \alpha_i^{(4)}\alpha_j^{(4)}\alpha_{kl}^{(4)}, \alpha_i^{(4)}\alpha_j^{(4)}\alpha_k^{(4)}\alpha_l^{(4)}\}_{\substack{ijkl \leq 4 \\ i < j < k < l}} \right]. \end{aligned} \quad (2.67)$$

If we obtain $\tilde{\alpha}_{4,3}^{\max} = \bar{\alpha}_4$ within the error bars, then it is an indication that our system might contain only 2- and 3-qubit correlated errors, and that the model described by Eq. (2.67) explains our system well enough that we do not have to also consider effects from 4-qubit correlated errors.

If, however, $\tilde{\alpha}_{4,3}^{\max} < \bar{\alpha}_4$ ($\tilde{r}_{4,3}^{\max} > \bar{r}_4$), then we can conclude that effects from higher order correlations are also statistically significant, and we should proceed to include them in our analysis. However, since the qubits used in our experiments were either pairwise coupled by a bus resonator or physically uncoupled (see Sec. 2.1.1 and Sec. 3.1), we do not expect to find strong 3- and 4-qubit correlated errors in our algorithm, and hence we expect to find that our system contains predominantly 2-qubit correlated errors.

3 Experimental Implementation

In this section I will describe how the single qubit randomized benchmarking (RB) and the multi-qubit simultaneous RB (SRB) experiments described in the previous section were implemented in the lab. I will start with a brief description of our room-temperature experimental setup, and some of the digital signal processing techniques that were used to manipulate and read out the qubits. I will emphasize the features of our detection instrument, the Zurich Instruments (ZI) Ultra High Frequency Lock-In Quantum Controller (UHFLI-QC), that we used to achieve fast multiplexed single-shot readout of the individual qubits and their correlators for the SRB experiments.

I will then explain the concept and our implementation of virtual Z (VZ) gates, introduced by McKay et al. [2]. As a small digression from RB, I will emphasize the usefulness of the VZ gates by describing how they can be used to correct the single qubit dynamic phases acquired by each qubit during a fluxing operation (see Sec. 2.2.1 for a discussion of flux line crosstalk). Then I will discuss how the VZ gates were used during this project to decompose the single qubit Clifford group into single qubit primitive gates using the HVZ decomposition introduced in Ref. [2]. I compare the results from performing standard RB on qubits 3, 4, 5, and 7, using both the HVZ and the traditional $XY_{\frac{\pi}{2}}$ [19] decompositions, and then I will show and discuss results from interleaved RB (IRB) with both VZ and real gates as interleaved gates.

3.1 Description of the multi-qubit setup

In this section I will describe the experimental setup and in particular the features of the detection instrument that were used to successfully measure SRB on up to four qubits. The four qubits used in our experiments were qubits 3, 4, 5, and 7, denoted by qb3, qb4, qb5, and qb7. Their placement on the quantum processor was shown in Fig. 2.1 and is also illustrated here schematically in Fig. 3.1 (a); see Sec. 2.1.1 for details about the processor. For all the SRB experiments presented in the last section of this work, these qubits were parked at their sweet spots given by the approximate frequencies $\{6.20, 6.27, 6.11, 6.12\}$ GHz for $\{qb3, qb4, qb5, qb7\}$, respectively; see the diagram in Fig. 3.1 (b) showing the important frequency components in the setup. At these parking positions, the qubits had energy relaxation times, T_1 , of approximately $\{4.5, 3.0, 1.1, 3.1\}$ μ s and dephasing times, T_2 , obtained from Echo measurements of approximately $\{7.2, 5.7, 2.2, 5.3\}$ μ s.

Fig. 3.1 (a) also shows the instruments that were used to operate and read out the qubits in the (S)RB experiments. The real and imaginary components of the pulse sequences used to drive each qubit are generated in software and uploaded onto the corresponding channels of the arbitrary waveform generators (AWGs). In our setup, qubits 4 and 5 use the channel pairs Ch3-Ch4 and Ch1-Ch2 of AWG1, respectively, while qubits 3 and 7 use the channels pairs Ch3-Ch4 and Ch1-Ch2 of AWG2, respectively. These pulses are generated at relatively low frequencies called the *drive intermediate frequencies* (IFs). In order to drive each qubit on resonance, these low IFs must be increased or *upconverted* to reach each qubit's frequency of around 6 GHz. This upconversion process is achieved with an *IQ mixer*. The mixer generates a complex-valued pulse-shape by multiplying a high frequency *local oscillator* (LO) tone with two signals at the IF frequency: the real, or *in-phase* (I) component with zero phase, and the imaginary, or *quadrature* (Q) component with a phase of 90° . In Fig. 3.1 (a) we see that the I and Q pulses are provided by the

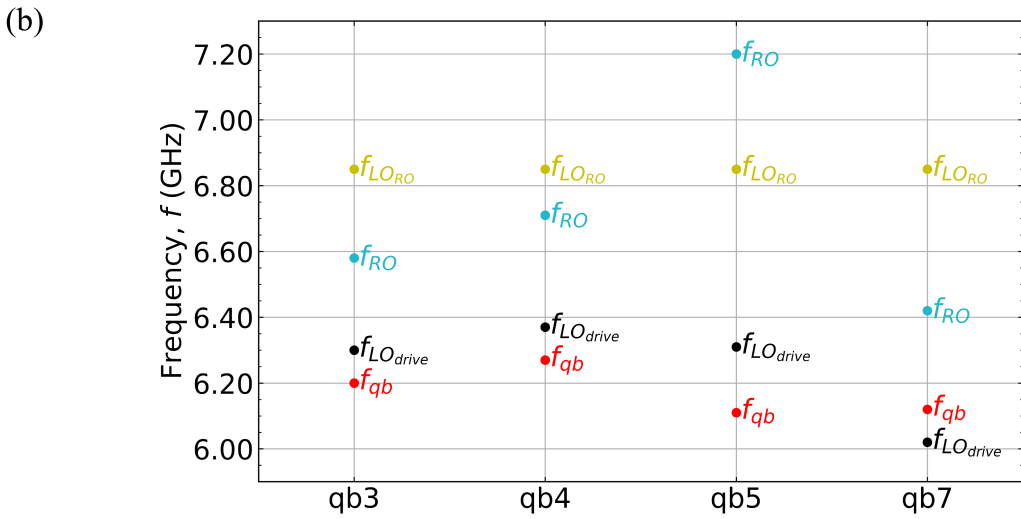
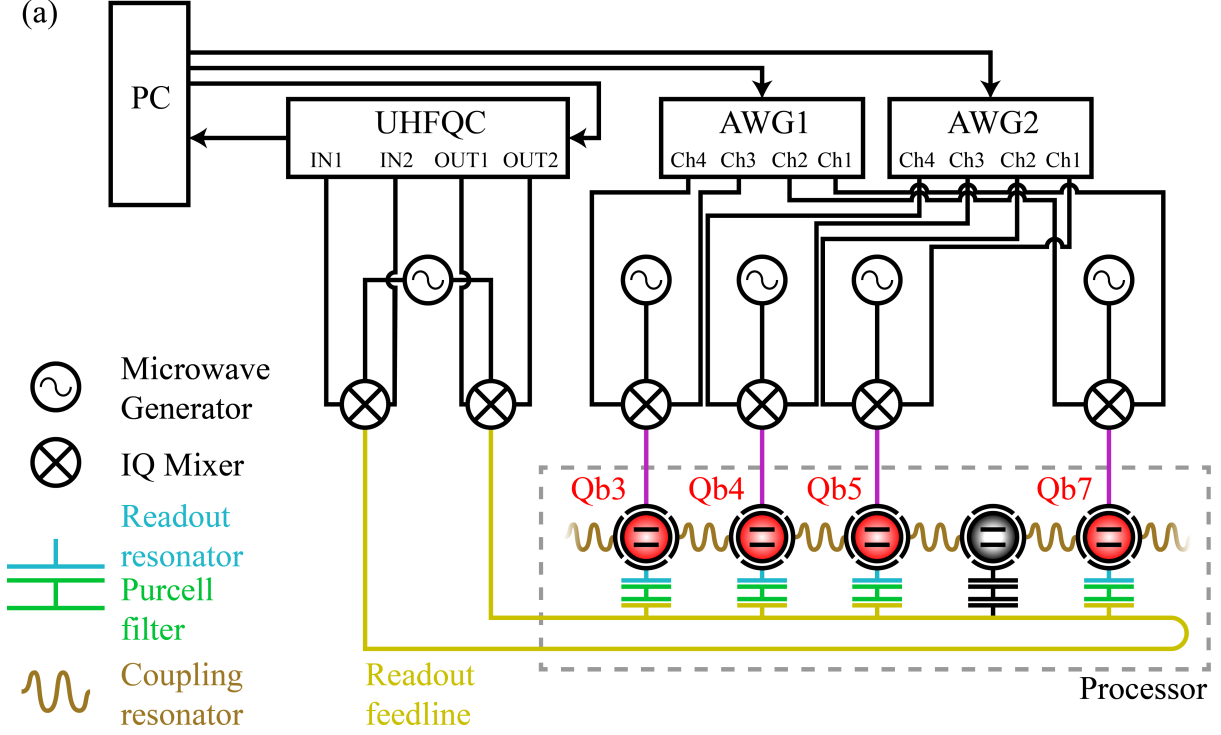


Figure 3.1: (a) The four qubits used in the experiments presented in this work and the room-temperature control instruments. The qubits are schematically illustrated by the red circles denoting two-level systems. The gray qubit is qubit 6, which was not used in our SRB experiments. See Sec. 2.1.1 for details about the processor. The flux lines were omitted in this illustration since they were not used during the SRB experiments. The two arbitrary waveform generators (AWGs) are identical Tektronix 5014 instruments, and all microwave generators are Rohde Schwarz SGS100A instruments. The roles of these control instruments are described in the main text. (b) Diagram showing the important frequency components in the experimental setup. The parking positions of the four qubits used in the SRB experiments are shown in red, and their readout frequencies are shown in blue. The local oscillator (LO) frequencies used for upconverting each qubit's drive signal, and for up- and downconverting the multiplexed readout signal are shown in black and yellow, respectively.

AWGs, and the LO signal is provided by a different microwave generator (MWG) for each qubit. The radio frequency signal at the output of the mixer, referred to as the *RF signal*, has the amplitude $I(t)\cos(2\pi ft) + Q(t)\sin(2\pi ft)$, and the frequency $f = f_{\text{LO}} + f_{\text{IF}} = f_{\text{qb}}$, which is tuned to be resonant with the qubit it will be applied to. For more details about IQ mixers and about how they are used in quantum computing setups, see Refs. [23, 42].

When we tune up the setup, we first park the qubits at the desired frequencies, then we choose drive IFs for each qubit i , and finally we calculate the LO frequencies as $f_{\text{LO},i} = f_{\text{qb},i} - f_{\text{IF},i}$. The reason for using waves at f_{IF} for the I and Q ports instead of DC voltages, is to detune the LO frequency from the resulting qubit drive pulse, and thus avoid that the qubit is driven by leakage of the LO signal into the RF port [23]. The IF frequencies must be chosen within the bandwidth of the AWG of a few hundred MHz; hence, typical values for this detuning are $f_{\text{IF}} = \pm 100$ MHz. In multi-qubit experiments, it is also important to ensure that potential leakage of the various LO signals is not resonant with any of the qubit frequencies. Hence, the drive LOs used in the SRB experiments are shown in Fig. 3.1 (b), with drive IFs of -100 MHz for qubits 3 and 4, -200 MHz for qubit 5, and 100 MHz qubit 7.

As shown in Fig. 3.1 (a), all qubits capacitively couple to the same readout feedline (yellow). As already described in Sec. 2.1.2, this design allows us to dispersively read out all or any subset of the qubits simultaneously with high fidelity using composite multiplexed readout pulses. These pulses are compiled in software and uploaded to the AWG unit inside the Ultra High Frequency Lock-In (UHFQI) instrument running the Quantum Controller (QC) firmware developed by Zurich Instruments for quantum computing research (see Fig. 3.2). For short, I will refer to this instrument as the "UHFQC." The UHFQC outputs the in-phase and quadrature components of the readout pulse at a low frequency called the *readout IF*. These components are then similarly upconverted to the readout resonator frequencies corresponding to each qubit. The optimal readout frequency of each qubit that gives the highest signal-to-noise ratio (SNR) is found by measuring the transmission spectrum of the resonator when the corresponding qubit is in the excited state and comparing it to the spectrum measured when the qubit is in the ground state. Then the optimal readout frequency is given by the point on the spectrum that is most sensitive to the dispersive shift (see Sec. 2.1.1). More details about this measurement can be found in Ref. [29]. Fig. 3.1 (b) shows the optimized readout frequencies of our four qubits at approximately $\{6.58, 6.71, 7.20, 6.42\}$ GHz for $\{\text{qb3}, \text{qb4}, \text{qb5}, \text{qb7}\}$, respectively.

In order to do multiplexed readout, we must choose a single LO frequency to upconvert different qubit IFs to the respective readout frequencies, since we use only one MWG that produces the LO signal at a fixed frequency (see Fig. 3.1). In addition, we must choose an LO such that all the IFs are within the bandwidth of the UHFQC of 1.2 GHz, and such that the absolute values of the IFs calculated from $|f_{\text{RO},i} - f_{\text{LO}}|$ are as spaced out as possible for each resonator i . The latter condition is required in order to minimize readout crosstalk due to potential spectral overlap of the different frequency components in this composite signal, which would be upconverted to a readout pulse with spurious frequency components (see Sec. 2.2.2). The readout LO used in the SRB experiments was $f_{\text{LO,RO}} \simeq 6.85$ GHz, and is shown in yellow in Fig. 3.1 (b).

The upconverted readout signal is sent through the readout transmission line to probe the resonator of each qubit. The role of the Purcell filters, see Fig. 3.1 (a), in reducing readout crosstalk was discussed in Sec. 2.2.2. At the other end of the feedline, the high frequency signal must be decreased or *downconverted* back to a few hundred MHz within

the bandwidth of the UHFQC. Downconversion is also achieved with an IQ mixer, where now the input signal comes in through the RF port and is downconverted using the LO signal to two low-frequency I and Q components [42]. Notice in Fig. 3.1 (a) that the same MWG is used to provide the LO signal for both the up- and downconversion IQ mixers. This configuration is used to perform *homodyne* detection [43]. Unlike *heterodyne* detection where two different MWGs are used, the homodyne setup avoids any issues from possible phase miss-matches between the two MWGs.

The I and Q components of the downconverted readout signal are then received and digitized by the UHFQC. This instrument then proceeds to split up each component into several different channels, and to perform separate weighted integration of the real and imaginary parts of each channel, see Fig. 3.2. In this work we used one UHFQC readout channel per qubit and mode-matched integration weights which are optimized to achieve the highest SNR from the digitized transmission signal. These weights are specific to each qubit and are obtained from measuring the averaged timetraces of the readout resonator response when the qubit is in the ground state and when it is in the excited state. The mode-matched integration weights are then given by the complex conjugate of the difference between these traces [29]. The integrated real and imaginary components are then added together with the weights w_{Re} and w_{Im} respectively, which then gives the total integrated signal as [29]:

$$S_{\text{int}} = \sum_k \left[w_{\text{Re}} \text{Re}(w_k D_k) + w_{\text{Im}} \text{Im}(w_k D_k) \right]. \quad (3.1)$$

Here, w_k and D_k are the k^{th} samples of the mode-matched weights and the digitized readout signal, respectively. For all SRB measurements in this work, we used $w_{\text{Re}} = 1$ and $w_{\text{Im}} = -1$. See Ref. [29] for more detailed descriptions of mode-matched integration and our detection scheme in general.

In order to measure the $\hat{\sigma}_z^{\otimes s}$ correlators between all subsets of $s \leq n$ qubits in an n -qubit SRB experiment, we must be able to multiply the individual measurement results, or *shots*, for each qubit before averaging the shots to obtain the expectation values of the correlators (see Sec. 2.3.3). In order to implement this procedure, we measured all SRB experiments using *single-shot readout* and we used one readout channel per qubit as explained above. Using two channels per qubit means that the real and imaginary components of the integrated signal are stored and analyzed in software independently. In principle, we could have used this technique and then proceeded to combine the integrated results from the two channels in the data analysis before determining the state of the qubit in each shot, and before multiplying the shots together to obtain the correlators. However, as will be described below, we made use of the *thresholding* and *correlator* features of the UHFQC to achieve data reduction, qubit state discrimination, and shot-by-shot multiplication directly in our detection instrument. Hence, it was necessary to combine the real and imaginary parts of the signal directly in the UHFQC in order to use these features.

As mentioned above, it is important to use single-shot readout in order to measure the s -qubit correlators, $\hat{\sigma}_z^{\otimes s}$. In this type of readout, the state of a qubit is determined from one single acquisition of the signal from the readout feedline. In order to distinguish reliably between the ground and excited states of the qubit, it is important to be able to read out the complex transmission signal coming from the readout feedline with a high SNR. We fulfilled this requirement by optimizing the readout frequency of each qubit and by using mode-matched filters for each qubit readout channel as explained above. After

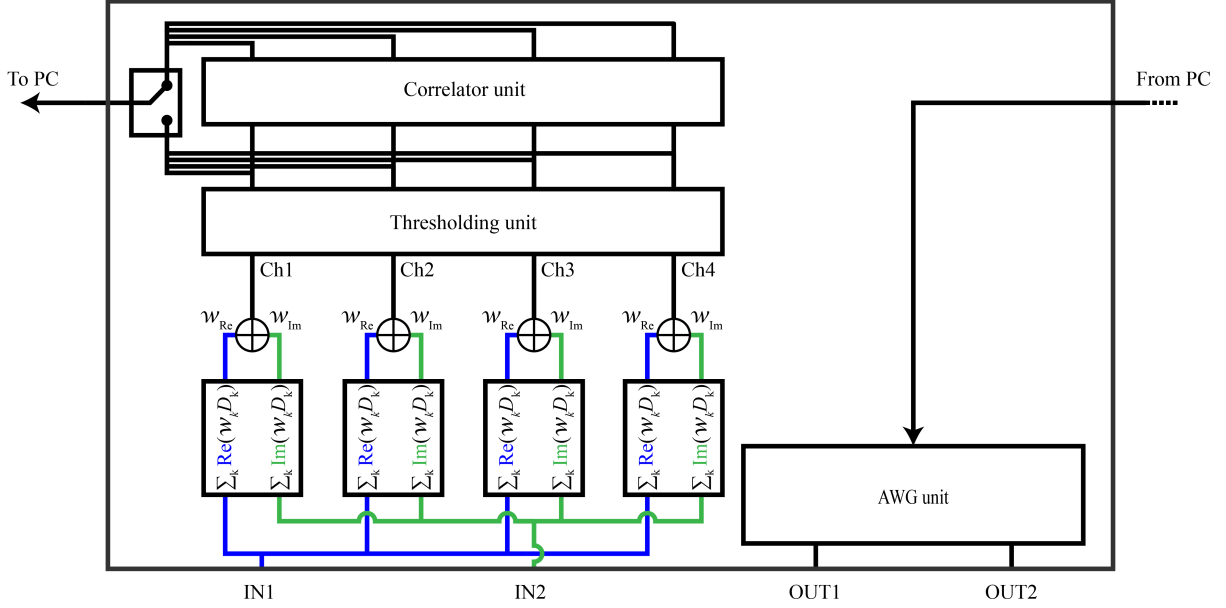


Figure 3.2: Main processing units in the UHFQC that were relevant for measuring the SRB experiments. The AWG unit in the bottom right is used to generate the I and Q signals for the readout upconversion mixer. The four blocks in the bottom left are the weighted integration units which integrate the real (IN1, blue) and imaginary (IN2, green) parts of the complex readout signal. The UHFQC can be configured to send the integrated signal to the PC directly after it is thresholded, or after it goes through both the thresholding and correlator units. See main text for details about these last two features.

also optimizing the readout power as explained in Ref. [29], we obtained the *assignment fidelities* {91.4%, 78.8%, 83.4%, 92.3%} for {qb3, qb4, qb5, qb7}, respectively.

The assignment fidelity F_a is obtained by plotting the histograms of a large number of shots when the qubit is prepared in the ground and the excited states as a function of the integrated signal, S_{int} . Fig. 3.3 shows these histograms for the four qubits used in the SRB experiments performed in this thesis, where the qubit was prepared in the ground state for purple and in the excited state for blue, and the dashed blue and purple lines are fits to double-Gaussians. The assignment fidelity represents the probability to assign the correct qubit state in each shot and is calculated as [29]

$$F_a = 1 - \frac{1}{2} \left[P(e_{\text{assign}}|g_{\text{prep}}) - P(g_{\text{assign}}|e_{\text{prep}}) \right], \quad (3.2)$$

where the last two quantities are the probabilities of incorrect state assignment. In typical single-shot calibration measurements such as those in Fig. 3.3 (a) and (d), these probabilities can be seen as the smaller Gaussians of each color. For qubits 4 and 5, there is a relatively high chance for a qubit prepared in the excited state to be assigned to either the ground or excited states. For qubit 5, this result occurs because the qubit decays to the ground state and loses coherence during state preparation and measurement due to its very low coherence times ($T_1 \simeq 1 \mu\text{s}$, $T_2 \simeq 2 \mu\text{s}$). For qubit 4, this behavior became more pronounced with higher readout powers, where its readout resonator is populated with a larger number of photons, n . As n becomes larger and approaches the *critical photon number* $n_{\text{critical}} = \Delta\omega_{q,r}^2/4g_{01}^2$, the dispersive approximation that allows us to perform QND measurements starts to break down [26, 29]; see Sec. 2.1.1 for a description of the notation used for n_{critical} . Consequently, the qubit state starts to become mixed, or

hybridized with that of the readout resonator. This behavior causes the qubit to decohere and to lead to the results in Fig. 3.3 (b). On the other hand, higher readout power leads to both a higher SNR and a better resolution of the Gaussians corresponding to the ground and excited states. Hence, for qubit 4 we settled for the compromise shown here, which gives us the assignment fidelity quoted above.

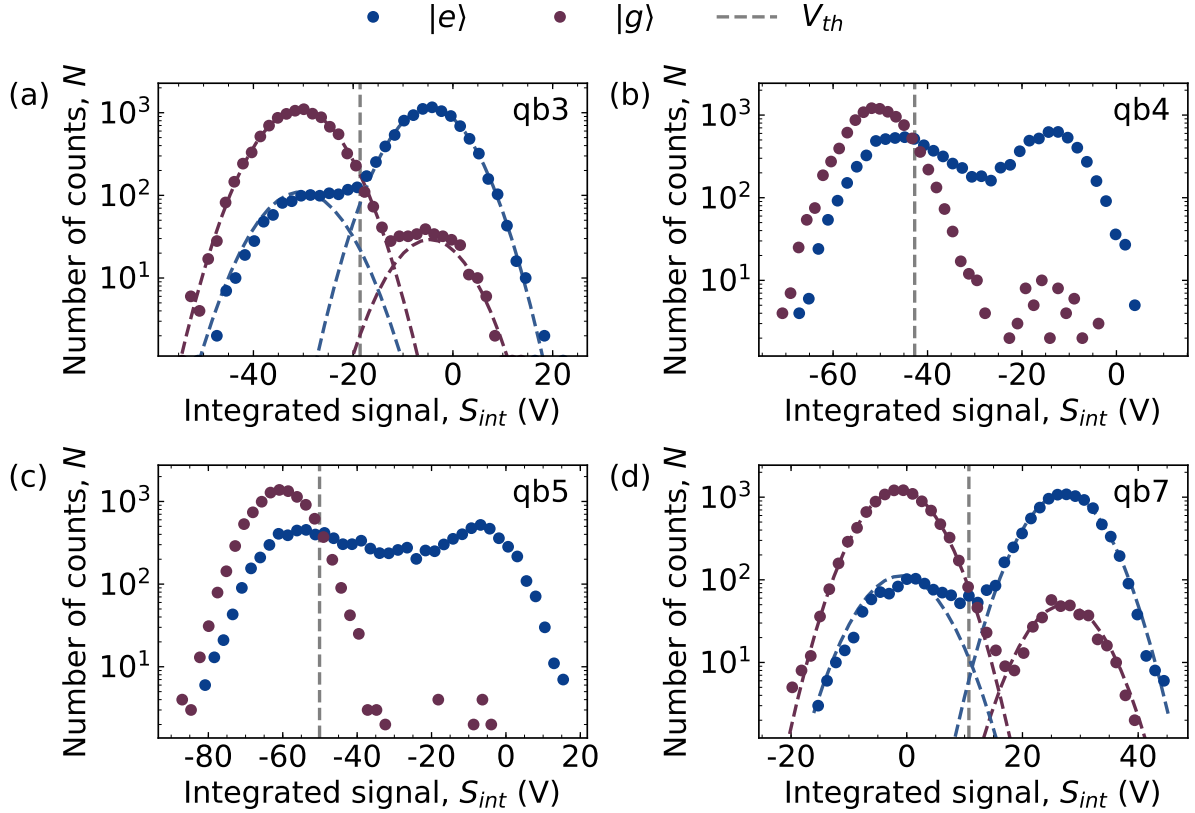


Figure 3.3: Histograms of the shots measured when the qubit was prepared in the ground state (purple) and the excited state (blue) as a function of the integrated readout signal for qubits (a) 3, (b) 4, (c) 5, and (d) 7. The purple and blue dashed lines are fits to double-Gaussians. The gray dashed lines represent the assignment voltage threshold that will be used to discriminate between the qubit in the ground and excited states.

Finally, I will now describe the thresholding and correlator units of the UHFQC, which have been used for the first time in our lab during this project. The voltage thresholds above (below) which each qubit is assigned to be in the excited (ground) state are indicated by the gray dashed vertical lines in Fig. 3.3, and are given by the values $\{-18.6, -42.7, -50.1, 10.7\}$ V for $\{qb3, qb4, qb5, qb7\}$, respectively. These values are obtained by calculating the cumulative sums of the histograms for the qubit prepared in the ground and excited states, and taking the voltage value of the integrated signal which gives the largest difference between these cumulative sums. The thresholding unit of the UHFQC allows to perform the qubit state assignment for each readout channel directly in the detection instrument after the signal was digitally integrated (see Fig. 3.2). Based on the values of the voltage thresholds for each qubit (or each readout channel), the thresholding unit returns the following results for each shot at the voltage value $V_{shot,k}^i$ in each readout channel i :

$$\begin{aligned} 0 & \text{ if } V_{\text{shot},k}^i \leq V_{th}^i, \\ 1 & \text{ if } V_{\text{shot},k}^i > V_{th}^i, \end{aligned}$$

where V_{th}^i is the voltage threshold for readout channel i . Notice that this procedure has the added benefit that it reduces the size of the acquired data from one float (if we use one readout channel) or two floats (for two readout channels) per qubit, to one bit per digital data point per qubit. This reduction is important in achieving faster data processing times inside the UHFQC, as well as in being able to store smaller data sets on the PC and to run faster analysis routines with this data.

The thresholded results can be directly output to the PC, or they can be further processed inside the UHFQC using the correlator unit. This unit measures the $\hat{\sigma}_z \hat{\sigma}_z$ correlations between two qubit states by multiplying the un-thresholded results of any two readout channels. If the results are first thresholded, then the correlator returns the exclusive-not-OR (XNOR) of each pair of data points given by the truth table shown in Table 3.1.

D_k^i	D_k^j	$D_k^i \text{ XNOR } D_k^j$
0	0	1
0	1	0
1	0	0
1	1	1

Table 3.1: Truth table for the exclusive-not-OR (XNOR) operation between two digital bits, D_k^i , D_k^j .

If we recall that 0 corresponds to the ground state and 1 corresponds to the excited state of each qubit, then this truth table describes exactly what we would find if we measured the two-qubit observable

$$\hat{\sigma}_z \hat{\sigma}_z = |00\rangle\langle 00| + |11\rangle\langle 11| - (|01\rangle\langle 01| + |10\rangle\langle 10|), \quad (3.3)$$

which gives +1 if both qubits are in the same state, and -1 if they are in different states. Thus, the correlator unit in the UHFQC calculates the $\hat{\sigma}_z \hat{\sigma}_z$ correlator between two qubits, with the convention that 0 and 1 represent the results when both qubits are in the same states and when they are in different states, respectively.

Even though this feature is very convenient to use in the SRB experiments, it is limited to two qubits; the UHFQC cannot multiply more than two readout channels. Hence, we used both the thresholding and the correlator features for all 6 two-qubit SRB experiments (from all combinations of qubits 3, 4, 5, and 7), while for the experiments on three and four qubits we still used the UHFQC to threshold each shot, but we performed all the $s \leq n$ $\hat{\sigma}_z^{\otimes s}$ correlators in our analysis routines.

3.2 Single qubit virtual Z (VZ) gates

The single qubit Z gate is an important gate in quantum computing, which has been used in many applications including spin model simulations [13], dynamical decoupling

schemes to reduce decoherence [35], and two-qubit gate implementations, such as the controlled-phase (CZ) gate discussed in Sec. 2.2.1, the cross-resonance (CR) gate [4], and the iSWAP gate [44]. A Z gate of angle ϕ can be implemented in several ways. For example, one can apply a flux pulse of duration $\Delta t = \Delta\omega_{\text{qb}}/\phi$ to the qubit, or one can drive the qubit with an off-resonant microwave pulse for a time $\Delta t = \Delta\omega_{\text{qb}}/\phi$, where in both cases $\Delta\omega_{\text{qb}}$ is the detuning of the qubit from its original parking position (see Sec. 2.2.1 and Sec. 2.1.1). In any implementation, the effect of a Z gate is to produce a counterclockwise rotation of the initial qubit state $|\psi_0\rangle$ around the \hat{z} axis of the Bloch sphere by an angle ϕ ; see Fig. 3.4 (a). A virtual Z (VZ) gate is an ideal, zero-duration Z gate that implements the equivalent effect by rotating the $\hat{x} - \hat{y}$ plane of the Bloch sphere *clockwise* around the \hat{z} axis by the same angle ϕ ; see Fig. 3.4 (b). This gate has zero duration because it is completely implemented in software and no physical microwave pulses are sent to the qubit; the VZ gate only changes the reference frame of the qubit state vector [2].

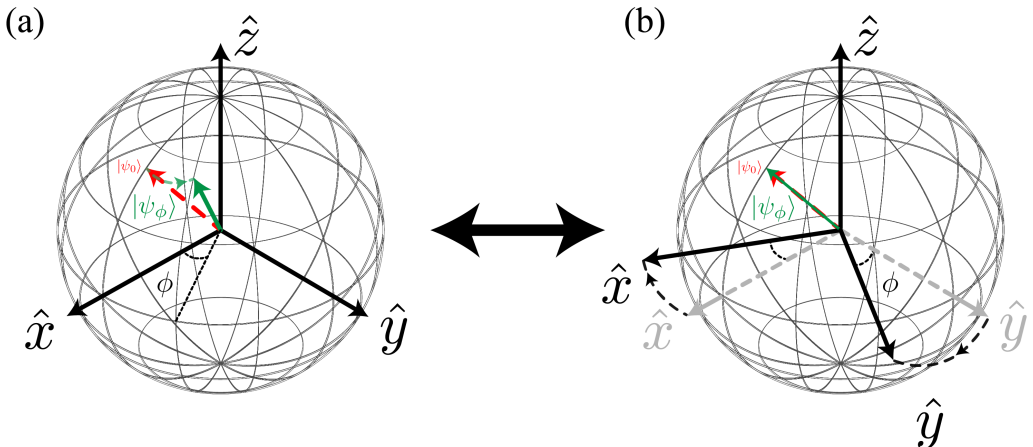


Figure 3.4: Comparison of the effects on the Bloch sphere of a real Z gate of angle ϕ (a) and a virtual Z (VZ) gate of angle ϕ (b). In both cases, the initial state $|\psi_0\rangle$ (red) with xy coordinates $(1, 0)$ is rotated to the final state $|\psi_\phi\rangle$ (green) with xy coordinates $(\cos(\phi), \sin(\phi))$.

In order to understand how the VZ gate is implemented, recall the Hamiltonian for a driven qubit in Eq. (2.6), Sec. 2.1.1. We saw that we can implement rotations about any axis in the $\hat{x} - \hat{y}$ plane by changing the phase of the qubit drive pulse. Thus, the effect of the VZ gate is achieved by subtracting the angle ϕ from the phases of all the subsequent single qubit microwave pulses. This means that all these later pulses will rotate the state about a set of $\hat{x} - \hat{y}$ axes that are rotated clockwise by the angle ϕ with respect to the original axes. The coordinates of the final state vector of the qubit $|\psi_\phi\rangle$ after a sequence containing VZ gates in this new reference frame will be the same as the coordinates of the final state vector after a sequence with real Z gates in the original coordinate system (see Fig. 3.4).

Support for these virtual pulses has been implemented in our main control software framework, PycQED, during this project. For detailed descriptions of the PycQED measurement and analysis framework, see Refs. [29, 32, 45]. Fig. 3.5 shows two basic measurements with VZ gates to demonstrate the correct functionality of this new feature. In Fig. 3.5 (a), we perform four measurements described by the pulse sequences indicated next to the respective data points. Each of these four measurements was repeated $8 \cdot 2^{10}$

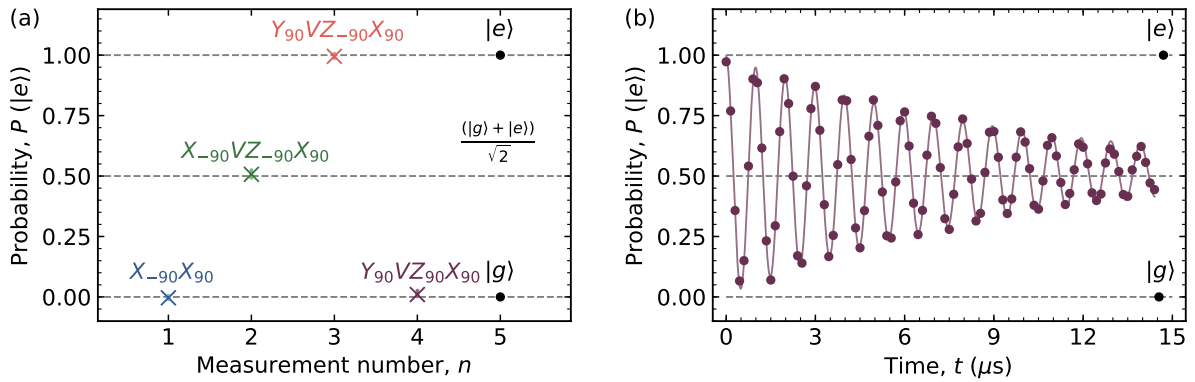


Figure 3.5: Basic measurements with VZ gates. (a) Four measurements with the VZ gate described by the pulse sequences shown next to the data points. The pulse sequences are applied to the qubit from right to left, and each symbol χ_θ denotes a counterclockwise rotation by an angle θ about the $\hat{\chi}$ axis of the Bloch sphere. Each cross marker represents the average over $8 \cdot 2^{10}$ shots of the corresponding measurement, and the small circles around each cross marker are the eight averages over 2^{10} shots. The y -axis shows the probability for the qubit to be in the excited state after each measurement. The black points are calibration states [32], representing the ground and excited states of the qubit. The dashed line at $P(|e\rangle) = 0.5$ denotes the state with equal population in the ground and excited states. (b) A typical Ramsey measurement performed by sweeping the phase of a VZ gate applied between two $\pi/2$ -pulses separated by a varying time delay t shown on the x -axis. The line connecting the data points is a fit to a cosine function with an exponentially decaying envelope. The y -axis shows the probability for the qubit to be in the excited state after each measurement, and the black points and dashed lines represent the same three qubit states as in (a).

times and the average values of these results are shown as crosses. The eight averages of the 2^{10} shots are also plotted as smaller circles, yet they are hardly visible since the standard deviations of the individual results around the mean values are less than 1%. The one exception is the second measurement (green cross at $n = 2$), which has a more visible distribution of points with a standard deviation of $\sim 1\%$. Ideally, each of the pulse sequences indicated in the figure should place the qubit in one of the three qubit states indicated above the gray dashed lines. This is illustrated in Fig. 3.6, which shows the effect on the Bloch sphere of each gate in the pulse sequences that contain a VZ gate (the gates are applied from left to right). The average value of each measurement differs by less than 1% from the theoretically expected value. These results demonstrate both the accuracy of our ability to control and read out the qubits, and the reproducibility of the correct functionality of the VZ gates.

Fig. 3.5 (b) shows a Ramsey measurement with VZ gates on a qubit with transition frequency $f_{qb} \simeq 5.22$ MHz and an averaged dephasing time $T_2^* \simeq 9.3$ μ s. In a typical Ramsey measurement both the time separation between the two $\pi/2$ -pulses and the phase ϕ of the second $\pi/2$ -pulse are varied. The latter changes according to $\phi(t) = t \cdot f_{\text{Ramsey}}$, where $f_{\text{Ramsey}} \simeq 1$ MHz is the frequency of the oscillations in Fig. 3.5 (b). Detailed descriptions of this experiment and how it is performed in our lab can be found in Refs. [29] and [32]. In the Bloch sphere picture, the second Ramsey pulse rotates the qubit state around an axis in the $\hat{x} - \hat{y}$ plane that is rotated counterclockwise around the \hat{z} -axis at each time step. An equivalent effect can be obtained by keeping the phase of the second $\pi/2$ -pulse at zero, and varying instead the angle of a VZ pulse inserted between the two $\pi/2$ -pulses.

Next I will present two examples where the VZ gates are useful in quantum computing algorithms. First I will describe how these gates can be used to compensate dynamic phases in two-qubit controlled-phase gate implementations. Then I will focus on RB and describe how the VZ gates have been used in this project to decompose Clifford gates into single qubit primitive gates.

3.2.1 Dynamic phase correction with VZ gates

As we saw in Sec. 2.2, a fluxing operation on qubit i will cause it to acquire a dynamic phase $\phi_{dyn,i}$, and crosstalk between the flux lines of different qubits will cause the other qubits to also acquire their own dynamic phases. During the implementation of a controlled-phase (CZ) gate it is important that these dynamic phases are removed in order to bring the two qubits into the same reference frame [13, 33, 34]. Traditionally this correction was achieved by designing flux pulse shapes that can be tuned to exactly compensate the dynamic phases for both qubits (see [13, 33]). However, since the CZ gate commutes with the single qubit Z gate, we can achieve the same effect by using VZ pulses to rotate the reference frames of each qubit by their dynamic phases. Specifically, if qubits i and j have dynamic phases $\phi_{dyn,i}$ and $\phi_{dyn,j}$, then we apply the gates $VZ_{-\phi_{dyn,i}}$ and $VZ_{-\phi_{dyn,j}}$ to each qubit before applying the flux pulse that tunes the $|g\rangle \leftrightarrow |e\rangle$ transition of one qubit into resonance with the $|e\rangle \leftrightarrow |f\rangle$ transition of the other qubit.

The pulse sequences for the phase measurement used to measure the dynamic phases of qubit 3 and 4, and to verify the successful correction of these dynamic phases with VZ gates are shown in Fig. 3.7. The dynamic phase is the difference between the phases obtained from cosine fits to the red and blue traces. Thus, we measure $\phi_{dyn,qb3} \simeq 103^\circ \pm$

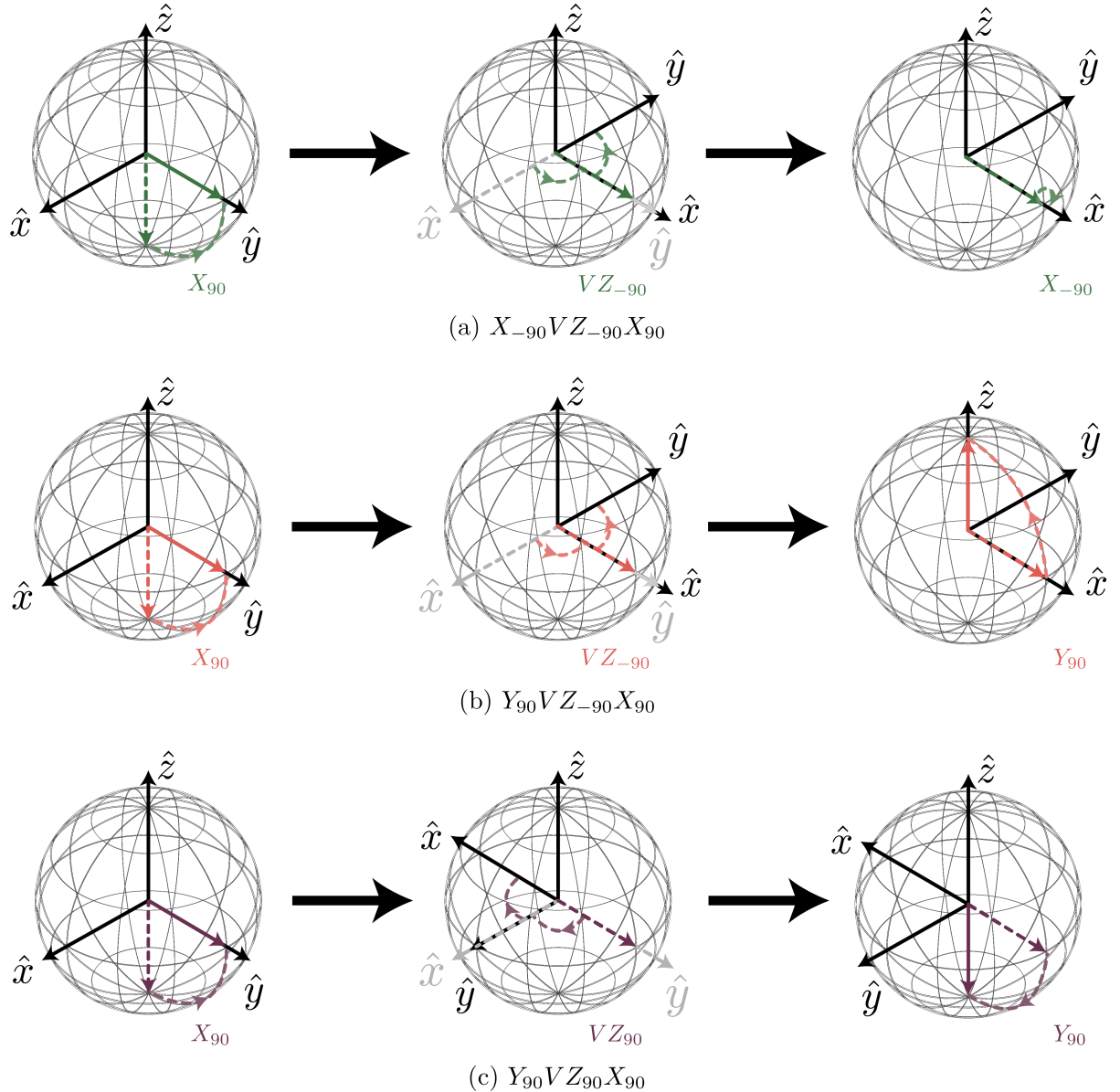


Figure 3.6: Rotations of the qubit state vector on the Bloch sphere induced by the three pulse sequences in Fig. 3.5 that contain a VZ gate: (a) $X_{-90}VZ_{-90}X_{90}$, (b) $Y_{90}VZ_{-90}X_{90}$, (c) $Y_{90}VZ_{90}X_{90}$. Each of these pulse sequences is applied from right to left on the qubit initially in the ground state shown as the dashed arrows along the $-\hat{z}$ axes in each subfigure. The temporal order of the application of each pulse on the Bloch spheres is from left to right, indicated by the black arrows.

0.5° for qubit 3 and $\phi_{dyn,qb4} \simeq -121^\circ \pm 0.4^\circ$ for qubit 4. After applying the VZ pulses to correct these phases, we see that the blue and green traces essentially overlap, with a difference between the phases from the blue and green fits of only $\Delta\phi_{corrected,qb3} \simeq 1.6^\circ \pm 0.4^\circ$ and $\Delta\phi_{corrected,qb4} \simeq 2.2^\circ \pm 0.4^\circ$ for qubits 3 and 4, respectively. Since these values were small enough to allow the implementation of a CZ gate limited by the qubits' coherence times, we can conclude that the dynamic phase correction with VZ gates was successful.

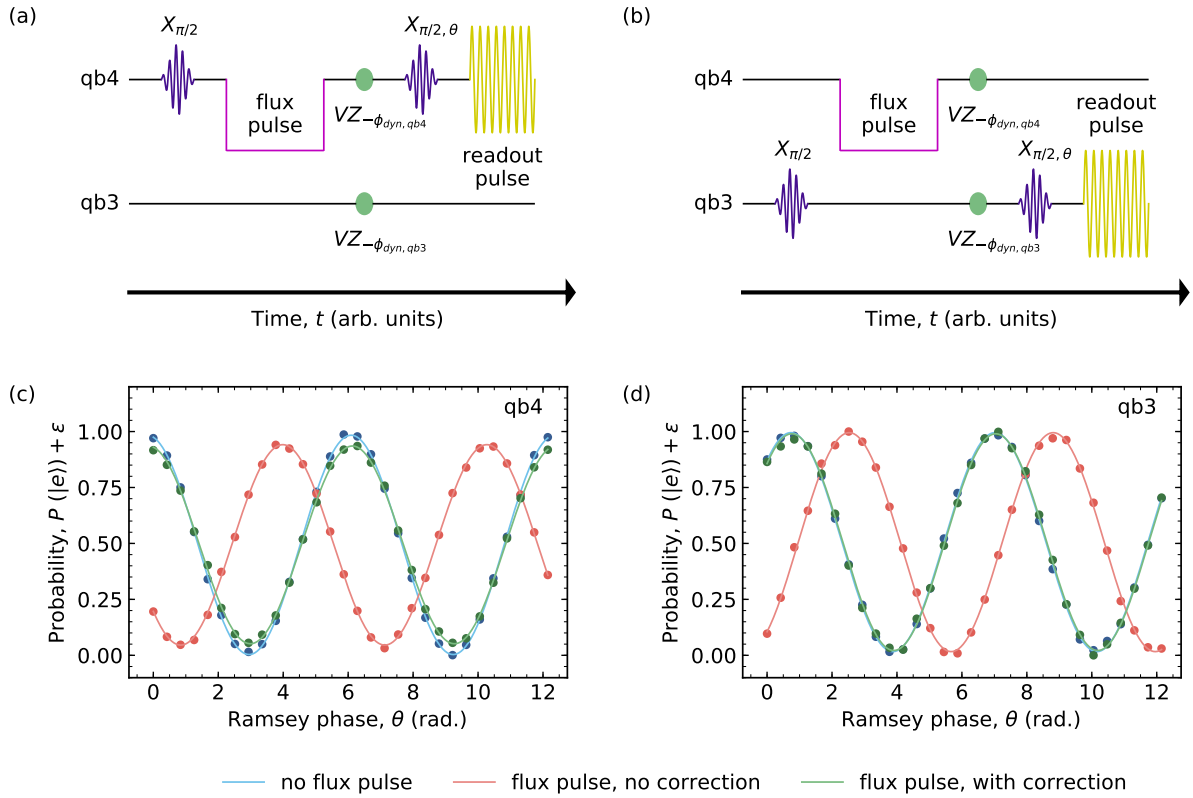


Figure 3.7: Measuring and correcting the dynamic phases acquired by qubits 3 and 4 during a fluxing operation. To measure each qubit's dynamic phase, the pulse sequences in (a) and (b) are used without the VZ gates (green circles). These sequences describe a phase measurement where the flux pulse is always applied on the control qubit (qubit 4) between two $\pi/2$ -pulses on the measured qubit, where the phase θ of the second $\pi/2$ -pulse is varied. The same pulse sequence is used to measure whether the dynamic phase correction was successful by applying the VZ gates with angles $-\phi_{dyn,qb3}$ and $-\phi_{dyn,qb4}$ on the corresponding qubits. (c) and (d) show the results from such measurements on each qubit. The blue data points are obtained from measurements without the flux pulse and no VZ pulses, the red data points are obtained from measurements with the flux pulse but without the VZ corrections, and the green data points are the results after correcting the dynamic phases of both qubits. The y -axes in (c) and (d) show the approximate probability of the respective qubit to be in the excited state, since calibration points were not used to measure this data.

3.2.2 Single qubit RB with VZ gates

In Sec. 2.3 we saw that the implementation of all the RB measurements described in this thesis involves sampling random elements from the single qubit Clifford group, \mathcal{C}_1 . In Sec. 2.1.1, this group was defined to be the normalizer of the single qubit Pauli group, since elements from the latter remain in the Pauli group under the conjugation action of \mathcal{C}_1 . However, in order to sample from the Clifford group, we must first generate all the elements contained in this group, and then express these elements in terms of single qubit gates that we can implement in the lab. In this section we will first identify the elements in \mathcal{C}_1 , and then we will compare two possible decompositions of these elements into primitive single qubit gates.

The single qubit Clifford group has 24 elements that are given by all the possible combinations of the elements from the following three groups [19]:

The Pauli group $\mathcal{P} = \{\mathbf{I}, \mathbf{X}, \mathbf{Y}, \mathbf{Z}\}$, where $\mathbf{X}, \mathbf{Y}, \mathbf{Z}$ are quantum maps that describe 180° rotations about the $\hat{x}, \hat{y}, \hat{z}$ axes of the Bloch sphere.

The exchange group $\mathcal{S} = \{\mathbf{I}, \mathbf{S}, \mathbf{S}^2\}$, where \mathbf{S}, \mathbf{S}^2 are quantum maps that describe the exchange operations $(x, y, z) \xrightarrow{S} (z, x, y) \xrightarrow{S^2} (y, z, x)$, where x, y, z are the coordinates of the qubit state vector on the Bloch sphere.

The Hadamard group $\mathcal{H} = \{\mathbf{I}, \mathbf{H}\}$, where \mathbf{H} is the quantum map describing the action $(x, y, z) \xrightarrow{H} (z, -y, x)$ on the coordinates of the quantum state vector.

In all the groups above, \mathbf{I} is the identity map. All the 24 elements of the Clifford group are shown in the first column of Table 3.2. The last two columns show two possible decompositions of each Clifford element into primitive single qubit gates. The standard implementation is to use the $XY_{\frac{\pi}{2}}$ decomposition consisting of only the gates X_π , Y_π , $X_{\pm\frac{\pi}{2}}$, and $Y_{\pm\frac{\pi}{2}}$, i.e. 180° and $\pm 90^\circ$ rotations about the \hat{x} and \hat{y} axes of the Bloch sphere [19]. The $XY_{\frac{\pi}{2}}$ decomposition has on average 1.825 primitive physical gates per Clifford element.

The HZ decomposition consists of only the gates X_π , Z_π , $X_{\pm\frac{\pi}{2}}$, and $Z_{\pm\frac{\pi}{2}}$. The set of pulses for this decomposition shown in the last column in Table 3.2 were obtained from the corresponding pulses in the $XY_{\frac{\pi}{2}}$ decomposition by using the fact that any element in the unitary group of degree 2 with determinant 1 (called the *special unitary group* and denoted by $SU(2)$) can be written as [2]

$$U(\theta, \phi, \lambda) = \begin{pmatrix} \cos(\theta/2) & -ie^{i\lambda}\sin(\theta/2) \\ -ie^{i\phi}\sin(\theta/2) & e^{i(\lambda+\phi)}\cos(\theta/2) \end{pmatrix} = Z_\phi \cdot X_\theta \cdot Z_\lambda. \quad (3.4)$$

Using this equation we can rewrite all the primitive gates in the $XY_{\frac{\pi}{2}}$ decomposition in terms of only X and Z gates. If we use VZ gates instead of the real Z gates, then this decomposition becomes advantageous because it has on average only 1.125 primitive *physical* gates per Clifford element. Since the fidelity of our multi-qubit algorithms is often limited by the qubit lifetimes, a zero-duration gate that produces shorter algorithms is a very useful tool in quantum computing.

We verify experimentally that we can measure the reduction in the average error per Clifford as a result of using the HVZ decomposition with fewer average physical gates per Clifford element. Fig. 3.8 shows the exponential decays of the measured expectation values $\langle \hat{\sigma}_z \rangle$ as a function of the Clifford sequence length m from standard single qubit RB measurements on qubits 3, 4, 5, and 7. The dark and light colors represent measurements using the HVZ and $XY_{\frac{\pi}{2}}$ decompositions, respectively. Table 3.3 summarizes

Clifford element	$XY_{\frac{\pi}{2}}$ decomposition	$H(V)Z$ decomposition
$\mathbb{1} - \mathbb{1} - \mathbb{1}$	$\mathbb{1}$	$\mathbb{1}$
$\mathbb{1} - \mathbb{1} - S$	$Y_{\pi/2} - X_{\pi/2}$	$X_{\pi/2} - VZ_{\pi/2}$
$\mathbb{1} - \mathbb{1} - S^2$	$X_{-\pi/2} - Y_{-\pi/2}$	$VZ_{-\pi/2} - X_{-\pi/2}$
$X - \mathbb{1} - \mathbb{1}$	X_π	X_π
$X - \mathbb{1} - S$	$Y_{-\pi/2} - X_{-\pi/2}$	$VZ_{-\pi/2} - X_{-\pi/2} - VZ_{\pi/2} - X_{-\pi/2}$
$X - \mathbb{1} - S^2$	$X_{\pi/2} - Y_{-\pi/2}$	$VZ_{-\pi/2} - X_{-\pi/2} - VZ_\pi$
$Y - \mathbb{1} - \mathbb{1}$	Y_π	$VZ_{-\pi/2} - X_\pi - VZ_{\pi/2}$
$Y - \mathbb{1} - S$	$Y_{-\pi/2} - X_{\pi/2}$	$VZ_{-\pi/2} - X_{-\pi/2} - VZ_{\pi/2} - X_{\pi/2}$
$Y - \mathbb{1} - S^2$	$X_{\pi/2} - Y_{\pi/2}$	$X_{\pi/2} - VZ_{-\pi/2} - X_{\pi/2} - VZ_{\pi/2}$
$Z - \mathbb{1} - \mathbb{1}$	$X_\pi - Y_\pi$	VZ_π
$Z - \mathbb{1} - S$	$Y_{\pi/2} - X_{-\pi/2}$	$VZ_\pi - X_{\pi/2} - VZ_{\pi/2}$
$Z - \mathbb{1} - S^2$	$X_{-\pi/2} - Y_{\pi/2}$	$VZ_{\pi/2} - X_{-\pi/2}$
$\mathbb{1} - H - \mathbb{1}$	$Y_{\pi/2} - X_\pi$	$VZ_{\pi/2} - X_{\pi/2} - VZ_{\pi/2}$
$\mathbb{1} - H - S$	$X_{-\pi/2}$	$X_{-\pi/2}$
$\mathbb{1} - H - S^2$	$X_{\pi/2} - Y_{-\pi/2} - X_{-\pi/2}$	$VZ_{\pi/2}$
$X - H - \mathbb{1}$	$Y_{-\pi/2}$	$VZ_{-\pi/2} - X_{-\pi/2} - VZ_{\pi/2}$
$X - H - S$	$X_{\pi/2}$	$X_{\pi/2}$
$X - H - S^2$	$X_{\pi/2} - Y_{\pi/2} - X_{\pi/2}$	$X_\pi - VZ_{\pi/2}$
$Y - H - \mathbb{1}$	$Y_{-\pi/2} - X_\pi$	$VZ_{-\pi/2} - X_{-\pi/2} - VZ_{\pi/2} - X_\pi$
$Y - H - S$	$X_{\pi/2} - Y_\pi$	$X_{\pi/2} - VZ_{-\pi/2} - X_\pi - VZ_{\pi/2}$
$Y - H - S^2$	$X_{\pi/2} - Y_{-\pi/2} - X_{\pi/2}$	$X_{-\pi/2} - VZ_\pi - X_{\pi/2} - VZ_{\pi/2}$
$Z - H - \mathbb{1}$	$Y_{\pi/2}$	$VZ_{-\pi/2} - X_{\pi/2} - VZ_{\pi/2}$
$Z - H - S$	$X_{-\pi/2} - Y_\pi$	$X_{-\pi/2} - VZ_{-\pi/2} - X_\pi - VZ_{\pi/2}$
$Z - H - S^2$	$X_{\pi/2} - Y_{\pi/2} - X_{-\pi/2}$	$VZ_{-\pi/2}$

Table 3.2: The 24 elements in the single-qubit Clifford group (first column) and the two possible decompositions of these elements into primitive single qubit gates. The standard $XY_{\frac{\pi}{2}}$ decomposition (second column) consists of 180° and $\pm 90^\circ$ rotations about the \hat{x} and \hat{y} axes of the Bloch sphere denoted by X_π , Y_π , $X_{\pm\frac{\pi}{2}}$, and $Y_{\pm\frac{\pi}{2}}$. The HVZ decomposition (last column) contains only the gates X_π , VZ_π , $X_{\pm\frac{\pi}{2}}$, and $VZ_{\pm\frac{\pi}{2}}$.

the average errors per Clifford (EPCs) r_1 calculated with Eq. (2.30) for each qubit for each decomposition. As expected, the EPCs from measurements using the HVZ decomposition are consistently smaller than the ones from RB with the $XY_{\frac{\pi}{2}}$ decomposition. However, within the empirical error bars, qubits 4 and 7 might have a larger EPC from using HVZ than from using $XY_{\frac{\pi}{2}}$. Notice also that the empirical error bars for qubits 5 and 7 are larger than those for the other two qubits. The error bars for these qubits are large most likely due to an instability in their frequencies and dephasing times, which we observed in the Ramsey and Echo calibration measurements [23, 32]. The sweet spot frequencies of the qubits at approximately $\{6.20, 6.26, 6.10, 6.12\}$ GHz for $\{\text{qb3}, \text{qb4}, \text{qb5}, \text{qb7}\}$ were very close to each other, and the mixers used for upconverting the qubit drive signals were not calibrated for these measurements. Hence, mixer imperfections [23, 42] could have caused the qubits to be driven by spurious frequency components, which may have lead to the instabilities and the large experimental uncertainties that we observed.

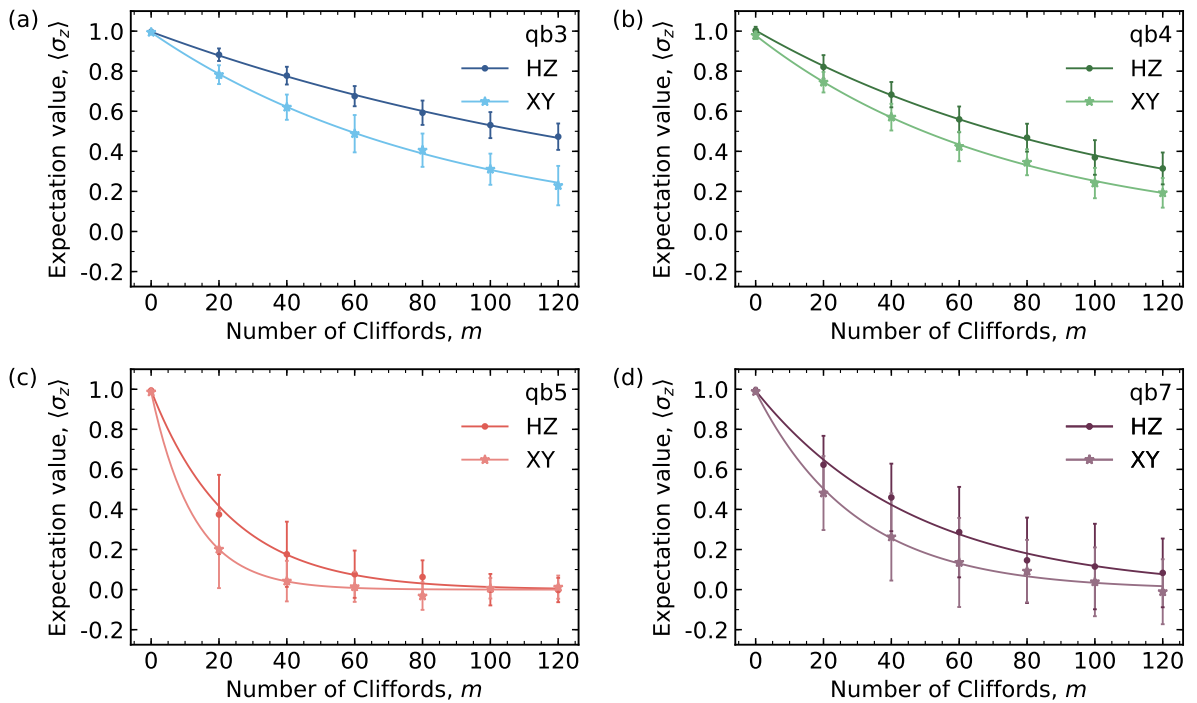


Figure 3.8: Comparison between using the HVZ decomposition (dark-colored circles) and the $XY_{\frac{\pi}{2}}$ decomposition (light-colored stars) in single qubit RB experiments on qubits (a) 3, (b) 4, (c) 5, and (d) 7. The traces from the measurements using the $XY_{\frac{\pi}{2}}$ decomposition decay faster than the ones performed using the HVZ decomposition, indicating a larger error per Clifford when using $XY_{\frac{\pi}{2}}$. The lines connecting the data points are fits to Eq. (2.28), and the error bars represent the 68% confidence intervals calculated from the empirical standard deviations of the distributions of $K = 100$ different Clifford sequences for each sequence length m .

Qubit	$r_{1,HVZ}$ (%)	$r_{coh_lim,HVZ}$ (%)	$r_{1,XY\frac{\pi}{2}}$ (%)	$r_{coh_lim,XY\frac{\pi}{2}}$ (%)
Qb3	0.31 ± 0.2 (0.1)	0.24	0.58 ± 0.3 (0.1)	0.41
Qb4	0.48 ± 0.3 (0.1)	0.33	0.67 ± 0.2 (0.1)	0.55
Qb5	2.13 ± 0.6 (0.3)	0.77	3.83 ± 1.3 (0.6)	1.28
Qb7	1.05 ± 0.8 (0.2)	0.27	1.66 ± 1.0 (0.3)	0.45

Table 3.3: Comparison between the average errors per Clifford (EPCs) from RB with the HVZ and $XY\frac{\pi}{2}$ decompositions. The EPCs from RB measurements using the HVZ decomposition are consistently smaller than the ones from measurements using the $XY\frac{\pi}{2}$ decomposition. The coherence limited EPC, r_{coh_lim} , is discussed in the main text. The larger values for the uncertainties around the main quantities were obtained from the empirical standard deviations, while the smaller values in parentheses quantify the uncertainty due to finite sampling of the single qubit Clifford group.

The empirical uncertainty values were obtained by performing a weighted least squares fit with weights given by the standard deviations of the distributions of K different Clifford sequences for each sequence length m (see Sec. 2.3.2). In each of the RB experiments shown in Fig. 3.8 we used $K = 100$ different randomly generated sequences of length m , for each $m \in [0, 20, 40, 60, 80, 100, 120]$. Therefore, these numbers quantify the uncertainty due to sampling the Clifford group only $K = 100$ times, as well as the experimental uncertainty in the expectation values $\langle \hat{\sigma}_z \rangle$ due to an insufficient number of averaged repetitions, N , of each identical sequence, m_i for $i \leq K$. We used $N = 2^{12}$ for all measurements in Fig. 3.8.

The additional uncertainty values shown in parentheses next to each EPC in Table 3.3 were obtained by implementing the theory introduced by Helsen et al. in Ref.[39], which estimates the confidence intervals around the measured quantities due to insufficient sampling of the single qubit Clifford group \mathcal{C}_1 . The RB theory in Sec. 2.3 was derived under the assumption that we fully sample the 24-element group \mathcal{C}_1 for each m . However, in order to achieve this, we would need a total of $K = m^{24}$ repetitions for each m , which is experimentally impossible. Nevertheless, Helsen et al. have shown that the uncertainties around the quantities of interest have upper bounds that at worst scale only linearly with m for shorter and intermediate sequence lengths, and that are independent of m for large sequence lengths. The latter are defined as $mr_{1,0} \simeq 1$, where $r_{1,0}$ is a previous estimate of the EPC. Specifically, the variance of the distribution of K averaged single qubit RB results has the following upper bounds[39]:

$$\begin{aligned} V(m) &\leq \frac{13}{2}mr_{1,0}^2, \quad mr_{1,0} < 1 \\ V(m) &\leq \frac{7}{2}r_{1,0}, \quad \text{and } mr_{1,0} \simeq 1 \text{ and } mr_{1,0} > 1. \end{aligned} \tag{3.5}$$

These bounds give an exponential reduction in the values for K required to obtain rigorous confidence intervals compared to previous estimates [46]. The uncertainty values shown in parentheses in Table 3.3 were obtained from a weighted least squares fit with the weights given by the $\delta = 68\%$ confidence intervals ϵ_m around the values $\langle \hat{\sigma}_z \rangle_m$ obtained from averaging over all K sequences at each sequence length m . The values for ϵ_m are obtained

from the variance V by solving the following non-linear equation for each m [39]

$$H(V, \epsilon_m) = \left(\frac{\delta}{2}\right)^{\frac{1}{K}}, \quad (3.6)$$

where

$$H(V, \epsilon_m) = \left(\frac{1}{1 - \epsilon_m}\right)^{\frac{1-\epsilon_m}{V+1}} \left(\frac{V}{V + \epsilon_m}\right)^{\frac{V+\epsilon_m}{V+1}}, \quad (3.7)$$

and $V = V(m)$ is given by Eq. (3.5). Notice in Table 3.3 that the uncertainties due to insufficient sampling of \mathcal{C}_1 account for around 50% of the values estimated from the empirical standard deviations. These results suggest that our single qubit RB experiments are limited by both the experimental uncertainty between runs, and by insufficient sampling of \mathcal{C}_1 .

Finally, the coherence limited infidelity, $r_{\text{coh_lim}}$, is the lowest value of the EPC that can be achieved with RB given a qubit's energy relaxation time T_1 and its dephasing time T_2 . This lower bound depends on the decomposition used in the experiment and is calculated from [20]:

$$r_{\text{coh_lim}} = 1 - \left[\frac{1}{6} \left(3 + 2e^{-\frac{\tau_p}{T_2}} + e^{-\frac{\tau_p}{T_1}} \right) \right]^{\langle N_{\text{GPC}} \rangle}, \quad (3.8)$$

where τ_p is the duration of a single physical gate, and $\langle N_{\text{GPC}} \rangle$ is the average number of physical gates per Clifford element given by the decomposition used.

3.2.3 Single qubit IRB with VZ gates

In order to further confirm that our VZ gates work as expected, we performed IRB with the HVZ decomposition using as interleaved gates the VZ gate of angle 180° , denoted by VZ_{180} , X gates of angles 180° and 90° denoted by X_{180} , and X_{90} , respectively, and an identity gate denoted by I . The latter is just a spacer pulse of the same duration as the X gates. The results from standard RB (no interleaved gate) and IRB with VZ_{180} and X_{180} on qubits 3, 4, 5, and 7 are shown in Fig. 3.9. The average infidelities r_1 calculated using Eq. (2.30), are shown in Table 3.4, where the corresponding measurements are indicated by the subscripts in the top row. Table 3.5 shows the gate errors r_{gate} calculated using Eq. (2.31), for each of the interleaved gates mentioned above.

Qubit	$r_{1,\text{noGate}} (\%)$	$r_{1,\text{Z}_{180}} (\%)$	$r_{1,I} (\%)$	$r_{1,X_{90}} (\%)$	$r_{1,X_{180}} (\%)$	$r_{\text{coh_lim}} (\%)$
Qb3	0.37 ± 0.2	0.29 ± 0.2	0.61 ± 0.1	0.65 ± 0.1	0.73 ± 0.2	0.26
Qb4	0.51 ± 0.2	0.48 ± 0.2	0.81 ± 0.2	0.84 ± 0.2	1.14 ± 0.2	0.36
Qb5	2.10 ± 0.3	1.74 ± 0.3	2.79 ± 0.4	3.16 ± 0.4	3.50 ± 0.4	1.52
Qb7	0.45 ± 0.2	0.42 ± 0.2	0.51 ± 0.1	0.67 ± 0.1	0.68 ± 0.1	0.27

Table 3.4: Average infidelities from the (I)RB measurements indicated by the subscripts in the top row performed on qubits 3, 4, 5 and 7. The last column shows the coherence limited errors per Clifford calculated as explained in the previous section. The errors are estimated from the statistical standard deviations of the distributions of $K = 100$ different Clifford sequences for each sequence length m .

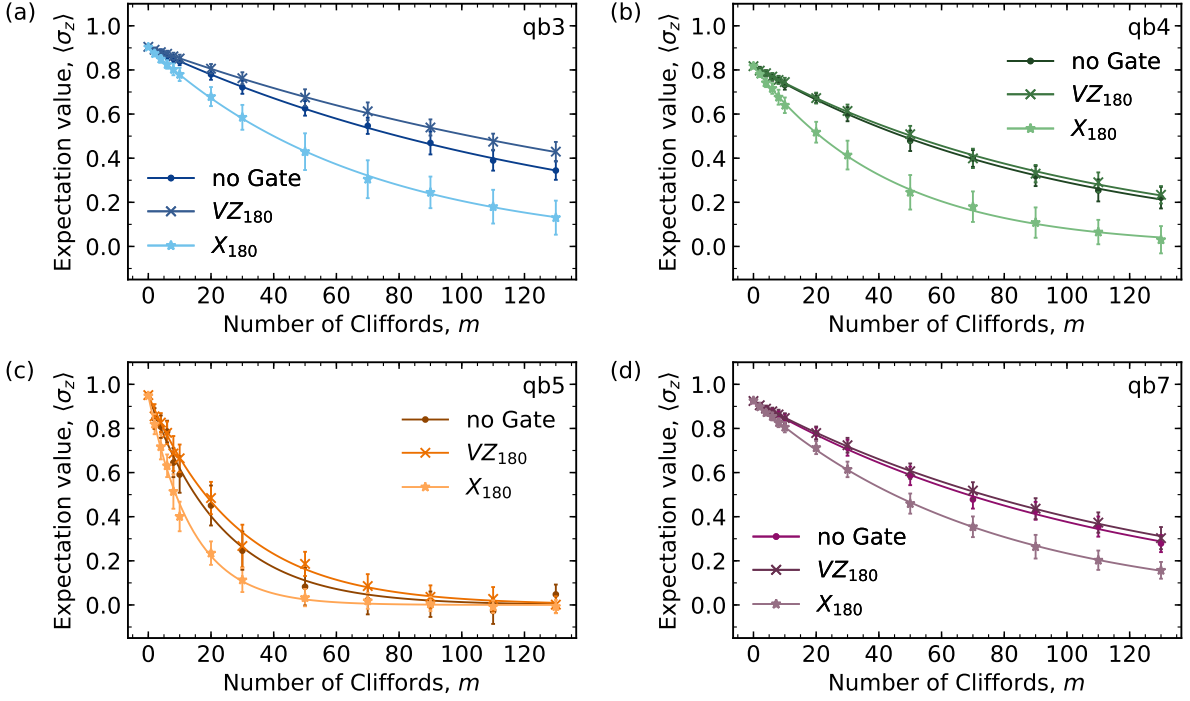


Figure 3.9: Expectation value of the observable $\hat{\sigma}_z$ as a function of the Clifford sequence length, m , from standard RB measurements (indicated in the legend by 'no Gate'), and IRB measurements using VZ_{180} and X_{180} as interleaved gates. All three measurements are performed on each of the qubits indicated in the top right corner: (a) qubit 3, (b) qubit 4, (c) qubit 5, (d) qubit 7. For each trace in each figure the error bars represent the 68% confidence intervals obtained from the empirical standard deviations of the distributions of $K = 100$ different Clifford sequences for each sequence length m .

Qubit	$r_{Z_{180}} (\%)$	$r_I (\%)$	$r_{X_{90}} (\%)$	$r_{X_{180}} (\%)$
Qb3	-0.08 ± 0.2	0.24 ± 0.2	0.28 ± 0.2	0.37 ± 0.2
Qb4	-0.03 ± 0.3	0.30 ± 0.3	0.33 ± 0.3	0.63 ± 0.3
Qb5	-0.38 ± 0.4	0.72 ± 0.5	1.10 ± 0.5	1.46 ± 0.5
Qb7	-0.03 ± 0.2	0.07 ± 0.2	0.23 ± 0.2	0.24 ± 0.2

Table 3.5: Average errors for the indicated gates obtained from IRB measurements on qubits 3, 4, 5 and 7. The errors are estimated from the statistical standard deviations of the distributions of $K = 100$ different Clifford sequences for each sequence length m .

Each data point in Fig. 3.9 was obtained by using $K = 100$ different randomly sampled Clifford sequences of length m , and $N = 2^{12}$ repetitions of each sequence m_i for $i \leq K$.

Since the VZ gate is a zero-duration, ideal gate, we expect its error to be approximately zero. From the first column in Table 3.5 we see that this is indeed what we measure for qubits 3, 4, and 7. For qubit 5, we measure a relatively large gate error of around $0.38 \pm 0.4\%$; however, within the error bars, the error for VZ_{180} for qubit 5 is also approximately zero. The gate errors for VZ_{180} are negative because the average infidelities from IRB with these virtual gates were smaller by about 0.1% for qubits 3, 4, 7 and by about 0.3% for qubit 5 than the average infidelities from standard RB (no gate interleaved); see Table 3.4. This result can also be seen in Fig. 3.9, where the standard RB measurements (denoted by 'no Gate' in the legend) always show a slightly stronger exponential decay. This systematic behavior has not been further investigated in this thesis. One possible explanation is that interleaving VZ_{180} gates after each Clifford element corrects some of the coherent errors that might otherwise occur in a standard RB experiment.

The identity gate I is essentially a waiting time of the same duration as an X gate, which was 25 ns long for all our measurements. Therefore we expect that $r_{X_{90}} \approx r_I + \epsilon$, where ϵ indicates that the error of X_{90} is typically slightly larger due to coherent errors such as over- or under-rotations of the qubit state vector. We also expect $r_{X_{180}} \approx r_I + 2\epsilon$, since the X_{180} gate is about twice as likely to be affected by coherent errors. The X_{180} pulse is also more strongly affected by leakage outside the computational subspace, since it has around twice the amplitude of the X_{90} pulse.

Indeed, we see in Table 3.5 that for qubits 3 and 4 the gate errors of the I and X_{90} gates differ by less than 0.1%, while the errors of X_{180} are around twice as large. For qubit 5, the error of X_{180} is also around twice that of X_{90} , yet the error of the I gate is around 0.4% smaller than that of the X_{90} gate. For qubit 7, X_{180} and X_{90} have around the same error, while the error of the I gate is significantly smaller than the error of X_{90} by around 0.15%. These results indicate that qubits 5 and 7 were affected by larger amounts of coherent errors than qubits 3 and 4.

4 Characterizing the amount of cross-talk and correlated errors in multi-qubit algorithms with SRB

In this section I will present and discuss the results from performing single qubit randomized benchmarking (RB) and simultaneous RB (SRB) on all combinations of $n \leq 4$ qubits using qubits 3, 4, 5, and 7. Thus we performed 4 standard single qubit RB experiments ($n = 1$), 6 two-qubit SRB experiments ($n = 2$), 4 three-qubit SRB experiments ($n = 3$), and one four-qubit SRB experiment ($n = 4$). From measurements of the $\hat{\sigma}_{z,i}$ operators for each qubit i in all these (S)RB experiments, we use Eq. (2.51) to calculate the average single qubit error per Clifford (EPC) $r_{1,i}^{(n)}$ as a function of n , the number of simultaneously operated qubits. We use the increase in $r_{1,i}^{(n)}$ with n as a quantitative measure of the amount of crosstalk in our multi-qubit algorithms.

In addition to measuring all single qubit observables, we also measure all combinations of $\hat{\sigma}_z^{\otimes s}$ correlators on $s \in [2, n]$ qubits in each of the 11 SRB experiments. Doing this allows us to use Eqs. (2.47) and (2.50) to estimate the total depolarizing parameters $\bar{\alpha}_n$ associated with the depolarizing channels $\Lambda_{\mathcal{C}_1^{\otimes n}}$ (Eq. (2.37)) corresponding to the average multi-qubit error channels $\bar{\mathcal{E}}_{\otimes n}$ implemented by each n -qubit (S)RB protocol. From $\bar{\alpha}_n$ we calculate the multi-qubit errors r_n associated with each channel $\bar{\mathcal{E}}_{\otimes n}$. We then use the formalism developed in Sec. 2.3.5 to quantify the amount of correlated errors in our n -qubit algorithms, and to investigate the degree of these correlated errors.

Lastly, I will briefly discuss how crosstalk from multiplexed readout would affect the SRB results. I will show that this effect was negligibly small in our experiments, and that it most likely does not contribute to the behaviors we observe.

For all the (S)RB measurements discussed in this section, we generated $K = 100$ different Clifford sequences for each sequence length m , and we used $N = 2^{12}$ identical repetitions of each K sequence of length m to obtain the expectation values of the single qubit observables $\hat{\sigma}_z$, and of all the correlators $\hat{\sigma}_z^{\otimes s}$, for $s \leq n$. See Sec. 2.3 for details about how the single qubit RB and multi-qubit SRB experiments are implemented in the lab.

4.1 Crosstalk in multi-qubit algorithms

From SRB experiments on up to four qubits using qubits 3, 4, 5, and 7, we calculate the increase of the average single qubit EPCs, $r_{1,i}^{(n)}$, with the number of simultaneously operated qubits n , for each qubit i . This increase is seen qualitatively in Fig. 4.1 by the faster decay of the expectation value of each single qubit observable $\hat{\sigma}_{z,i}$ when all four qubits are operated in the 4-qubit SRB experiment (light colors, $n = 4$) compared to when only each qubit is operated alone in standard, single qubit RB (dark colors, $n = 1$).

Quantitatively, we see in Table 4.1 that the EPCs are about 1% to 2% larger when $n = 4$ (second to last column) compared to the values when $n = 1$ (second column). The number of qubits operated simultaneously, n , is indicated in the superscripts in the top row. The last row shows the average of all the EPC values in each column, i.e. the average single qubit EPC from all four qubits when we simultaneously operate n qubits. We denote this quantity by $\bar{r}_1^{(n)}$ for each n . Due to crosstalk, we obtain an average single qubit EPC of $\bar{r}_1^{(4)} \simeq 2.18 \pm 0.2\%$ when we operate all four qubits simultaneously, which is about 2.5 times larger than the average EPC of approximately $\bar{r}_1^{(1)} \simeq 0.86 \pm 0.1\%$ when

we operate only one qubit at a time:

$$\bar{r}_1^{(4)} \simeq 2.5\bar{r}_1^{(1)}. \quad (4.1)$$

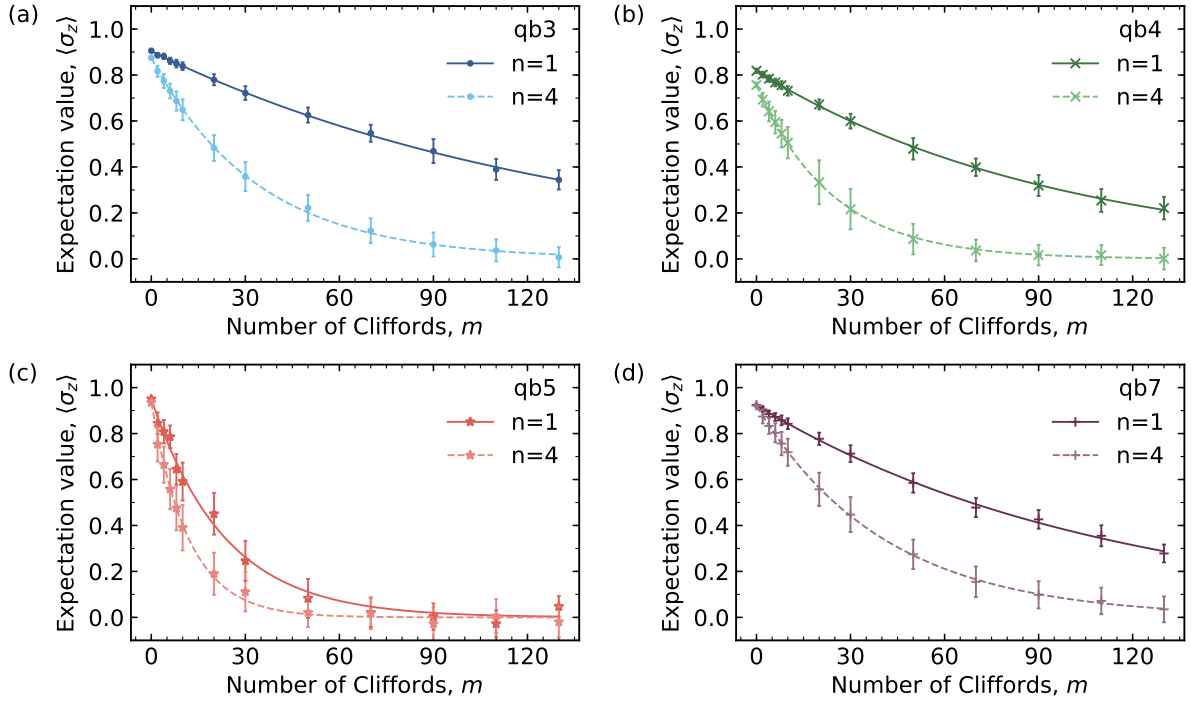


Figure 4.1: Crosstalk in multi-qubit SRB experiments. Each figure shows the exponential decay of the expectation value of the single qubit operator $\hat{\sigma}_z$ as a function of the Clifford sequence length m for the qubit indicated in the top right corner. The darker traces were obtained from standard RB ($n = 1$), where only the respective qubit is operated, while the lighter traces correspond to 4-qubit SRB measurements ($n = 4$), where all four qubits are operated simultaneously. The lines are fits to the exponential decay in Eq. (2.28). The error bars represent the 68% confidence intervals obtained from the empirical standard deviations of the distributions of $K = 100$ different Clifford sequences for each sequence length m .

This 2.5-fold increase in the average single qubit EPC can also be seen in Fig. 4.2. This figure shows all the EPCs listed in Table 4.1 for each qubit, with qubits 3, 4, 5, and 7 denoted by the blue circles, the green crosses, the red stars, and the purple pluses, respectively. Since we performed each n -qubit (S)RB experiment on all possible combinations of n qubits from the set of qubits $\{3, 4, 5, 7\}$, we obtain several EPC values for one qubit when $n = 2$ and $n = 3$. The numbers in bold shown in the third and fourth columns of Table 4.1 indicate the indices of the qubits in the SRB experiments from which the corresponding EPC values were obtained for the respective qubit indicated in the first column. The magenta line in Fig. 4.2 shows the average single qubit EPC, $\bar{r}_1^{(n)}$, as a function of the number of qubits operated simultaneously, n . Due to crosstalk, $\bar{r}_1^{(n)}$ increases almost linearly with n , with around an 0.5% increase for each added qubit.

We have also investigated whether we find the same amount of crosstalk from AC-Stark shift measurements on pairs of qubits (see Sec. 2.2.1). We measure an approximate AC-Stark shift between qubits 3 and 5 of around 40 kHz. Since all four qubits are parked

	$r_1^{(1)}$ (%)	$r_1^{(2)}$ (%)	$r_1^{(3)}$ (%)	$r_1^{(4)}$ (%)	r_{coh_lim} (%)
Qb3	0.37 ± 0.16 (0.09)	34: 0.89 ± 0.15 (0.10)	345: 1.30 ± 0.16 (0.13)	1.45 ± 0.18 (0.14)	0.26
		35: 0.71 ± 0.16 (0.09)	347: 1.07 ± 0.16 (0.11)		
		37: 0.62 ± 0.16 (0.09)	357: 0.84 ± 0.17 (0.10)		
Qb4	0.51 ± 0.21 (0.13)	34: 0.89 ± 0.19 (0.14)	345: 1.79 ± 0.32 (0.25)	2.03 ± 0.39 (0.28)	0.35
		45: 1.10 ± 0.21 (0.17)	347: 1.13 ± 0.20 (0.16)		
		47: 0.83 ± 0.20 (0.14)	457: 1.48 ± 0.26 (0.21)		
Qb5	2.10 ± 0.34 (0.23)	35: 2.28 ± 0.35 (0.26)	345: 3.63 ± 0.50 (0.41)	4.04 ± 0.62 (0.47)	1.38
		45: 2.39 ± 0.31 (0.23)	357: 3.57 ± 0.60 (0.45)		
		57: 2.33 ± 0.37 (0.26)	457: 3.44 ± 0.49 (0.37)		
Qb7	0.45 ± 0.16 (0.09)	37: 0.79 ± 0.19 (0.09)	347: 1.08 ± 0.20 (0.11)	1.21 ± 0.21 (0.12)	0.28
\bar{r}_1	0.86 ± 0.11 (0.07)	1.21 ± 0.07 (0.05)	1.79 ± 0.09 (0.07)	2.18 ± 0.20 (0.14)	0.57

Table 4.1: Single qubit EPCs from measuring the single qubit observables $\hat{\sigma}_z$ for each qubit indicated in the first column, in all (S)RB experiments that contain that qubit. The number of qubits in each experiment, n , is indicated in the superscripts in the top row. The numbers in bold for $n = 2$ and $n = 3$ are the indices of the qubits in the SRB experiment from which we obtained the corresponding EPC for the qubit indicated in the first column. The last row shows the average of all the EPCs in the respective column (magenta points in Fig. 4.2). The last column shows the coherence limited EPCs. Both sets of error bars represent the 68% confidence intervals; the first set is obtained from the empirical standard deviations of the distributions of $K = 100$ different Clifford sequences for each sequence length m , while the errors in parentheses are upper bounds on the uncertainty due to finite sampling of the single qubit Clifford group.

at their sweet spots where they are all within around 100 MHz of each other (see Sec. 3.1), we expect the AC-Stark shift on other pairs of qubits to be around the same value. If we compare this value to the average Clifford gate time of 28.125 ns, we would expect this AC-Stark shift to induce an average error per Clifford of around 0.7%. This value is slightly larger than the increase in the average single qubit EPC with each qubit added in the algorithm. Hence, we can conclude that a significant part of the crosstalk measured with SRB may be due to coherent errors such as over- and under-rotations of the qubits.

The same experiments on up to four qubits have been performed by Córcoles et al. in Ref. [21], where the authors obtain a smaller amount of crosstalk given by $\bar{r}_1^{(4)} \simeq 1.4\bar{r}_1^{(1)}$, and an increase of the average single qubit EPC with each added qubit of only about 0.1%. However, the parking frequencies of the qubits in this paper are more spaced out than ours (see Sec. 3.1), and all qubits have longer energy relaxation and dephasing times of around 30 μ s and 20 μ s, respectively. Thus, the EPCs from standard single qubit RB are all on the order of 0.1% in this reference.

The coherence limited EPC, r_{coh_lim} , for each qubit is shown in the last column of Table 4.1, with the last row showing the average coherence limited infidelity of all four qubits (see Sec. 3.2.2 for details about r_{coh_lim}). Since qubit 5 has very low coherence times below 3 μ s (Sec. 3.1), we see that this qubit has a rather large coherence limited infidelity of approximately 1.38%. The small coherence times of this qubit, as well as the leakage to the qubit $|f\rangle$ level due to a low value of the charging energy E_c defined in Sec. 2.1.1, are the most likely causes for the significantly higher EPCs of qubit 5 compared to those of the other three qubits (see Fig. 4.2 and Table 4.1).

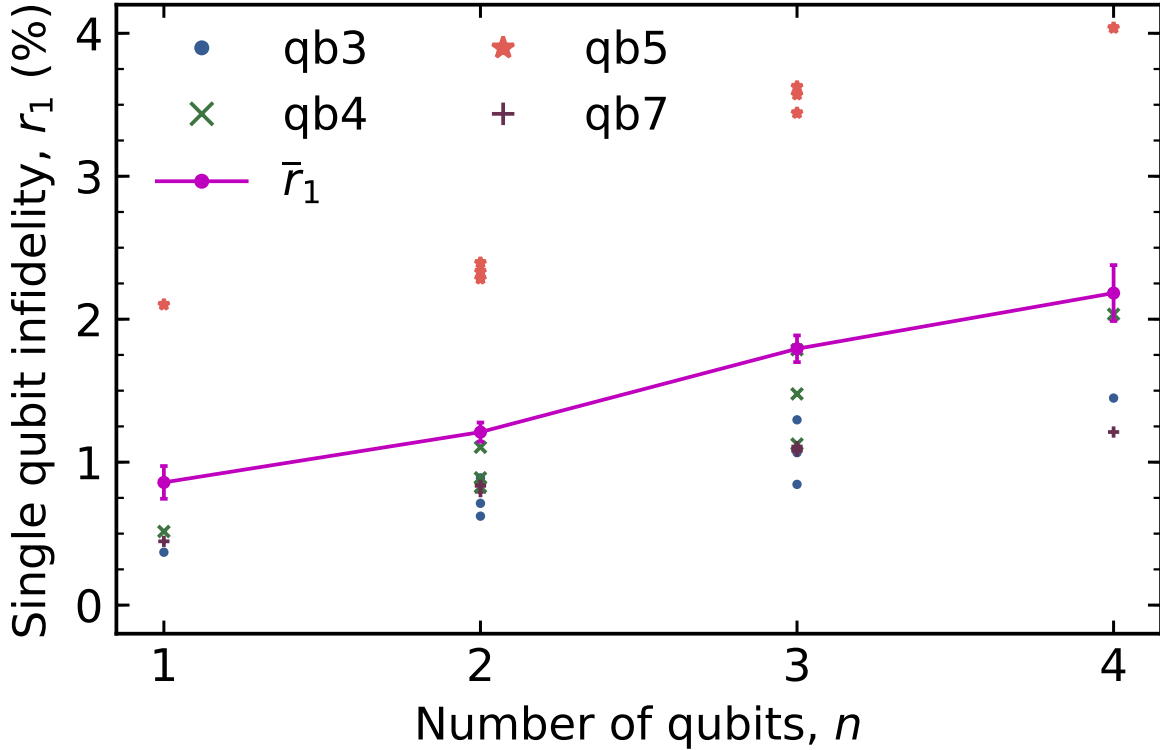


Figure 4.2: Single qubit EPCs for each qubit from all (S)RB experiments containing that qubit as a function of the number of simultaneously operated qubits n . The magenta points are the averages over all the EPCs for a given n , and they represent the average single qubit EPC from all four qubits when n qubits are operated simultaneously. The error bars represent the 68% confidence intervals obtained from the empirical standard deviations of the distributions of $K = 100$ different Clifford sequences for each sequence length m .

In Sec. 2.3.2 I explained that the constants A and B in the fit to Eq. (2.28),

$$A\alpha_1^m + B, \quad (4.2)$$

quantify the amount of SPAM errors in the (S)RB measurements. In particular, A captures the errors due to improper state preparation and poor readout fidelity, while B reflects systematic errors in the readout. The values for A and B obtained from the single qubit RB measurements for each of the four qubits shown in Fig. 4.1 are given in Table 4.2. As expected from the single shot readout calibration measurements for qubits 4 and 5 shown in Fig. 3.3, these qubits have higher values for the parameter B than the remaining two qubits. Notice also that qubit 4 has the lowest value for the parameter A, which may explain the lower assignment fidelity of qubit 4 (approximately 78%) compared to that of qubit 5 (about 83%). For all the (S)RB experiments presented in this thesis, the fit results were rescaled such that $B' = 0$ and $A' = A + B$. The rescaled parameters A' now capture all the SPAM errors, and their values for each qubit are shown in the last column of Table 4.2.

All the error bars in Fig. 4.1 and the error values in Tables 4.1 and 4.2 that are not in parentheses are obtained by using as weights for the fits to Eq. (4.2) the empirical standard deviations of the distributions of $K = 100$ different Clifford sequences for each

Qubit	A (%)	B (%)	A' (%)
Qb3	0.74 ± 0.23	0.16 ± 0.24	0.90 ± 0.33
Qb4	0.56 ± 0.14	0.25 ± 0.15	0.82 ± 0.20
Qb5	0.74 ± 0.03	0.21 ± 0.03	0.95 ± 0.04
Qb7	0.74 ± 0.17	0.18 ± 0.17	0.92 ± 0.24

Table 4.2: A and B coefficients from Eq. (4.2) quantifying the amount of errors due to improper qubit state preparation and poor readout fidelity, and due to systematic readout errors, respectively. $A' = A + B$ is the rescaled A parameter that now quantifies all SPAM errors.

sequence length m . The error values in parentheses in Table 4.1 were calculated using the estimation theory in Ref. [39], which quantifies the errors due to insufficient sampling of the single qubit Clifford group \mathcal{C}_1 for each qubit. See Sec. 3.2.2 for details about these two types of error bars. We see in Table 4.1 that in the single qubit experiments, the error values in parentheses account for around half of the corresponding empirical values, while in the SRB experiments they account for most of the corresponding empirical values. Thus, it appears that for the SRB experiments, insufficient sampling of \mathcal{C}_1 seems to be a significant limiting factor, while for the single qubit RB measurements we are limited by both experimental noise, and insufficient sampling of \mathcal{C}_1 .

4.2 Correlated errors in multi-qubit algorithms

The technique of using SRB to quantify the amount of correlated errors in a multi-qubit algorithm was introduced by Gambetta et al. in Ref. [9], where the authors performed the experiment on two qubits. Here we quantify the amount of correlated errors in simultaneous randomized benchmarking of up to four qubits using the theory in Sec. 2.3.3 and 2.3.5. Correlated errors refer to multi-qubit errors that do not act independently in each qubit subspace, but instead couple all or any subset of these subspaces. See Sec. 2.3.5 for a definition of multi-qubit correlated errors.

First, we calculate an ideal, lower bound on the multi-qubit errors in each n -qubit algorithm that we would expect to find if we had no crosstalk and no correlated errors. If we had no crosstalk, we would expect the single qubit EPCs from measurements of single qubit observables $\hat{\sigma}_{z,i}$ in all $n > 1$ SRB experiments to be equal to the EPCs obtained from standard single qubit RB on the respective qubits:

$$r_{1,i}^{(1)} = r_{1,i}^{(2)} = r_{1,i}^{(3)} = r_{1,i}^{(4)}, \quad (4.3)$$

where i indicates the qubit number. Thus, we calculate the multi-qubit error from single qubit RB measurements, $r_n^{(1)}$, using Eq. (2.55) for the completely uncorrelated multi-qubit error,

$$r_n^{(1)} = \frac{(2^n - 1)(1 - \bar{\alpha}_n^{(1)})}{2^n}, \quad (4.4)$$

$$\bar{\alpha}_n^{(1)} = \frac{1}{A} \left(\sum_{i \leq n} 3\alpha_i^{(1)} + \sum_{\substack{i,j \leq n \\ i < j}} 9\alpha_i^{(1)}\alpha_j^{(1)} + \sum_{\substack{i,j,k \leq n \\ i < j < k}} 27\alpha_i^{(1)}\alpha_j^{(1)}\alpha_k^{(1)} + \dots + 3^n \alpha_1^{(1)}\alpha_2^{(1)}\dots\alpha_n^{(1)} \right), \quad (4.5)$$

where now all the depolarizing parameters $\alpha_i^{(1)}$ in Eq. (4.5) are obtained from measuring $\langle \hat{\sigma}_{z,i} \rangle$ in the *single qubit* RB experiment on qubit i . We calculate these quantities for $n = 1, 2, 3, 4$ and plot the results as the green dot-dashed line in Fig. 4.3 (b). At the end of this section, we will compare the measured multi-qubit errors against this ideal quantity in order to see whether we can recover the amount of crosstalk found in Eq. (4.1) using the multi-qubit error analysis.

The first indication that correlated errors are present in our 4-qubit algorithm is shown in Fig. 4.3 (a). We have seen in Eq. (2.58) and Appendix B, that the depolarizing parameter from an s -qubit correlator measurement is greater than or equal to the product of depolarizing parameters from individual qubit measurements,

$$\alpha_{ij\dots s} \geq \alpha_i \alpha_j \dots \alpha_s, \quad (4.6)$$

with equality if all errors are completely uncorrelated. To check this inequality, we plot in Fig. 4.3 (a) the results from the 4-qubit correlator measurement in orange, and the product of single qubit results $\langle \hat{\sigma}_{z,3} \rangle \langle \hat{\sigma}_{z,4} \rangle \langle \hat{\sigma}_{z,5} \rangle \langle \hat{\sigma}_{z,7} \rangle = \langle \hat{\sigma}_z \rangle^{\otimes 4}$ in purple for each sequence length m . We can see that the expectation value of the product of single qubit observables $\langle \hat{\sigma}_z \rangle^{\otimes 4}$ decays faster with the sequence length m than the expectation value of the 4-qubit correlator $\langle \hat{\sigma}_z^{\otimes 4} \rangle$. From fits to these two traces, we extract $\alpha_{3457} \simeq 87.6 \pm 1.3\%$ and $\alpha_3 \alpha_4 \alpha_5 \alpha_7 \simeq 85.3 \pm 0.3\%$, where the indices indicate the qubits used in the experiment. Thus, we find $\alpha_{3457} > \alpha_3 \alpha_4 \alpha_5 \alpha_7$, which signals the presence of correlated errors in our 4-qubit algorithm.

In order to quantify the amount of correlated errors in each of the SRB experiments on all combinations of up to four qubits, we calculate all multi-qubit errors $r_{n \in \{1,2,3,4\}}$ defined in Eq. (2.50) and reproduced here for clarity:

$$r_n = \frac{(2^n - 1)(1 - \bar{\alpha}_n)}{2^n}, \quad (4.7)$$

$$\bar{\alpha}_n = \frac{1}{A} \left(\sum_{i \leq n} 3\alpha_i^{(n)} + \sum_{\substack{i,j \leq n \\ i < j}} 9\alpha_{ij}^{(n)} + \sum_{\substack{i,j,k \leq n \\ i < j < k}} 27\alpha_{ijk}^{(n)} + \dots + 3^n \alpha_{12\dots n}^{(n)} \right). \quad (4.8)$$

Thus, for example in the SRB experiment on $n = 4$ qubits, we measured all single qubit observables in order to obtain all the α_i , where i indicates the qubit number, and we calculated all possible correlators on $s \leq 4$ qubits in order to obtain all the $\alpha_{ij\dots s}$ in Eq. (4.8). As described in Sec. 3.1, this was achieved by saving all the shots for each qubit and averaging the products of all 4 or any subset $s < 4$ of these results shot-by-shot. For example, for $s = 3$, $n = 4$, we calculated the 4 3-qubit correlators between qubits 3-4-5, 3-4-7, 3-5-7, and 4-5-7 from the individual shots for each of these qubits measured in the 4-qubit SRB experiment.

The second column of Table 4.3 shows the multi-qubit errors from the (S)RB measurements on the qubits indicated by the numbers in the first column. The multi-qubit errors for the single qubit RB measurements are just the EPCs for the respective qubit, which were also shown in Table 4.1. In order to investigate how the multi-qubit error scales with the number of operated qubits n , we calculate the average of the multi-qubit errors from all experiments on n qubits. These average values are shown in bold in Table 4.3, and they are plotted in yellow (circles) in Fig. 4.3 (b) as a function of n , the number of qubits in the algorithm. We see that the multi-qubit error increases sharply with n , with a total 4-qubit error of around $9.32 \pm 0.46\%$. In Table 4.3 we see that all the experiments that

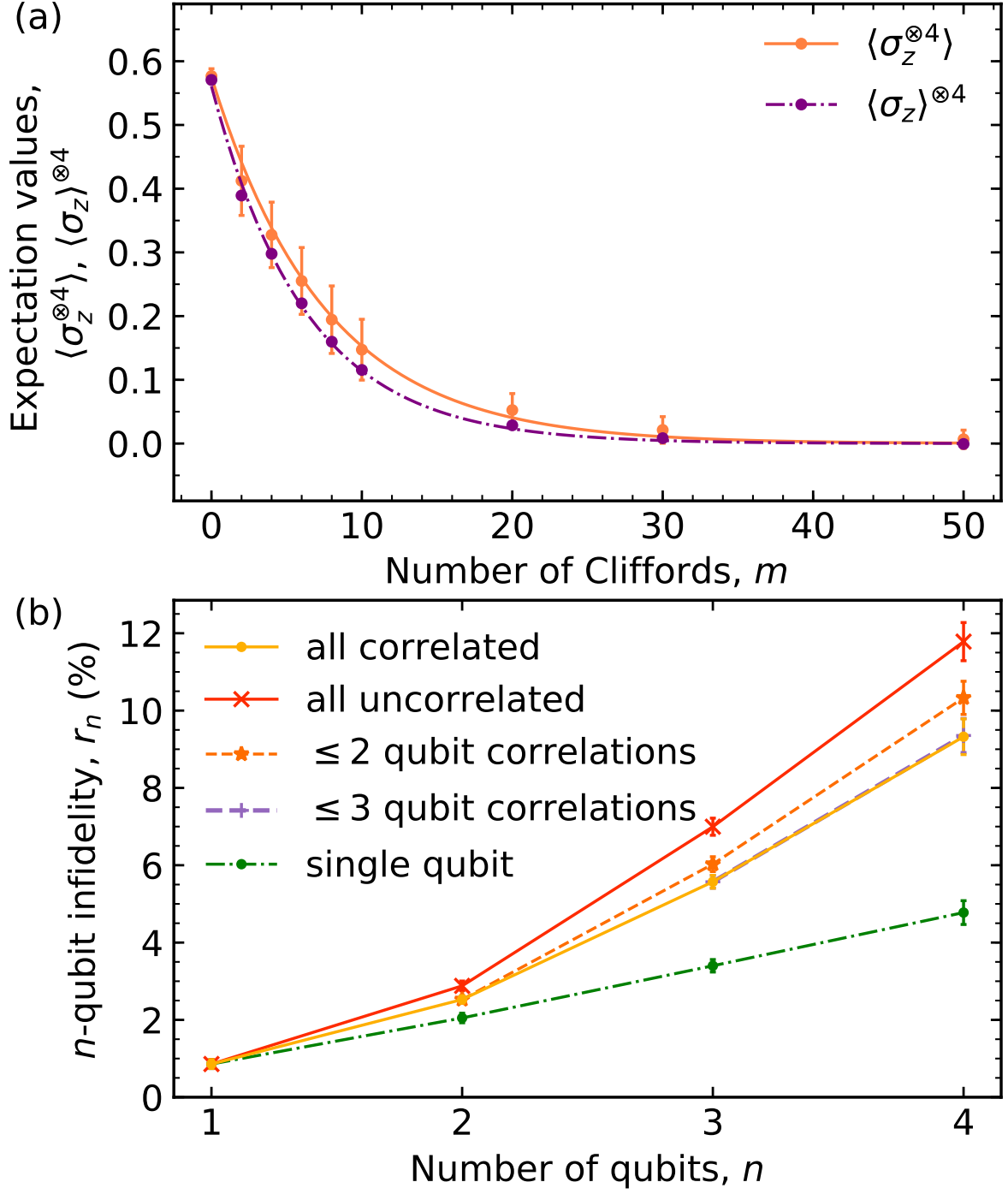


Figure 4.3: Correlated errors in multi-qubit algorithms. (a) The expectation value of the 4-qubit correlator $\langle \hat{\sigma}_z^{\otimes 4} \rangle$ (orange) and the product of the expectation values of the four single qubit observables $\langle \hat{\sigma}_z \rangle^{\otimes 4}$ (purple) as a function of the Clifford sequence length m . (b) The multi-qubit error as a function of the number of simultaneously operated qubits, n . Each line represents the multi-qubit error calculated under various assumptions about the type and degree of correlations: all correlators included in the calculations (r_n , yellow), assuming completely uncorrelated errors ($\tilde{r}_{n,1}$, red), only up to 2-qubit correlators included in the calculations ($\tilde{r}_{n,2}$, orange), only up to 3-qubit correlators included in the calculations ($\tilde{r}_{n,3}$, purple), assuming completely uncorrelated errors and no crosstalk ($r_n^{(1)}$, green). All error bars are 68% confidence intervals obtained from the empirical standard deviations of the distributions of $K = 100$ different Clifford sequences for each sequence length m .

contain qubit 5 have higher multi-qubit errors than the other experiments on n qubits. These results are to be expected due to the bad coherence properties of qubit 5 and its low charging energy E_c (see Sec. 4.1).

Qubit numbers	r_n (%)	Δr_n (%)	$\Delta r_n/r_n$ (%)
3	0.37 ± 0.16 (0.09)	-	-
4	0.51 ± 0.21 (0.13)	-	-
5	2.10 ± 0.34 (0.23)	-	-
7	0.45 ± 0.16 (0.09)	-	-
$n = 1$ average	0.86 ± 0.11 (0.07)	-	-
3,4	1.74 ± 0.15 (0.22)	0.38 ± 0.27	21.79 ± 15.65
3,5	3.12 ± 0.25 (0.31)	0.45 ± 0.44	14.33 ± 14.15
3,7	1.58 ± 0.15 (0.19)	0.11 ± 0.28	6.91 ± 17.52
4,5	3.75 ± 0.33 (0.43)	0.40 ± 0.48	10.80 ± 12.81
4,7	1.73 ± 0.17 (0.23)	0.26 ± 0.30	14.83 ± 17.62
5,7	3.25 ± 0.26 (0.32)	0.52 ± 0.47	15.92 ± 14.37
$n = 2$ average	2.53 ± 0.09 (0.12)	0.35 ± 0.16	14.10 ± 6.31
3,4,5	6.71 ± 0.40 (0.65)	1.97 ± 0.62	29.27 ± 9.46
3,4,7	3.59 ± 0.19 (0.33)	0.70 ± 0.33	19.42 ± 9.12
3,5,7	5.69 ± 0.32 (0.48)	1.52 ± 0.61	26.65 ± 10.87
4,5,7	6.29 ± 0.37 (0.59)	1.52 ± 0.59	24.12 ± 9.54
$n = 3$ average	5.57 ± 0.17 (0.26)	1.43 ± 0.28	24.87 ± 4.89
$3,4,5,7$	9.32 ± 0.46 (0.81)	2.46 ± 0.68	26.39 ± 7.36

Table 4.3: Multi-qubit errors r_n calculated from all subsets of correlators in each of the n -qubit (S)RB measurements shown in the first column, where the numbers indicate the qubits operated during each experiment. The second and third columns show the amount $\Delta r_n = \tilde{r}_{n,1} - r_n$ and percentage $\Delta r_n/r_n$ of correlated errors in the total multi-qubit error r_n . Both sets of error bars represent the 68% confidence intervals; the first set is obtained from the empirical standard deviations of the distributions of $K = 100$ different Clifford sequences for each sequence length m , while the errors in parentheses are upper bounds on the uncertainty due to finite sampling of the single qubit Clifford group.

In Eq. (2.58) in Sec. 2.3.5.2 I showed that we can quantify the amount of correlated errors in our algorithms as the difference $\Delta r_n = \tilde{r}_{n,1} - r_n$ between the completely uncorrelated multi-qubit error, $\tilde{r}_{n,1}$, and the multi-qubit error calculated from all correlators according to Eqs. (4.7)-(4.8). Hence, we calculate $\tilde{r}_{n,1}$ from Eq. (2.55), reproduced here for clarity:

$$\tilde{r}_{n,1} = \frac{(2^n - 1)(1 - \tilde{\alpha}_{n,1})}{2^n}, \quad (4.9)$$

$$\tilde{\alpha}_{n,1} = \frac{1}{A} \left(\sum_{i \leq n} 3\alpha_i^{(n)} + \sum_{\substack{i,j \leq n \\ i < j}} 9\alpha_i^{(n)}\alpha_j^{(n)} + \sum_{\substack{i,j,k \leq n \\ i < j < k}} 27\alpha_i^{(n)}\alpha_j^{(n)}\alpha_k^{(n)} + \dots + 3^n \alpha_1^{(n)}\alpha_2^{(n)} \dots \alpha_n^{(n)} \right). \quad (4.10)$$

All the depolarizing parameters $\alpha_i^{(n)}$ in Eq. (4.10) are obtained from measuring $\langle \hat{\sigma}_{z,i} \rangle$ for qubit i in the n -qubit SRB experiment. We calculate the averages of all the completely

uncorrelated multi-qubit errors for each n , and plot the results as a function of n in red (crosses) in Fig. 4.3 (b). The third column in Table 4.3 shows the amount of correlated errors Δr_n in the SRB experiments on the qubits in the first column, while the last column shows what percentage of the total, multi-qubit errors are correlated.

With the exception of SRB on qubits 3 and 7, the amount of correlated errors account for more than 10% of the multi-qubit errors, and as high as around 29% for SRB on qubits 3, 4, 5, and around 26% for SRB on all four qubits. In addition, notice how Δr_n depends on the position of the qubits on the processor (see Figs. 2.1 and 3.1). We expect the pairs and triplets of qubits that are connected by coupling resonators (nearest neighbors) to show larger amounts of correlated errors. We see in Table 4.3 that, as expected, the SRB experiment on qubits 3 and 7 has the smallest amount of correlated errors of around $0.11 \pm 0.28\%$, the experiment on qubits 3, 4, and 5 has the highest amount of correlated errors out of all 3-qubit experiments (around $1.97 \pm 0.62\%$), and the overall highest amount of correlated errors of around $2.46 \pm 0.68\%$ is found in the SRB experiment on all four qubits. However, SRB on qubits 3-4-5 and 3-5-7 have approximately the same amount of correlated errors within the error bars. Similarly, in the 2-qubit experiments, SRB on qubits 5-7 has a larger amount of correlated errors than SRB on qubits 4-5, and the SRB measurements on qubits 3-4 and 3-5 appear to have approximately the same amount of correlated errors of around 0.4%, even though qubits 3 and 5 do not share a coupling resonator. Nevertheless, Δr_2 for SRB on qubits 3-5 has very large relative error bars, and hence this result might be inconclusive. Since these unexpected results occur when qubit 5 is involved in the experiment, some of these effects might be explained by the bad properties of this qubit mentioned above.

Notice that for the 4-qubit experiment, we obtain the following relations between the completely uncorrelated multi-qubit error $\tilde{r}_{4,1}$ and the one obtained from single qubit measurements $r_4^{(1)}$, and between the multi-qubit error with all correlators r_4 and the one obtained from single qubit measurements:

$$\tilde{r}_{4,1} - r_4^{(1)} \simeq 7.00 \pm 0.58\%, \quad (4.11)$$

$$r_4 - r_4^{(1)} \simeq 4.55 \pm 0.55\%, \quad (4.12)$$

or

$$\tilde{r}_{4,1} \simeq 2.47r_4^{(1)}, \quad (4.13)$$

$$r_4 \simeq 1.95r_4^{(1)}. \quad (4.14)$$

Hence, we find a similar amount of crosstalk as we did in Eq. (4.1) if we compare the multi-qubit error from single qubit measurements to the completely uncorrelated multi-qubit error Eq. (4.13), not to the one that includes all correlators Eq. (4.14). This result is an indication that the crosstalk in our algorithms as defined in Sec. 4.1 might predominantly contain uncorrelated errors.

Moreover, notice that comparing $r_4^{(1)}$ to r_4 underestimates the amount of crosstalk. This effect occurs for the same reason why the completely uncorrelated multi-qubit errors $\tilde{r}_{n,1}$ are larger than r_n , see Fig. 4.3. The mathematical proof for this inequality is derived in Appendix B. Intuitively, this inequality makes sense because the $\hat{\sigma}_z^{\otimes n}$ correlator measurements are parity measurements: they return +1 (-1) if an even (odd) number of the n qubits are in the excited state [31]. Hence, an error that flips n qubits simultaneously

is detected as one single error by the correlator measurement, but as n errors by the n single qubit measurements. This means that the n -qubit fidelities calculated from all correlators (Eq. (4.8)) will be larger than the ones calculated by multiplying together the single qubit fidelities obtained by tracing out all other qubits.

In order to understand better the results from SRB, we also measured the pairwise $\sigma_z\sigma_z$ -coupling with Ramsey measurements as described in Sec. 2.2.2. We find a coupling rate of around 300 kHz between qubits 3-4, and of around 600 kHz between qubits 4-5. If we compare these rates to the average duration of a Clifford gate of 28.125 ns, we would expect to find on average around 5.3% and 10.6% correlated errors per Clifford between qubits 3-4 and 4-5, respectively. We do not observe such strong contributions in the SRB results in Table 4.3. This is an indication that, either the errors affecting the SRB protocols are not directly proportional to the errors due to the $\sigma_z\sigma_z$ -coupling, or that the SRB protocols might capture additional multi-qubit errors that are not seen in typical pairwise measurements of the $\sigma_z\sigma_z$ -coupling.

In addition to using SRB to quantify the amount of correlated errors in multi-qubit algorithms, we also use SRB to investigate the degree of the correlated errors. I.e. we try to identify the smallest correlated qubit subspace that we need to assume in our analysis in order to describe the multi-qubit errors r_n in each n -qubit SRB experiment. To do this we use the theory developed in Sec. 2.3.5.3 to calculate lower bounds on the multi-qubit errors when we assume correlations on only up to $s < n$ qubits. When we assume to have only up to $s = 2$ -qubit correlations, the multi-qubit errors from SRB experiments on $n = 1, 2, 3, 4$ qubits are given by:

$$\begin{aligned}\tilde{r}_{1,2} &= r_1, \\ \tilde{r}_{2,2} &= r_2, \\ \tilde{r}_{3,2} &= \frac{(2^3 - 1)(1 - \tilde{\alpha}_{3,2}^{\max})}{2^3}, \\ \tilde{r}_{4,2} &= \frac{(2^4 - 1)(1 - \tilde{\alpha}_{4,2}^{\max})}{2^4}.\end{aligned}\tag{4.15}$$

The depolarizing parameters $\tilde{\alpha}_{3,2}^{\max}$ and $\tilde{\alpha}_{4,2}^{\max}$ are upper bounds on the corresponding total depolarizing parameters calculated only from α_i and α_{ij} obtained from measuring single qubit observables and from the measurements of 2-qubit correlators, respectively (see Sec. 2.3.5.3 and in particular Eq. (2.65)).

We calculate the quantities in Eq. (4.15) for all the SRB experiments on the sets of qubits indicated in the first column of Table 4.3, and, as before, we average the results from all n -qubit measurements. These average values are shown by the orange stars in Fig. 4.3 (b) (the value at $n = 2$ is identical to r_2). We see that $\tilde{r}_{n,2}$ (orange) $>$ r_n (yellow) for $n = 3$ and $n = 4$. Quantitatively, for the 3-qubit algorithm we have $\tilde{r}_{3,2} - r_3 \simeq 0.46 \pm 0.25\%$, and for the 4-qubit algorithm we find $\tilde{r}_{4,2} - r_4 \simeq 1.00 \pm 0.63\%$. These values account for less than half of the total amount of correlated errors of around $1.43 \pm 0.28\%$ for $n = 3$, and around $2.46 \pm 0.68\%$ for $n = 4$, see Table 4.3. However, even though these values are lower bounds of the true multi-qubit errors with up to 2-qubit correlations, within the confidence intervals we cannot conclude that we only have 2-qubit correlations in our algorithms. However, we can say that these correlations make up a significant part of the total amount of correlated errors.

We have also looked at the lower bounds on the multi-qubit errors calculated by assuming up to $s = 3$ -qubit correlations, i.e. both 2- and 3-qubit correlations, but no

4-qubit correlated errors. In this case, the multi-qubit errors from SRB experiments on $n = 1, 2, 3, 4$ qubits are given by (see Sec. 2.3.5.3):

$$\begin{aligned}\tilde{r}_{1,3} &= r_1, \\ \tilde{r}_{2,3} &= r_2, \\ \tilde{r}_{3,3} &= r_3, \\ \tilde{r}_{4,3} &= \frac{(2^4 - 1)(1 - \tilde{\alpha}_{4,3}^{\max})}{2^4},\end{aligned}\tag{4.16}$$

with the depolarizing parameter $\tilde{\alpha}_{4,3}^{\max}$ given by Eq. (2.65), which was calculated only from α_i obtained from measuring single qubit observables, and both α_{ij} and α_{ijk} obtained from the measurements of 2- and 3-qubit correlators.

Again we calculate $\tilde{r}_{4,3}$ for the 4-qubit experiment according to Eq. (4.16), and plot the result as the purple dashed line in Fig. 4.3 (b) (the value at $n = 3$ is identical to r_3). $\tilde{r}_{4,3}$ almost completely overlaps the yellow multi-qubit error r_4 calculated from all correlators (Eq. (4.7)), with a difference of $\tilde{r}_{4,3} - r_4 \simeq 0.03 \pm 0.64\%$. Remembering that the value of $\tilde{r}_{4,3}$ is only a lower bound of the true multi-qubit error with up to 3-qubit correlations, we can conclude that this result is an indication that our 4-qubit algorithm likely contains no effects from 4-qubit correlated errors.

Note from the discussion above and from Fig. 4.3 (b), that we have experimentally verified the expected hierarchy in Eq. (B.3) derived at the end of Appendix B:

$$\bar{r}_4 \leq \tilde{r}_{4,3} \leq \tilde{r}_{4,2} \leq \tilde{r}_{4,1}.\tag{4.17}$$

I will end this section with a brief discussion about the error bars around our results. All confidence intervals shown in Fig. 4.3 and in Table 4.3 that are not in parentheses are obtained by using the empirical standard deviations of the distributions of $K = 100$ different Clifford sequences for each sequence length m (see Sec. 3.2.2). The values in parentheses in Table 4.3 are calculated from the following upper bounds for the variance of the distribution of K averaged multi-qubit RB sequences derived by Helsen et al. [47]:

$$\begin{aligned}V_{\text{mq}}(m) &\leq \frac{d^2 - 2}{4(d-1)^2} m r_0^2 \alpha_0^{m-1} + \frac{d^2}{(d-1)^2} r_0^2 \frac{1 + (m-1)\alpha_0^{2m} - m\alpha_0^{2(m-1)}}{(1 - \alpha_0^2)^4}, \quad \text{all } m \\ V_{\text{mq}}(m) &\leq \frac{d^2 - 2}{4(d-1)^2} r_0^2 + \frac{d^2 m(m-1)}{2(d-1)^2} r_0^2, \quad mr_0 < 1,\end{aligned}\tag{4.18}$$

where $d = 2^n$, and r_0 and α_0 are previous estimates of the infidelity and depolarizing parameter. These bounds for the variance are the multi-qubit equivalents of the quantities for the single qubit case discussed in Eq. (3.5) in Sec. 3.2.2.

However, the estimates in Eq. (4.18) were derived for a full n -qubit RB experiment where the twirl is over the full n -qubit Clifford group, \mathcal{C}_n (see Sec. 2.3.5.1). In the SRB experiments, we are instead twirling with the n -fold tensor product of the single qubit Clifford group, $\mathcal{C}_1^{\otimes n}$ (see Sec. 2.3.3). Thus, it has not been proven that the upper bounds in Eq. (4.18) apply to the n -qubit SRB experiments. However, following the same procedure as explained in Sec. 3.2.2, we calculated the 68% confidence intervals around the expectations values $\langle \hat{\sigma}_z^{\otimes n} \rangle$ for each m using the bounds in Eq. (4.18). We verified that for all

SRB experiments, almost all these intervals are larger than the 68% confidence intervals calculated from the empirical standard deviations. We can also see in Table 4.3 that all error values in parentheses for $n > 1$ qubits are larger than the values in front, obtained from the empirical standard deviations. Hence, we can conclude as we did in Sec. 4.1, that our SRB experiments are most probably limited more by insufficient sampling of the group \mathcal{C}_1 for each qubit, than by experimental imperfections.

4.3 Readout crosstalk in SRB experiments

In this section I will briefly discuss the potential effects of crosstalk from multiplexed readout (MRO) on the SRB experiments, and I will show that the results presented in the previous two sections were most likely not greatly influenced by these readout (RO) errors.

As already mentioned in Sec. 2.2.2, the consequence of MRO crosstalk is that we would measure the correlators of qubits whose readout resonators are close in frequency instead of only measuring single qubit observables. Hence, there is the possibility that some or even a significant amount of the correlated errors we measured with SRB are in fact due to crosstalk in the MRO. In order to investigate whether this might be the case, we add various amounts of MRO crosstalk on top of our results from single qubit observables in order to see how and by how much do these errors affect our results. In particular, we look at the inequality in Eq. (4.6) for an n -qubit SRB experiment,

$$\alpha_{12\dots n} \geq \alpha_1 \alpha_2 \dots \alpha_n, \quad (4.19)$$

where $\alpha_{12\dots n}$ is the depolarizing parameter obtained from measuring the n -qubit correlator $\hat{\sigma}_z^{\otimes n}$, and the right hand side is the product of depolarizing parameters from measuring all the n single qubit observables. We then add the same amount of MRO crosstalk ϵ between all n qubits according to:

$$\begin{aligned} \text{output}_1 &= [1 - (n - 1)\epsilon] \alpha_1^m + \epsilon \alpha_2^m + \epsilon \alpha_3^m + \dots + \epsilon \alpha_n^m, \\ \text{output}_2 &= [1 - (n - 1)\epsilon] \alpha_2^m + \epsilon \alpha_1^m + \epsilon \alpha_3^m + \dots + \epsilon \alpha_n^m, \\ &\dots \\ \text{output}_n &= [1 - (n - 1)\epsilon] \alpha_n^m + \epsilon \alpha_1^m + \epsilon \alpha_2^m + \dots + \epsilon \alpha_{n-1}^m, \end{aligned}$$

where m is the Clifford sequence length. We obtain the product of single qubit depolarizing parameters with ϵ amount of added crosstalk, $(\alpha_1 \alpha_2 \dots \alpha_n)_\epsilon$, from fitting the following equation:

$$\text{output}_1 \cdot \text{output}_2 \cdot \dots \cdot \text{output}_n = A(\alpha_1 \alpha_2 \dots \alpha_n)_\epsilon + B. \quad (4.20)$$

If the correlated errors that we quantify by $\Delta\alpha = \alpha_{12\dots n} - \alpha_1 \alpha_2 \dots \alpha_n$ in the SRB experiments were due to crosstalk in the multiplexed RO, then we would expect that adding additional crosstalk would further increase the difference $\Delta\alpha$. Table 4.4 shows $\alpha_{12\dots n}$, $\alpha_1 \alpha_2 \dots \alpha_n$, and $\Delta\alpha$ for all SRB experiments on $n = 2, 3, 4$ qubits. The last three columns show the results $\Delta\alpha_\epsilon = \alpha_{12\dots n} - (\alpha_1 \alpha_2 \dots \alpha_n)_\epsilon$ from adding MRO crosstalk ϵ of 5%, 25%, and 50%, as explained above. We see that by adding the multiplexed readout errors we *decrease* $\Delta\alpha$. Thus, it appears that the effect of crosstalk in multiplexed RO is

not to produce more correlated errors, but to hide some of the correlated errors that can be detected with the SRB formalism.

From independent measurements (see Sec. 2.2), we estimate to have around 5% crosstalk in the multiplexed RO [5]. Table 4.4 shows that the largest change in the estimated amount of correlated errors due to such a low ϵ is only around 0.2%, which is smaller or approximately equal to the error bars. Another potential effect of these RO errors is to cause the measured single qubit observables $\langle \hat{\sigma}_z \rangle$ to decay with multiple decay constants corresponding to the depolarizing channels acting in the other qubit subspaces accessed during multiplexed readout. This effect would result in poor fits to the single exponential decay in Eq. (4.2) that has been used throughout this project, and these poor fits would give large empirical confidence intervals around the quantities of interest. Yet, we have seen in Table 4.1 that we obtain small 68% confidence intervals of at most approximately 0.6% around the single qubit EPCs obtained from measuring individual qubit subspaces in the n -qubit SRB experiments. Hence, we can conclude that the results presented in Sec. 4.1 and Sec. 4.2 are most likely not strongly influenced by the crosstalk in the multiplexed RO, and that our SRB experiments truly quantify the amounts of crosstalk and correlated errors in the n -qubit algorithms.

Qubit numbers	$\alpha_{12..n}$ (%)	$\alpha_1\alpha_2\dots\alpha_n$ (%)	$\Delta\alpha$ (%)	$\Delta\alpha_{\epsilon=5\%}$ (%)	$\Delta\alpha_{\epsilon=25\%}$ (%)	$\Delta\alpha_{\epsilon=50\%}$ (%)
3,4	97.32 ± 0.30	96.47 ± 0.78	0.84 ± 0.56	0.84 ± 0.30	0.84 ± 0.30	0.84 ± 0.30
3,5	95.07 ± 0.50	94.07 ± 0.76	0.99 ± 0.91	0.93 ± 0.50	0.74 ± 0.51	0.65 ± 0.51
3,7	97.43 ± 0.30	97.19 ± 0.49	0.24 ± 0.57	0.24 ± 0.30	0.24 ± 0.30	0.24 ± 0.30
4,5	94.01 ± 0.70	93.11 ± 0.72	0.90 ± 1.00	0.86 ± 0.70	0.73 ± 0.70	0.68 ± 0.70
4,7	97.27 ± 0.33	96.71 ± 0.53	0.57 ± 0.62	0.57 ± 0.33	0.57 ± 0.33	0.57 ± 0.33
5,7	94.89 ± 0.52	93.74 ± 0.81	1.15 ± 0.96	1.09 ± 0.52	0.92 ± 0.52	0.84 ± 0.53
3,4,5	90.94 ± 0.94	87.11 ± 1.14	3.83 ± 1.48	3.71 ± 0.94	3.41 ± 0.94	3.49 ± 0.94
3,4,7	94.80 ± 0.46	93.60 ± 0.63	1.20 ± 0.78	1.20 ± 0.46	1.20 ± 0.46	1.20 ± 0.46
3,5,7	91.82 ± 0.76	89.26 ± 1.25	2.56 ± 1.46	2.34 ± 0.76	1.82 ± 0.78	1.95 ± 0.78
4,5,7	91.37 ± 0.87	88.40 ± 1.10	2.97 ± 1.40	2.83 ± 0.87	2.49 ± 0.88	2.58 ± 0.88
3,4,5,7	87.58 ± 1.34	83.56 ± 1.38	4.02 ± 1.94	3.81 ± 1.34	3.44 ± 1.34	3.93 ± 1.34

Table 4.4: Quantifying the amount of correlated errors when we add MRO crosstalk to the results from the SRB experiments performed on the qubits indicated by the numbers in the first column. The second and third columns show respectively the depolarizing parameter from the n -qubit correlator measurement, and the product of n depolarizing parameters from measuring all n single qubit observables. $\Delta\alpha$ is the difference between the first and second columns, and it quantifies the amount of correlated errors in the algorithm. $\Delta\alpha_\epsilon$ quantifies the amount of correlated errors after adding 5%, 25%, and 50% MRO crosstalk to the SRB results.

5 Conclusions and outlook

In this project we performed standard randomized benchmarking (RB) and simultaneous RB (SRB) on all combinations of $n = 1, 2, 3, 4$ qubits using the qubits 3, 4, 5, and 7 on an 8-superconducting-qubit quantum processor. The novelty of this project is that, in addition to measuring all n single qubit observables $\hat{\sigma}_z$ in each n -qubit experiment, we also measured correlators $\hat{\sigma}_z^{\otimes s}$ on all possible combinations of $s \leq n$ qubits.

For all experiments, we used the new HVZ decomposition of the elements in the single qubit Clifford group into physical X gates and virtual Z gates, and we demonstrated that this decomposition gives smaller single qubit average infidelities than the $XY_{\frac{\pi}{2}}$ decomposition, which has on average more physical gates per Clifford element (Sec. 3.2.2).

We used the thresholding feature of our detection instrument, the UHFQC, to perform qubit state discrimination in single shot readout simultaneously on n qubits directly in our acquisition device, which leads to a significant data reduction (Sec. 3.1). We also used the correlator unit of the UHFQC in order to measure the thresholded 2-qubit $\hat{\sigma}_z\hat{\sigma}_z$ correlators of each shot. Due to a limitation of the correlator unit to only 2 qubits, for the experiments on $n > 2$ qubits we saved all the thresholded shots for each qubit, and calculated the correlators in our data analysis (Sec. 3.1).

From the measurements of all n single qubit observables in each n -qubit SRB experiment, we quantified the amount of crosstalk in our multi-qubit algorithms, defined here as the increase in the average single qubit errors per Clifford (EPCs) with the number of qubits operated simultaneously, n . We find that, due to crosstalk, the average single qubit EPC over all four qubits is around 2.5 times larger when we operate all four qubits in SRB, $\bar{r}_1^{(4)}$, compared to when we only operate one qubit at a time in standard RB, $\bar{r}_1^{(1)}$ (Sec. 4.1):

$$\boxed{\text{Cross-talk : } \bar{r}_1^{(4)} \simeq 2.5\bar{r}_1^{(1)}}.$$

From measurements of all subsets of correlators in each n -qubit SRB experiment, we calculated the multi-qubit error on n qubits, r_n , associated with each simultaneous application of n Clifford elements, i.e. the total infidelity of the n -qubit error channel $\tilde{\mathcal{E}}_{\otimes n}$ implemented by each SRB protocol. We quantified the amount of errors that couple to more than one qubit subspace (correlated errors) as the difference $\Delta r = \tilde{r}_{n,1} - r_n$ between the completely uncorrelated multi-qubit error, $\tilde{r}_{n,1}$, and the multi-qubit error containing all correlators, r_n (Sec. 4.2). For the 4-qubit SRB experiment, we find a total infidelity from all correlators of around 9%, and approximately 2.5% correlated errors, which thus account for around 26% of the total amount of errors:

$$\boxed{\begin{aligned} \text{Total infidelity : } & r_4 \simeq 9.32 \pm 0.46\%, \\ \text{Correlated errors : } & \Delta r_4 \simeq 2.46 \pm 0.68\%, \\ & \frac{\Delta r_4}{r_4} \simeq 26.39 \pm 7.36\%. \end{aligned}}$$

We also investigated what is the smallest correlated subspace that we need to assume in our calculation of the multi-qubit error in order to describe the multi-qubit error calculated from all correlators (Sec. 4.2). We found lower bounds of the multi-qubit errors calculated by assuming to have completely uncorrelated errors and only 2-qubit correlated errors. For the 4-qubit SRB experiment, we find a difference of around 1% between this lower bound $\tilde{r}_{4,2}$, and the total 4-qubit error r_4 that assumes all degrees of correlators,

which we can interpret as the approximate amount of 2- and -3 qubit correlated errors in our algorithm:

$$2\text{- and }3\text{-qubit correlated errors : } \Delta r_{4,2} = \tilde{r}_{4,2} - r_4 \simeq 1.00 \pm 0.63\%.$$

We also calculate the lower bounds of the 4-qubit error by assuming to have completely uncorrelated errors and both 2- and 3-qubit correlated errors, but no 4-qubit correlations. We obtain almost no difference between this lower bound, $\tilde{r}_{4,3}$, and the total 4-qubit error, r_4 , assuming all degrees of correlators:

$$4\text{-qubit correlated errors : } \Delta r_{4,3} = \tilde{r}_{4,3} - r_4 \simeq 0.03 \pm 0.64\%.$$

From these lower bounds and within the confidence intervals, we can conclude that 2-qubit correlations have a significant contribution to our correlated errors, but they may not completely explain them. However, we have a good indication that we may not have 4-qubit correlated errors in our algorithms.

In the future we will use the techniques presented in this thesis to quantify the multi-qubit crosstalk and correlated errors in algorithms on up to 8 or more qubits. We saw in Figs. 4.2 and 4.3 that both crosstalk and the correlated errors continue to increase up to $n = 4$ qubits. We will investigate whether these metrics continue to increase even for $n > 4$, in order to test the feasibility of our processor and our setup for achieving the error correction thresholds for fault-tolerance, which assume uncorrelated errors that do not increase indefinitely with the number of qubits in the algorithm.

In addition, we will also perform a more rigorous analysis of the degrees of error correlations in our algorithms than the one described in Sec. 2.3.5, where we only estimated lower bounds on the multi-qubit errors calculated from correlated errors on at most $s < n$ qubits. A more careful analysis would allow us to determine the dominant source of correlated errors that we must reduce as we move towards implementing fault-tolerant quantum error corrections codes.

Acknowledgements

I would like to thank my supervisor Dr. Christian Kraglund Andersen for his valuable support and guidance throughout the entire project. I greatly appreciate all the insightful discussions about the theory of this project and everything he has taught me in the lab during the implementation of our experiments. I am also grateful for the opportunity to complete this challenging and rewarding project in a very pleasant and productive working relationship with my supervisor.

I thank Prof. Andreas Wallraff for the opportunity to complete my Master's thesis project in his group at the Quantum Device Lab, which he ensures is always a center of excellence in a very dynamic research field. I am very grateful to have completed this project in a proficiently run, state-of-the-art quantum computing research facility.

I would also like to thank Christopher Eichler for insightful discussions and feedback related to my project. I greatly appreciate and am very thankful to Ants Remm and Johannes Heinsoo for the guidance and support, the very helpful discussions, and for the fun and productive working environment. They have both always made time to help me in the lab and to discuss any ideas or questions that I had related to my work during this project. I also thank the rest of the quantum computing team at the time of this writing, Jonas Butscher, Simon Storz, and Sebastian Krinner, for their valuable help in the lab, the productive discussions, and the overall friendly working atmosphere.

I thank the fabrication team, Anton Potočnik, Simone Gasparinetti, Jean-Claude Besse, and Mihai Gabureac, for the processor that was used to perform the work during this project, and for their valuable efforts to optimize and improve our fabrication techniques.

Finally, I warmly thank the entire QuDev team for their support, the insightful discussions, and the friendly and productive working atmosphere during this project.

I acknowledge financial support from the Swiss National Centre of Competence in Research (NCCR) Quantum Science and Technology (QSIT) during my Master's thesis project.

Appendices

Appendix A Driving a two-level system

In this appendix I will derive the Hamiltonian for a coherently driven transmon, and the induced AC-Stark shift of its first energy transition $E_{01} = \hbar\omega_q$ if the drive frequency ω_d is detuned from the qubit frequency ω_q . I will make use of Ch. 2 in Ref. [43], which describes the interaction between polarized radiation and an atom with radius r_0 , under the assumption that $kr_0 \ll 1$, where k is the polarization vector of the electromagnetic wave. Thus, we assume that the electromagnetic field varies very little across the size of the atom.

We will start by assuming an incident monochromatic radiation field at frequency ω_d , whose electric field component is described by

$$\vec{E}(t) = \frac{1}{2} [\vec{A}(t)e^{-i\omega_dt} + \vec{A}(t)^*e^{i\omega_dt}]. \quad (\text{A.1})$$

We further express the complex amplitude A as

$$\vec{A}(t) = \vec{A}_0(t)e^{-i\phi}, \quad (\text{A.2})$$

where ϕ is the phase of the wave, and we obtain

$$\vec{E}(t) = \frac{1}{2} \vec{A}_0(t) [e^{-i(\omega_dt+\phi)} + e^{i(\omega_dt+\phi)}]. \quad (\text{A.3})$$

We only focus on the electric field component since the dominant interaction between the incident radiation field and our (artificial) atom arises from the potential energy of the electric dipole of the atom in the electric field of the radiation wave. Therefore we can write the Hamiltonian describing the dynamics of a driven transmon as

$$\hat{H}_{\text{drive}} = \frac{\hbar\omega_q}{2} \hat{\sigma}_z + \hat{H}_{\text{int}}(t), \quad (\text{A.4})$$

where the first term is the energy of the qubit and the second term is the interaction Hamiltonian. If we assume \vec{A}_0 points in the \vec{x} direction, then $\vec{d} = -e\vec{x}$ is the electric dipole moment of the transmon and we can write

$$\hat{H}_{\text{int}}(t) = -\vec{d} \cdot \vec{E}(t). \quad (\text{A.5})$$

Since the atom possesses inversion symmetry, it follows that [43]

$$\langle 0 | \vec{d} | 0 \rangle = \langle 1 | \vec{d} | 1 \rangle = 0 \quad (\text{A.6})$$

$$\langle 0 | \vec{d} | 1 \rangle = \langle 1 | \vec{d} | 0 \rangle = -eX_{01}, \quad (\text{A.7})$$

with $X_{01} = \langle 0 | \vec{x} | 1 \rangle$. Therefore, we can write the interaction Hamiltonian in the $\{|0\rangle, |1\rangle\}$ basis as

$$\hat{H}_{\text{int}}(t) = eX_{01}(\hat{\sigma}^+ + \hat{\sigma}^-) \cdot \frac{1}{2} \vec{A}_0(t) [e^{-i(\omega_dt+\phi)} + e^{i(\omega_dt+\phi)}]. \quad (\text{A.8})$$

where $\hat{\sigma}^+ = |1\rangle\langle 0|$ and $\hat{\sigma}^- = |0\rangle\langle 1|$. Next we will use the rotating wave approximation (RWA) $|\omega_q - \omega_d| \ll \omega_q$ to neglect the terms proportional to $\hat{\sigma}^+e^{i\omega_dt}$ and $\hat{\sigma}^-e^{-i\omega_dt}$. For an

unperturbed atom, the time-evolution of $\hat{\sigma}^\pm$ is described by $\hat{\sigma}^\pm(t) = \hat{\sigma}^\pm(0)e^{\pm i\omega_q t}$. In the RWA, the neglected terms proportional to $e^{\pm i(\omega_q + \omega_d)t}$ rotate at a much faster rate $\omega_q + \omega_d$ compared to the remaining terms rotating at $\omega_q - \omega_d$. Therefore, these fast-oscillating terms are on average equal to zero, and the total Hamiltonian becomes

$$\hat{H}_{\text{drive}} = \frac{\hbar\omega_q}{2}\hat{\sigma}_z + \frac{1}{2}\hbar e X_{01} \vec{A}_0(t) \left[e^{-i(\omega_d t + \phi)}\sigma^- + e^{i(\omega_d t + \phi)}\sigma^+ \right]. \quad (\text{A.9})$$

Defining $\Omega_R(t) = eA_0(t)X_{01}/\hbar$ as the *Rabi frequency* of the transmon induced by the external field, we can rewrite this Hamiltonian in the following matrix form:

$$\hat{H}_{\text{drive}} = \begin{pmatrix} \hbar\omega_0/2 & \hbar(\Omega_R/2)e^{-i(\omega_d t + \phi)} \\ \hbar(\Omega_R/2)e^{i(\omega_d t + \phi)} & -\hbar\omega_0/2 \end{pmatrix}. \quad (\text{A.10})$$

We use the unitary transformation

$$\hat{U} = \begin{pmatrix} 1 & 0 \\ 0 & e^{i\omega_d t} \end{pmatrix}, \quad (\text{A.11})$$

to transform into a frame rotating at ω_d . Then our Hamiltonian becomes

$$\hat{H}_{\text{drive}} = \begin{pmatrix} \hbar\Delta\omega_{q,d}/2 & \hbar(\Omega_R/2)e^{-i\phi} \\ \hbar(\Omega_R/2)e^{i\phi} & -\hbar\Delta\omega_{q,d}/2 \end{pmatrix}, \quad (\text{A.12})$$

where $\Delta\omega_{q,d} = \omega_q - \omega_d$, or, using that $e^{\pm i\phi} = \cos(\phi) \pm i\sin(\phi)$,

$$\hat{H}_{\text{drive}} = \hbar \frac{\omega_q - \omega_d}{2} \hat{\sigma}_z + \frac{\hbar\Omega_R(t)}{2} (\cos(\phi)\hat{\sigma}_x + \sin(\phi)\hat{\sigma}_y),$$

which is the Hamiltonian in Eq. (2.6) in Sec. 2.1.1. The time-dependence in $\Omega_R(t)$ comes from $A_0(t)$; above I have been writing Ω_R for simplicity.

To obtain the AC-Stark shift of the energy levels of the transmon due to the off-resonant incident radiation detuned by $\Delta\omega_{q,d} = \omega_q - \omega_d$, we find the eigenenergies of \hat{H}_{drive} given by the eigenvalues of Eq. (A.13):

$$\begin{vmatrix} \hbar\Delta\omega_{q,d}/2 - E_{01}^\pm & \hbar\Omega_R/2 \\ \hbar\Omega_R^*/2 & -\hbar\Delta\omega_{q,d}/2 - E_{01}^\pm \end{vmatrix} = 0. \quad (\text{A.13})$$

Here, I have absorbed the phase into Ω_R , which is now a complex quantity. The eigenenergies are

$$E_{01}^\pm = \pm \hbar \sqrt{\left(\frac{\Delta\omega_{q,d}}{2}\right)^2 + \left(\frac{\Omega_R}{2}\right)^2}. \quad (\text{A.14})$$

If the detuning is very large $\Delta\omega_{q,d} \gg \Omega_R$, then we can use the approximation $\sqrt{1+x^2} \simeq 1 + x^2/2$ to write

$$E_{01}^\pm \simeq \pm \left(\frac{\hbar\Delta\omega_{q,d}}{2} + \frac{\hbar\Omega_R^2}{4\Delta\omega_{q,d}} \right). \quad (\text{A.15})$$

We see that in this limit the so-called *bare* qubit frequencies $\pm\Delta\omega_{q,d}/2$ are shifted by the *AC-Stark shift* $\Omega_R^2/4\Delta\omega_{q,d}$.

Appendix B Derivation of the inequality between correlated and uncorrelated depolarizing parameters

In this appendix I will prove that the product of two depolarizing parameters $\alpha_1^{(2)}$, $\alpha_2^{(2)}$ obtained from measurements of single qubit observables $\langle \hat{\sigma}_z \rangle$ in a 2-qubit SRB experiment is less than or equal to the depolarizing parameter $\alpha_{12}^{(2)}$ obtained from measuring the two-qubit correlator $\langle \hat{\sigma}_z \hat{\sigma}_z \rangle$:

$$\alpha_1^{(2)} \alpha_2^{(2)} \leq \alpha_{12}^{(2)}. \quad (\text{B.1})$$

I will then use this result to argue that the same relation is also true for SRB experiments on any number of qubits.

To prove Eq. (B.1), I will describe the total depolarizing channel associated with the 2-qubit SRB experiment in the general framework introduced in Sec. 2.3.5. Hence, the channel is given by Eq. (2.59), reproduced here for clarity:

$$\Lambda_{12}^{(2)} = a_2 \Lambda_{12} + b_2 \Lambda_1 \circ \Lambda_2.$$

As mentioned before, we obtain the depolarizing parameters $\alpha_1^{(2)}$, $\alpha_2^{(2)}$, $\alpha_{12}^{(2)}$ from measurements of $\langle \sigma_{z,1} \rangle$, $\langle \sigma_{z,2} \rangle$, and $\langle \sigma_{z,1} \sigma_{z,2} \rangle$, respectively. We write these parameters in a similar way as we wrote $\alpha_{12}^{(4)}$ in Eq. (2.62):

$$\begin{aligned} \alpha_1^{(2)} &= a_2 \alpha_{12} + b_2 \alpha_1 \leq 1 \\ \alpha_2^{(2)} &= a_2 \alpha_{12} + b_2 \alpha_2 \leq 1 \\ \alpha_{12}^{(2)} &= a_2 \alpha_{12} + b_2 \alpha_1 \alpha_2 \leq 1, \\ &\text{with } a_2 + b_2 = 1, \end{aligned}$$

where a_2 and b_2 are unknown coefficients denoting the weights of the theoretical depolarizing parameters α_1 , α_2 , and α_{12} associated with the theoretical channels Λ_1 , Λ_2 , and Λ_{12} . The depolarizing parameters $\alpha_1^{(2)}$, $\alpha_2^{(2)}$, $\alpha_{12}^{(2)}$ all lie in the interval $[0, 1]$, where a value of 0 (1) indicates an error channel that will produce a completely mixed state with probability 0% (100%). From the normalization condition, we obtain $b_2 = 1 - a_2$, and we can rewrite

$$\begin{aligned} \alpha_1^{(2)} &= \alpha_1 + a_2(\alpha_{12} - \alpha_1) \leq 1 \\ \alpha_2^{(2)} &= \alpha_2 + a_2(\alpha_{12} - \alpha_2) \leq 1 \\ \alpha_{12}^{(2)} &= \alpha_1 \alpha_2 + a_2(\alpha_{12} - \alpha_1 \alpha_2) \leq 1. \end{aligned}$$

We want to show that $\alpha_1^{(2)} \alpha_2^{(2)} \leq \alpha_{12}^{(2)}$. To this end we calculate

$$\alpha_1^{(2)} \alpha_2^{(2)} = \alpha_1 \alpha_2 + a_2 \alpha_1 (\alpha_{12} - \alpha_2) + a_2 \alpha_2 (\alpha_{12} - \alpha_1) + a_2^2 (\alpha_{12} - \alpha_1)(\alpha_{12} - \alpha_2).$$

Since $a_2 + b_2 = 1$, then $a_2 \leq 1$ and $a_2^2 \leq a_2$. Hence, we can write

$$\begin{aligned} \alpha_1^{(2)} \alpha_2^{(2)} &\leq \alpha_1 \alpha_2 + a_2 \alpha_1 (\alpha_{12} - \alpha_2) + a_2 \alpha_2 (\alpha_{12} - \alpha_1) + a_2 (\alpha_{12} - \alpha_1)(\alpha_{12} - \alpha_2) \\ &= \alpha_1 \alpha_2 + a_2 (\alpha_{12}^2 - \alpha_1 \alpha_2). \end{aligned}$$

Since the parameter α_{12} is a depolarizing parameter, it is true that $\alpha_{12} \leq 1$, and thus $\alpha_{12}^2 \leq \alpha_{12}$. We then have that

$$\alpha_1^{(2)} \alpha_2^{(2)} \leq \alpha_1 \alpha_2 + a_2(\alpha_{12} - \alpha_1 \alpha_2), \quad (\text{B.2})$$

or, using $\alpha_{12}^{(2)} = \alpha_1 \alpha_2 + a_2(\alpha_{12} - \alpha_1 \alpha_2)$,

$$\boxed{\alpha_1^{(2)} \alpha_2^{(2)} \leq \alpha_{12}^{(2)}}.$$

If Eq. (B.1) is true, then simple inductive arguments can be used to generalize this result to an SRB experiment on n qubits:

$$\begin{aligned} \alpha_{ij...s}^{(n)} &\geq \alpha_i^{(n)} \alpha_{jk...s}^{(n)} \geq \alpha_i^{(n)} \alpha_j^{(n)} \alpha_{kl...s}^{(n)} \geq \dots, \\ \alpha_{ij...s}^{(n)} &\geq \alpha_{ij}^{(n)} \alpha_{kl...s}^{(n)} \geq \alpha_{ij}^{(n)} \alpha_k^{(n)} \alpha_{l...s}^{(n)} \geq \dots, \\ &\dots \\ \alpha_{ij...s}^{(n)} &\geq \alpha_{ij...s-1}^{(n)} \alpha_s^{(n)}, \end{aligned}$$

for $s \leq n$.

Consequently, we expect to find the following hierarchy for the multi-qubit errors calculated from our 4-qubit SRB experiment:

$$\boxed{\bar{r}_4 \leq \tilde{r}_{4,3} \leq \tilde{r}_{4,2} \leq \tilde{r}_{4,1}.} \quad (\text{B.3})$$

These quantities are defined in Sec. 2.3.3 and Sec. 2.3.5.

References

- [1] K. Serniak et al. “Hot non-equilibrium quasiparticles in transmon qubits”. In: *arXiv:1803.00476* (2018). URL: <https://arxiv.org/abs/1803.00476> (cit. on p. 1).
- [2] David C. McKay et al. “Efficient Z gates for quantum computing”. In: *Phys. Rev. A* 96 (2 2017), p. 022330. DOI: 10.1103/PhysRevA.96.022330. URL: <https://link.aps.org/doi/10.1103/PhysRevA.96.022330> (cit. on pp. 1, 2, 8, 27, 34, 39).
- [3] D. C. McKay et al. “Three Qubit Randomized Benchmarking”. In: *arXiv:1712.06550* (2017). URL: <https://arxiv.org/abs/1712.06550> (cit. on pp. 1, 10).
- [4] Sarah Sheldon et al. “Procedure for systematically tuning up cross-talk in the cross-resonance gate”. In: *Phys. Rev. A* 93 (6 2016), p. 060302. DOI: 10.1103/PhysRevA.93.060302. URL: <http://link.aps.org/doi/10.1103/PhysRevA.93.060302> (cit. on pp. 1, 34).
- [5] J. Heinsoo et al. “Rapid High-Fidelity Multiplexed Readout of Superconducting Qubits”. In: *ArXiv e-prints* (2018). URL: <https://arxiv.org/abs/1801.07904> (cit. on pp. 1, 4, 9, 58).
- [6] J. Preskill. “Quantum Computing in the NISQ era and beyond”. In: *arXiv:1801.00862* (2018). URL: <https://arxiv.org/abs/1801.00862> (cit. on p. 1).
- [7] Austin G. Fowler et al. “Surface codes: Towards practical large-scale quantum computation”. In: *Phys. Rev. A* 86 (3 2012), p. 032324. DOI: 10.1103/PhysRevA.86.032324. URL: <http://link.aps.org/doi/10.1103/PhysRevA.86.032324> (cit. on pp. 1, 7, 10).
- [8] R. Barends et al. “Superconducting quantum circuits at the surface code threshold for fault tolerance”. In: *Nature* 508.7497 (Apr. 2014), pp. 500–503. ISSN: 0028-0836. DOI: 10.1038/nature13171. URL: <http://www.nature.com/nature/journal/v508/n7497/full/nature13171.html> (visited on 04/30/2014) (cit. on p. 1).
- [9] Jay M. Gambetta et al. “Characterization of Addressability by Simultaneous Randomized Benchmarking”. In: *Phys. Rev. Lett.* 109 (24 2012), p. 240504. DOI: 10.1103/PhysRevLett.109.240504. URL: <http://link.aps.org/doi/10.1103/PhysRevLett.109.240504> (cit. on pp. 1–3, 10, 13, 14, 16–19, 50).
- [10] Zhibo Hou et al. “Full reconstruction of a 14-qubit state within four hours”. In: *arXiv:1602.08604 [quant-ph]* (Feb. 2016). arXiv: 1602.08604. URL: <http://arxiv.org/abs/1602.08604> (visited on 03/02/2016) (cit. on p. 1).
- [11] Giacomo Torlai et al. “Neural-network quantum state tomography”. In: *Nature Physics* 14 (2018), p. 447. URL: <https://doi.org/10.1038/s41567-018-0048-5> (cit. on p. 1).
- [12] Philippe Faist and Renato Renner. “Practical and Reliable Error Bars in Quantum Tomography”. In: *Physical Review Letters* 117.1 (2016), p. 010404. ISSN: 1079-7114. DOI: 10.1103/physrevlett.117.010404. URL: <http://dx.doi.org/10.1103/PhysRevLett.117.010404> (cit. on p. 1).

- [13] Y. Salathé et al. “Digital Quantum Simulation of Spin Models with Circuit Quantum Electrodynamics”. In: *Phys. Rev. X* 5 (2 June 2015), p. 021027. DOI: 10.1103/PhysRevX.5.021027. URL: <http://link.aps.org/doi/10.1103/PhysRevX.5.021027> (cit. on pp. 1, 33, 36).
- [14] L. Steffen et al. “Deterministic quantum teleportation with feed-forward in a solid state system”. In: *Nature* 500 (2013), pp. 319–322. DOI: 10.1038/nature12422. URL: http://www.nature.com/nature/journal/v500/n7462/full/nature12422.html?WT_ec_id=NATURE-20130815 (cit. on p. 1).
- [15] Robin Blume-Kohout et al. “Demonstration of qubit operations below a rigorous fault tolerance threshold with gate set tomography”. In: *Nature Communications* 8 (Feb. 2017), p. 14485. URL: <http://dx.doi.org/10.1038/ncomms14485> (cit. on p. 1).
- [16] Easwar Magesan, J. M. Gambetta, and Joseph Emerson. “Scalable and Robust Randomized Benchmarking of Quantum Processes”. In: *Phys. Rev. Lett.* 106 (18 2011), p. 180504. DOI: 10.1103/PhysRevLett.106.180504. URL: <http://link.aps.org/doi/10.1103/PhysRevLett.106.180504> (cit. on pp. 1, 12, 14).
- [17] Easwar Magesan et al. “Efficient Measurement of Quantum Gate Error by Interleaved Randomized Benchmarking”. In: *Phys. Rev. Lett.* 109 (8 2012), p. 080505. DOI: 10.1103/PhysRevLett.109.080505. URL: <http://link.aps.org/doi/10.1103/PhysRevLett.109.080505> (cit. on pp. 1, 15, 16).
- [18] Easwar Magesan, Jay M. Gambetta, and Joseph Emerson. “Characterizing quantum gates via randomized benchmarking”. In: *Phys. Rev. A* 85 (4 2012), p. 042311. DOI: 10.1103/PhysRevA.85.042311. URL: <http://link.aps.org/doi/10.1103/PhysRevA.85.042311> (cit. on p. 1).
- [19] Jeffrey M. Epstein et al. “Investigating the limits of randomized benchmarking protocols”. In: *Phys. Rev. A* 89.6 (June 2014), p. 062321. DOI: 10.1103/PhysRevA.89.062321. URL: <https://journals.aps.org/prabSTRACT/10.1103/PhysRevA.89.062321> (cit. on pp. 1, 10, 27, 39).
- [20] Serwan Asaad et al. “Independent, extensible control of same-frequency superconducting qubits by selective broadcasting”. In: *Npj Quantum Information* 2 (Aug. 2016), pp. 16029–. URL: <http://dx.doi.org/10.1038/npjqi.2016.29> (cit. on pp. 1, 43).
- [21] A.D. Corcoles et al. “Demonstration of a quantum error detection code using a square lattice of four superconducting qubits”. In: *Nat Commun* 6 (Apr. 2015), pp. –. URL: <http://dx.doi.org/10.1038/ncomms7979> (cit. on pp. 2, 48).
- [22] J. Koch et al. “Charge-insensitive qubit design derived from the Cooper pair box”. In: *Phys. Rev. A* 76.4, 042319 (2007), p. 042319. DOI: 10.1103/PhysRevA.76.042319. URL: <http://link.aps.org/abstract/PRA/v76/e042319> (cit. on pp. 3–5).
- [23] Matthias Baur. “Realizing quantum gates and algorithms with three superconducting qubits”. PhD thesis. ETH Zurich, Mar. 2012. URL: http://qudev.phys.ethz.ch/content/science/Documents/phd/PhD_Thesis_Baur_Matthias.pdf (cit. on pp. 3–6, 29, 40).

- [24] Marek Pechal. “Microwave photonics in superconducting circuits”. PhD thesis. ETH Zurich, 2016. URL: http://qudev.phys.ethz.ch/content/science/Documents/phd/MarekPechal_PhDThesis_v4_160928.pdf (cit. on p. 3).
- [25] A. Wallraff et al. “Strong coupling of a single photon to a superconducting qubit using circuit quantum electrodynamics”. In: *Nature* 431 (2004), pp. 162–167. DOI: 10.1038/nature02851. URL: <http://www.nature.com/nature/journal/v431/n7005/full/nature02851.html> (cit. on p. 5).
- [26] Alexandre Blais et al. “Cavity quantum electrodynamics for superconducting electrical circuits: An architecture for quantum computation”. In: *Phys. Rev. A* 69 (6 2004), p. 062320. DOI: 10.1103/PhysRevA.69.062320. URL: <https://link.aps.org/doi/10.1103/PhysRevA.69.062320> (cit. on pp. 5, 6, 31).
- [27] Lars Steffen. “Quantum Teleportation and Efficient Process Verification with Superconducting Circuits”. PhD thesis. ETH Zurich, 2013. URL: http://qudev.phys.ethz.ch/content/science/Documents/phd/PhD-Lars_Steffen.pdf (cit. on p. 6).
- [28] C. J. Foot. *Atomic Physics*. Oxford University Press, 2007 (cit. on p. 6).
- [29] Ants Remm. “Implementation and characterization of multiplexed readout of superconducting qubits”. MA thesis. ETH Zurich, Nov. 2017. URL: http://qudev.phys.ethz.ch/content/science/Documents/master/Ants_Remm_MastersThesis.pdf (cit. on pp. 7, 9, 29–31, 34, 36).
- [30] M. M. Wilde. *Quantum Information Theory*. Cambridge University Press, 2013 (cit. on p. 7).
- [31] M. A. Nielsen and I. L. Chuang. *Quantum Computation and Quantum Information*. 10th. New York, NY, USA: Cambridge University Press, 2011. ISBN: 1107002176, 9781107002173 (cit. on pp. 7, 16, 54).
- [32] Stefania Balasius. “Single-Qubit Gates Calibration in PycQED using Superconducting Qubits”. MA thesis. ETH Zurich, 2017. URL: http://qudev.phys.ethz.ch/content/science/Documents/semester/Stefania_Balasius-Single-Qubit-Gates_Calibration_in_PycQED_using_Superconducting_Qubits.pdf (cit. on pp. 8, 34–36, 40).
- [33] Johannes Heinsoo. “Towards high fidelity two-qubit gates with superconducting qubits”. MA thesis. ETH Zurich, June 2014. URL: http://qudev.phys.ethz.ch/content/science/Documents/master/Johannes_Heinsoo_MasterThesis.pdf (cit. on pp. 8, 36).
- [34] Jonas Butscher. “Shaping of Fast Flux Pulses for Two-Qubit Gates: Inverse Filtering”. MA thesis. ETH Zurich, Jan. 2018. URL: http://qudev.phys.ethz.ch/content/science/Documents/master/Jonas_Butscher_MasterThesis.pdf (cit. on pp. 8, 36).
- [35] F. F. Fanchini et al. “Protecting the \sqrt{SWAP} operation from general and residual errors by continuous dynamical decoupling”. In: *Phys. Rev. A* 91 (4 2015), p. 042325. DOI: 10.1103/PhysRevA.91.042325. URL: <http://link.aps.org/doi/10.1103/PhysRevA.91.042325> (cit. on pp. 9, 34).
- [36] J. P. Gaebler et al. “Randomized Benchmarking of Multiqubit Gates”. In: *Phys. Rev. Lett.* 108 (26 2012), p. 260503. DOI: 10.1103/PhysRevLett.108.260503. URL: <http://link.aps.org/doi/10.1103/PhysRevLett.108.260503> (cit. on p. 10).

- [37] A. D. Córcoles et al. “Process verification of two-qubit quantum gates by randomized benchmarking”. In: *arXiv:1210.7011* (2012). URL: <http://arxiv.org/abs/1210.7011> (cit. on pp. 10, 14, 18, 21).
- [38] Peter Selinger. “Generators and relations for n-qubit Clifford operators”. In: *Logical Methods in Computer Science* 11 (2015) (cit. on p. 11).
- [39] J. Helsen et al. “Multi-qubit Randomized Benchmarking Using Few Samples”. In: *arXiv:1701.04299* (2017). URL: <https://arxiv.org/abs/1701.04299> (cit. on pp. 13, 16, 42, 43, 50).
- [40] Christoph Dankert et al. “Exact and approximate unitary 2-designs and their application to fidelity estimation”. In: *Phys. Rev. A* 80 (1 2009), p. 012304. DOI: 10.1103/PhysRevA.80.012304. URL: <https://link.aps.org/doi/10.1103/PhysRevA.80.012304> (cit. on p. 13).
- [41] Michael Tinkham. *Group theory and quantum mechanics*. Dover Publications, 2003 (cit. on p. 13).
- [42] Richard G. Lyons. *Understanding Digital Signal Processing*. 3rd. Upper Saddle River, NJ, USA: Prentice-Hall, 2011. ISBN: 978-0-13-702741-5 (cit. on pp. 29, 30, 40).
- [43] Rodney Loudon. *The Quantum Theory of Light*. Oxford U, 2000 (cit. on pp. 30, 62).
- [44] David C. McKay et al. “Universal Gate for Fixed-Frequency Qubits via a Tunable Bus”. In: *Phys. Rev. Applied* 6 (6 2016), p. 064007. DOI: 10.1103/PhysRevApplied.6.064007. URL: <http://link.aps.org/doi/10.1103/PhysRevApplied.6.064007> (cit. on p. 34).
- [45] M.A. Rol et al. *DiCarloLab-Delft/PycQED_py3: Initial public release*. Oct. 2016. DOI: 10.5281/zenodo.160327. URL: <https://doi.org/10.5281/zenodo.160327> (cit. on p. 34).
- [46] Joel J Wallman and Steven T Flammia. “Randomized benchmarking with confidence”. In: *New Journal of Physics* 16.10 (2014), p. 103032. URL: <http://stacks.iop.org/1367-2630/16/i=10/a=103032> (cit. on p. 42).
- [47] J. Helsen, *private communications* (cit. on p. 56).



Eidgenössische Technische Hochschule Zürich
Swiss Federal Institute of Technology Zurich

Declaration of originality

The signed declaration of originality is a component of every semester paper, Bachelor's thesis, Master's thesis and any other degree paper undertaken during the course of studies, including the respective electronic versions.

Lecturers may also require a declaration of originality for other written papers compiled for their courses.

I hereby confirm that I am the sole author of the written work here enclosed and that I have compiled it in my own words. Parts excepted are corrections of form and content by the supervisor.

Title of work (in block letters):

Characterization of Multi-Qubit Algorithms with Randomized Benchmarking

Authored by (in block letters):

For papers written by groups the names of all authors are required.

Name(s):

Balasius

First name(s):

Stefania

With my signature I confirm that

- I have committed none of the forms of plagiarism described in the '[Citation etiquette](#)' information sheet.
- I have documented all methods, data and processes truthfully.
- I have not manipulated any data.
- I have mentioned all persons who were significant facilitators of the work.

I am aware that the work may be screened electronically for plagiarism.

Place, date

Zurich, 31.05.2018

Signature(s)

For papers written by groups the names of all authors are required. Their signatures collectively guarantee the entire content of the written paper.